Ultrafast spectro-microscopy of highly excited low dimensional materials

Alessandra Virga

A Thesis presented for the degree of
Doctor of Philosophy

SAPIENZA
UNIVERSITÀ DI ROMA

Femtoscopy Group (Prof. T. Scopigno)
Department of Physics
University Sapienza
Italy

December 2018

Ultrafast spectro-microscopy of highly excited low dimensional materials

Alessandra Virga

Submitted for the degree of Doctor of Philosophy
December 2018

Abstract

Born-Oppenheimer approximation (ABO) is the assumption that the motion of atomic nuclei and electrons in molecules can be separated and independently treated. In solids, ABO is well justified when the energy gap between ground and excited electronic states is larger than the energy scale of the nuclear motion. Graphene represents a notable exception of this acceptantance. In particular, here we unravel the key role of the gapless linear Dirac dispersion in the vibrational Raman response of the system in the case of impulsively photoexcited graphene.

First, we unambiguously describe Four-Wave Mixing (FWM) processes in graphene, which depend on the resonant nature of the electronic interactions. Indeed, the overall spectral response is described in terms of a third order diagrammatic description of the light-matter interaction. We disclose that the interference between Coherent anti-Stokes Raman Scattering (CARS) and Non-Vibrationally Resonant Background (NVRB) generates Lorentzian dip spectral profiles. Actually, by introducing an experimental time delayed FWM scheme, able to modify the relative strength of the two contributions, we observe the first evidence of CARS peak equivalent to the Raman spectrum in graphene.

Second, we adopt sub picosecond photoexcitation which impulsively localize energy into graphene electronic subsystem. While the response of hot charge carriers is well-characterized, unraveling the behavior of optical phonons under strongly out-of-equilibrium conditions remains a challenge. Using a 3-ps laser excitation, which trades off between impulsive stimulation and spectral resolution, we show how the Raman response of graphene can be detected in presence of an electronic subsystem temperature largely exceeding that of the phonon bath. We find a peculiar behaviour

of the period and lifetime of both the G and 2D phonons as function of the carriers temperature in the range 1700-3100 K, suggesting a broadening of the Dirac cones. Accordingly, we reconsider the traditional scenario of the electron-phonon scattering in a highly excited transient regime.

List of publications/conference contributions

This thesis is based on following publications in journals and conference contributions:

C. Ferrante, G. Batignani, G. Fumero, E. Pontecorvo, **A. Virga**, L. C. Montemiglio, G. Cerullo, M. H. Vos, T. Scopigno. *Resonant Broadband Stimulated Raman scattering in Myoglobin*, **Journal of Raman Spectroscopy**, 2018; 18, 10.1002/jrs.5323

C. Ferrante, **A. Virga**, L. Benfatto, M. Martinati, D. De Fazio, U. Sassi, C. Fasolato, A.K. Ott, P. Postorino, D.Yoon, G. Cerullo, F. Mauri, A. C. Ferrari, T. Scopigno. *Raman spectroscopy of graphene under ultrafast laser excitation*, **Nature Communications**, (2018) 9:308, 10.1038/s41467-017-02508-x

A. Virga, C. Ferrante, L. Benfatto, M. Martinati, D. De Fazio, U. Sassi, C. Fasolato, A.K. Ott, P. Postorino, D.Yoon, G. Cerullo, F. Mauri, A. C. Ferrari, T. Scopigno. *The Raman spectrum of Graphene in presence of highly excited charge carriers*, Oral Contribution, **Graphene2017.**

A. Virga, C. Ferrante, L. Benfatto, M. Martinati, D. De Fazio, U. Sassi, C. Fasolato, A.K. Ott, P. Postorino, D.Yoon, G. Cerullo, F. Mauri, A. C. Ferrari, T. Scopigno. *Phonon anomalies in Graphene induced by highly excited charge carriers*, Oral Contribution, **CLEO/Europe-EQEC 2017 Conference on Lasers and Electro-Optics Europe & European Quantum Electronics Conference.**

A. Virga, C. Ferrante, L. Benfatto, M. Martinati, D. De Fazio, U. Sassi, C. Fasolato, A.K. Ott, P. Postorino, D.Yoon, G. Cerullo, F. Mauri, A. C. Ferrari, T. Scopigno. *The role of electron-phonon scattering in the Raman spectrum of Graphene in presence of highly excited charge carriers*, Oral Contribution, **Fis-**

Mat2017 - The Italian National Conference on Condensed Matter Physics.

A. Virga, C. Ferrante, L. Benfatto, M. Martinati, D. De Fazio, U. Sassi, C. Fasolato, A.K. Ott, P. Postorino, D.Yoon, G. Cerullo, F. Mauri, A. C. Ferrari, T. Scopigno. *Raman spectroscopy of graphene under ultrafast laser excitation*, Oral Contribution, **UP2018 XXI International Conference on Ultrafast Phenomena.**

A. Virga, C. Ferrante, L. Benfatto, M. Martinati, D. De Fazio, U. Sassi, C. Fasolato, A.K. Ott, P. Postorino, D.Yoon, G. Cerullo, F. Mauri, A. C. Ferrari, T. Scopigno. *Out of equilibrium electron-phonon interaction in graphene unraveled by Raman scattering by picosecond excitation*, Poster Presentation, **ICORS2018 The 26th International Conference on Raman Spectroscopy.**

Contents

Chapter 1

Motivation

Over the last decade the field of material sciences has witnessed significant increase in the fabrication of systems with reduced dimensionality. It is now understood that these materials on sufficiently short length scales exhibit properties that are considerably different from the bulk materials. Graphene is an example of this tendency: it is a one-atom thick planar sheet of sp^2 bonded carbon atoms, that are packed in a honeycomb crystal lattice. Even if it was isolated only in 2004 [1], since then it has been the focus of research activities in view of its great potential to underpin new disruptive technologies, substituting materials used in existing applications but also leading to radically new devices [2]. This growing interest has culminated in the recognition of graphene as one of the two pillars, that lead and inspire the projects launched in EU Horizon 2020 programme. Several recent results highlight the versatility in the application of this system, ranging from solar cells and light-emitting devices to touch screens, photodetectors and ultrafast lasers [3]. Nowadays, even global industrial partners, as Samsung, are working together with researchers and universities to create a new technology that promises double the electric capacity of Lithium batteries, thanks to the introduction of graphene as an efficient energy storage solution [4, 5]. Clearly all these applications are related to unique properties, such as high mobility, optical transparency and high termal conductivity [6–8], in addition to flexibility, robustness, and environmental stability [2, 5]. The very origin of such properties is strictly related to the gapless linear energy dispersion of graphene and the breakdown of the Born-Oppenheimer [9] approximation which

determines a strong coupling between electronic and vibrational degrees of freedom in the system.

Such peculiar properties obviously influence the light-matter interaction in graphene, making it a promising material for many optoelectronics devices due to a fast response time and a notable broadband wavelength-independent absorptive tendency [3, 7]. In particular, these features depend on the ultrafast dynamics of the system, which has aroused great interest in the last decade to be studied by means of time-resolved techniques [10, 11]. These studies have disclosed the key role of the carriers relaxation channels and, among them, the importance of phononic channel, which can be precisely observed by means of Spontaneous Raman (SR) Spectroscopy [12]. This frequency-domain technique provides information about the energy and dephasing time of phonons at thermodynamic equilibrium. This latter quantity is related to the inverse of Raman linewidth, although disentangling the specific processes that generate homogeneous and heterogeneous broadening in the frequency domain is a challenge.

For this purpose, in 2013, within the context of my master thesis, I embraced a project aimed at examining the graphene lifetime in time domain by detecting coherent Raman processes [13], wherein a short (tens of fs) pulse induces atoms to oscillate in phase, i.e. coherently, and a second time-delayed (ps) pulse probes the Raman spectrum. According to these measurements, the G-phonon dephasing time was about 5 times less than expected from the frequency-domain techniques [12]. Although a few possible explanation could be found, the full understanding of the data were not achived at the end of the work.

Is this effect due to the coherent feature of the photoexcited phonons? Could it be related to thermic effects? Could it be due to the use of pulsed excitation in the experiment instead of the continuous-wave lasers involved in Spontaneous Raman spectroscopy?

These open questions contributed to motivate this Ph.D. thesis. In this project, I combined coherent Raman techniques and picosecond Spontaneous Raman aiming at a complete characterization of graphene out-of-equilibrium electronic and vibrational degrees of freedom. In particular, we first analyze much more in detail the nature

of coherent Raman process in graphene. Then, we perform a Spontaneous Raman experiment by means of a picosecond laser pulses in order to isolate the effect of ultrafast optical excitation.

This work aims for bridging the gap between the graphene scientific community and the non-linear Raman spectroscopy one. The thesis is structured in five Chapters which summarize the main theoretical and experimental work done during my Ph.D. studies.

In Chapter *One*, the motivations of this Ph.D. thesis are presented and contextualized.

Chapter *Two* is introductive and sets the theoretical grounds for rest of the Chapters. In particular this Chapter discusses the main physical aspects of graphene, including electronic, vibrational and optical properties. Moreover, we introduce the main mechanisms responsible for the light-matter interaction with this system. An introduction to Spontaneous Raman spectroscopy is given, focusing on the graphene Raman response as fundamental characterization tool.

Chapter *Three* is totally focused on the CARS response in graphene. In particular, this section discusses about the derivation of four coupled equations for four-wave mixing process derived from Maxwell's equations. Then, a semiclassical treatment based on Feynman diagrams is presented. The rest of the chapter is focused on the experimental results. The compact versatile fiber-format Coherent Raman microscopy setup developed in our laboratory and its time-delayed scheme are discussed. CARS response of graphene is presented and it is theoretically described in terms of a quantum modelization of the third order polarization.

In Chapter *Four*, electron-phonon scattering, along with anharmonicity, are discussed due to ther pivotal role in the description of the equilibrium phonon properties in graphene studied by means of Raman scattering. In particular, an extensive description of e-ph coupling is presented in terms of Green's function and self-enegy. Moreover, spontaneous Raman measurements in graphene by using a 3-ps laser pulses are performed; indeed we show how the Raman response of graphene can be detected in presence of an electronic subsystem temperature largely exceeding that of the phonon bath. The experimental data are modelled by reconsidering

the traditional scenario of the electron-phonon scattering in a highly excited transient regime, wherein graphene is in out-of-equilibrium condition photoinduced by ps-pulses involved in the experiment.

Chapter *Five* is equivalent to a brief summary of the main results of this thesis.

Finally, details on CARS interaction are provided in the appendix.

Part I: Introduction

Chapter 2

Graphene and its Raman spectrum

The key role of carbon atoms in all organic and live organisms is absolute; however for long time only two structures, diamond and graphite [14], were commonly used. A new era for carbon has begun since the advent of fullerene in 1985 [15] and carbon nanotubes in 1991 [16]. Only in 2004 [17] the cornerstone of their structure, graphene, a single layer of carbon atoms bounded in sp^2 configuration forming an hexagonal lattice, was finally isolated and stable by itself. This has awaked interest on researches for this new carbon form, paving the way for the success of low-dimensional materials in several fields, from optoelectronics [2] to spintronics [18]. In this chapter, the main properties of graphene are reviewed. In addition, it is given a brief introduction to Raman effect, at the base of the spectroscopic techniques performed in this work. In particular, it is focused on the Raman spectrum of graphene.

2.1 Structural properties: from graphite to graphene

Graphene is a one-atom thick planar sheet of sp^2 bonded carbon atoms [1, 8, 17]. These atoms are packed in a honeycomb crystal lattice; it is actually an hexagonal lattice with a basis of two ions in each unit cell. Stacking of these graphene sheets forms multilayer graphene and graphite. Although there exist many different stack-

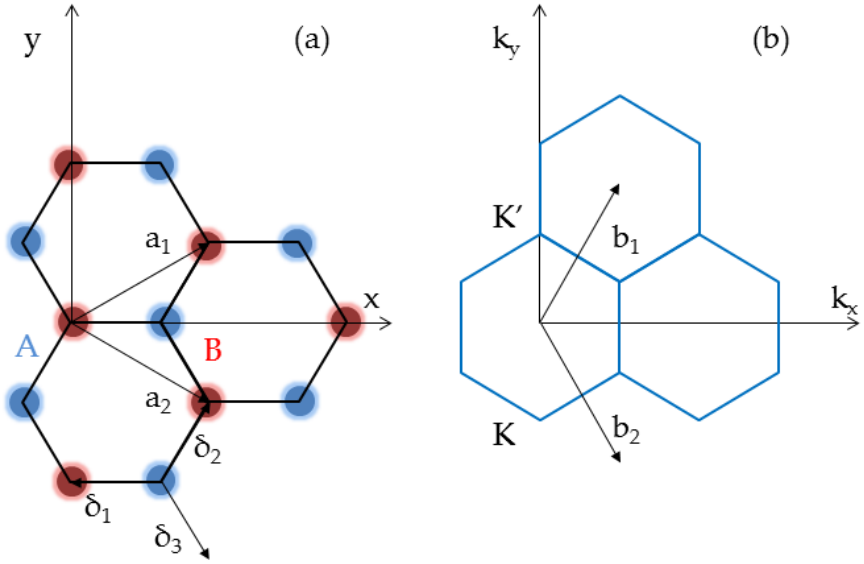

Figure 2.1: Unit-cell convention in single layer graphene. (a) Honeycomb lattice: The vectors $\boldsymbol{\delta}_1$, $\boldsymbol{\delta}_2$, and $\boldsymbol{\delta}_3$ connect the nearest carbon atoms, separated by a distance $a_{CC} \sim 1.42\,\mathring{A}$. The vectors $\mathbf{a}_1$ and $\mathbf{a}_2$ are basis vectors of the triangular Bravais lattice. A and B sublattice atoms are represented in blue and red, respectively. (b) Reciprocal lattice of the triangular lattice. The vectors $\boldsymbol{b}_1$ and $\boldsymbol{b}_2$ are basis vectors of the reciprocal lattice.

ing configurations, the lowest energy stacking forms when two adjacent layers are rotated by 60^o relative to each other and it is called Bernal stacking. The distance between graphene sheets in Bernal graphite is $3.35\,\mathring{A}$ in the z-direction.

Referring to the honeycomb crystal lattice shown in Fig.2.1.a, if $a_{CC} \sim 1.42\,\mathring{A}$ is the distance between the nearest neighbors, we identify the basic unit cell through the vectors:

$$\mathbf{a}_1 = \frac{a_{CC}}{2}(3, \sqrt{3}),\ \mathbf{a}_2 = \frac{a_{CC}}{2}(3, -\sqrt{3})$$

Accordingly, the nearest neighbors are identified by the vectors:

$$\boldsymbol{\delta}_1 = -\frac{1}{3}(\mathbf{a}_1 + \mathbf{a}_2),\ \boldsymbol{\delta}_2 = \boldsymbol{\delta}_1 + \mathbf{a}_1,\ \boldsymbol{\delta}_3 = \boldsymbol{\delta}_1 + \mathbf{a}_2$$

The reciprocal unit cell, shown in Fig.2.1.b, has basic vectors:

$$\mathbf{b}_1 = \frac{2\pi}{3a_{CC}}(1, \sqrt{3}),\ \mathbf{b}_2 = \frac{2\pi}{3a_{CC}}(1, -\sqrt{3})$$

Graphene honeycomb lattice was firstly isolated in 2004 [17] by micromechanical cleavage from graphite [1]. This procedure consists in peeling off a piece of graphite by means of an adhesive tape. Although the production technology has rapidly strenghten [19], this is still the method mainly chosen for fundamental research, as it guarantees the best samples in terms of purity, defects, mobility and optoelectronics properties. Nevertheless, it is impractical for large scale applications. Indeed, the widespread of graphene in technological application requires the production of large scale assembly with controlled growth. At this aim, several techniques have been developed [19]. Chemical vapour deposition [20] is able to produce few-layers graphene (FLG) on various substrates by feeding hydrocarbons at a suitable temperature [21–23], but it is not suitable for obtaining single layer graphene (SLG). Liquid phase exfoliation of graphite consists in chemical wet dispersion followed by ultrasonication, both in aqueous and non-aqueous solvents [24, 25]. This method offers advantages of scalability and no requirement of expensive growth substrates. Other remarkable techniques include the chemical synthesis [26] and carbon segregation from silicon carbide or metal substrates [27, 28].

2.2 Electronic properties in graphene

In graphene, each carbon atom has three in-plane σ bonds and one out-of-plane $2p_z$ orbital. The σ band, related to planar sp^2 orbitals, yields strong covalent bonds with the nearest carbon atoms; the π orbitals exhibit interlayer overlap in graphite that accounts for weak bonding along with van der Waals forces between the graphene layers. Thus, interaction between adjacent graphene layers or even interactions between a graphene layer and the substrate should affect the electronic structure [1, 8, 14].

Since there is no overlap between σ and π orbitals, in theoretical analysis as tight-binding method, each band can be treated independently from the others. The shortest gap between conduction and valance band is associated to σ band at Γ point: it counts more than 10 eV, revealing a covalent behavior of the sp^2 bonds. Nevertheless, the π band reveals that conduction and valence bands touch at K

points, showing a linear energy dispersion [8]. Since there is one valence electron per carbon atom in graphene, the valence band is completely filled, while the conduction band is completely empty: for this reason, graphene can be described as a zero-gap semiconductor.

As the number of layers increases, the energy dispersion becomes parabolic at the K point and the opening of a gap takes place due to interaction between different sheets and symmetry breaking. This justifies a semi-metallic behaviour [29].

Tight-binding method is able to calculate the spectrum of non-interacting electrons in this material. Here we restrict ourselves to the case of the nearest-neighbor tunneling terms and the most important features of the spectrum are well-described. We directly work in second quantization and define the annihilation (creation) operators of an electron at the lowest orbital centered around atoms of sublattice A and B (see Fig.2.1): a, b, $(a^\dagger, b^\dagger)$.

The full tight-binding Hamiltonian of graphene is given by [30, 31]:

$$H = -t \sum_{n,\delta,\sigma} (a^\dagger_{n,\sigma} b_{n+\delta,\sigma} + c.c.) \tag{2.2.1}$$

This expression indicates that the δ vectors connect the A atoms to their nearest neighbors and that the hopping, quantified by the parameter t, is possible only between the two different sublattices. In the equation, c.c stands for complex conjugate. In the following, the sublattice index will play the role of a pseudospin (σ is the real spin index) and the model can be expressed in terms of a spinor $\Psi^\dagger = (a^\dagger_k, b^\dagger_k)$, where the operators $a^\dagger_k$ and $b^\dagger_k$ indicate the excitations on the A and B sublattices in the k-space.

First of all, we want to diagonalize the Hamiltonian in order to determine its eigenvalues [31]. Since we have a translation invariant system, we now go to Fourier space and write:

$$a^\dagger_{n,\sigma} = \frac{1}{\sqrt{N}} \sum_k e^{-i\boldsymbol{k}\cdot\boldsymbol{r}_n} a^\dagger_{k,\sigma}$$

By substituting this expression in Eq.2.2.1, we can rewrite the Hamiltonian out as:

$$H = -t \sum_{\boldsymbol{k},\delta,\sigma} e^{-i\boldsymbol{k}\cdot\boldsymbol{\delta}} a^\dagger(\boldsymbol{k}) b(\boldsymbol{k}) + h.c. = \sum_{\delta,\sigma} \Psi^\dagger(\boldsymbol{k}) h(\boldsymbol{k}) \Psi(\boldsymbol{k}) \tag{2.2.2}$$

where the matrix h, called the Bloch Hamiltonian, takes the form:

$$h = \begin{pmatrix} 0 & f(\boldsymbol{k}) \\ f^*(\boldsymbol{k}) & 0 \end{pmatrix} \tag{2.2.3}$$

with $f(\boldsymbol{k}) = -t\sum_{\delta} e^{-i\boldsymbol{k}\cdot\boldsymbol{\delta}} = -t\left(e^{-ik_x a_{CC}} + 2e^{ik_x a_{CC}/2}\cos\left(\frac{k_y a_{CC}\sqrt{3}}{2}\right)\right)$. Since h is an Hermitian matrix, the diagolization is guaranteed and the corresponding eigenvalues are given by:

$$\epsilon_{\pm} = \pm|f(\boldsymbol{k})| = \pm t\sqrt{3 + 2\cos(\sqrt{3}k_y a_{CC}) + 4\cos(\sqrt{3}k_y a_{CC}/2)\cos(3k_x a_{CC}/2)}$$

Notice that even this simple tight-binding model predicts that the two bands touch at some points in the first Brillouin zone. By taking spin into account, we get that the lower band is exactly filled, since graphene has one accessible electron per atom,. This means that if we now discuss small excitations above the ground state, the excitations to be considered are those near the crossing points. To write the low energy theory, we have therefore to identify these points. We get them from the condition $f(\boldsymbol{k}) = 0$. This equation gives us the following points (plus any reciprocal lattice vector):

$$\left(0, \pm\frac{4\pi}{3\sqrt{3}a_{CC}}\right), \pm\frac{2\pi}{3a_{CC}}\left(1, \frac{1}{\sqrt{3}}\right), \pm\frac{2\pi}{3a_{CC}}\left(1, -\frac{1}{\sqrt{3}}\right)$$

Actually, all the points listed above sit in the corners of the first Brillouin zone. A simple inspection shows that the above set of k-space vectors is not independent and we choose one representative vector from each set. These are conventionally called K and K':

$$\boldsymbol{K} = \frac{2\pi}{3a_{CC}}\left(1, \frac{1}{\sqrt{3}}\right), \boldsymbol{K}' = \frac{2\pi}{3a_{CC}}\left(1, -\frac{1}{\sqrt{3}}\right) \tag{2.2.4}$$

The energy bands cross at these points, and the gap closes. In order to study the low-energy excitation regime, we expand around K and K':

$$f(\boldsymbol{K}' + \boldsymbol{q}) \approx -\frac{3ta_{CC}}{2}e^{-2\pi i/3}(q_y + iq_x)$$

Thus, upon changing the phases of A and B, which physically means changing the phases of the basis wavefunctions, the h matrix can be brought to the form:

$$h(\boldsymbol{K}' + \boldsymbol{q}) = -\frac{3ta_{CC}}{2}\begin{pmatrix} 0 & q_y + iq_x \\ q_y - iq_x & 0 \end{pmatrix} = -\hbar v_F \boldsymbol{q}\cdot\boldsymbol{\sigma} \tag{2.2.5}$$

where $\boldsymbol{\sigma}$ is the vector of Pauli-matrices. This is just the 2D massless Dirac Hamiltonian, which describes free relativistic electrons, where the light speed has been replaced by the Fermi velocity $v_F = \frac{3ta_{CC}}{2\hbar} \sim 10^6$ m/s. Keeping the same notation and using the same spinor, the Hamiltonian around K would give instead:

$$h(\boldsymbol{K} + \boldsymbol{q}) = \hbar v_F \boldsymbol{q} \cdot \boldsymbol{\sigma} \tag{2.2.6}$$

The eingenvalues of this matrix are:

$$E = \pm \hbar v_F q \tag{2.2.7}$$

Then, around K and K' the energy dispersion is linear (see Fig.2.2 and, more importantly, we can have both positive and negative excitations (i.e. electrons and holes), described by the same Hamiltonian (charge conjugation). Notably in supported graphene, many body effects can be neglected, i.e. electrons behave as if there were no electron-electron interactions [32–34]. As a result, v_F can be considered as a constant. If now we consider the expansion up to the second order in k we retrieve the so-called trigonal warping [8]. For higher energy states the cone deforms to adopt a triangular-like shape, i.e. the dispersion relation depends on the direction in momentum space. This effect is neglected in this work.

Eq.2.2.7 strongly recalls the photons dispersion relation, as it can be expressed in the relativistic form:

$$E(q) = \pm \sqrt{q^2 c_*^2 + m_*^2 c_*^4} = \pm c_* q$$

with an effective mass $m_* = 0$ and an effective light velocity c_* equal to the Fermi velocity v_F. For this reason, electrons and holes in graphene are called massless Dirac fermions [8]. Nevertheless, electrons in graphene are not strictly speaking relativistic as their velocity is approximately 300 times smaller than the light velocity, the electronic wavefunctions near the K and K points obey the Dirac equation (and not the Schrödinger one) for massless fermions and have a well defined chiralityTIR,Noselov.

We now calculate the electronic density of states g(E), which counts the number of quantum states in the vicinity of a fixed energy E [35]. It may be obtained from the total number of states N below the energy E.

$$N(E) = d \sum_{\epsilon < E} = A \int_0^E d\epsilon \, g(\epsilon) \tag{2.2.8}$$

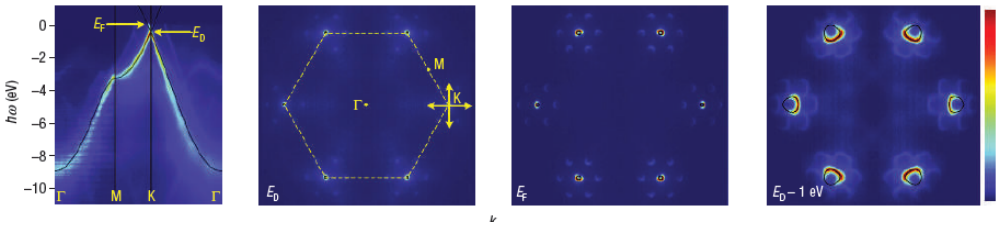

Figure 2.2: The band structure in graphene: ARPES measurement of the dispersion relation of epitaxial graphene (from Ref. [36])

So, $g(E)$can be expressed as:

$$g(E) = \frac{1}{A}\frac{\partial N}{\partial E} \tag{2.2.9}$$

where A is the total surface and $d = 4$ takes into account the degeneracy due to internal degrees of freedom (valley degeneracy and electron spin). In the vicinity of the Dirac points, N may be calculated quite easily because of the isotropy of the energy dispersion.

$$N(E) = \frac{Ad}{2\pi}\int_0^{q(E)} dq\, q \tag{2.2.10}$$

Then, it follows the expression for g(E):

$$g(E) = \frac{d}{2\pi} = \frac{q(E)}{\partial E/\partial q} = \frac{2}{\pi}\frac{E}{\hbar^2 v_F^2}$$

wherein the spin and the valley degeneracy are taken into account. Note that due to the electron-hole symmetry, $g(E)$ is valid for both electrons and holes. It scales linearly with the energy E and vanishes at the Dirac points. This situation is different from what is usually happening in a solid, where the density of states is constant (due to the parabolic dispersion relation).

2.3 Lattice vibrations in graphene

Graphene has two atoms for unit cell. Then there are six possible phonon dispersion branches in Γ point at Brillouin zone (see Fig. 2.3): three optical (O), whose frequencies do not vanish in the long-wavelength limit, and three acoustic (A). The vibrations perpendicular to the plane formed by graphene lattice (out-of-plane modes) are softer than in-plane motions; the latter can be distinguished

between longitudinal and transverse, with respect to the vector formed between the two carbon atoms that compose the unit cell. So the six branches can be divided into three cases: two in-plane longitudinal (iLA and iLO), two in-plane transverse (iTA and iTO) and two out-of-plane transverse (oTA and oTO) [37].

These six branches can be measured experimentally by inelastic neutron [38] or X-ray [39–41] scattering, as well as electron energy loss spectroscopy (EELS) [42, 43]. Raman scattering can also be performed to study the phonon modes in graphene as it will appear clear in the following sections. From a theoretical point of view, the phonon dispersion has been determined using empirical force-constant calculations [38, 41] and density functional theory (DFT) [39, 44–46]. In order to reproduce the experimental results, graphene case requires to consider contributions from long-distance forces, such as from the n-th neighbor atoms, ($n = 1, 2, 3, 4...$). These effects are taken into account by the so-called GW method [47, 48]. Other correction in the calculations are given by renormalization effects [49] or the electron-phonon coupling (EPC), a process in which a phonon can create an electron-hole pair. This intense EPC cannot be understood within the framework of the Born-Oppenheimer approximation [9] and gives rise to an interesting effect, known as Kohn anomaly [48].

Indeed, in the phonon dispersion curve, shown in Fig. 2.3, the most remarkable feature is the discontinuity in the frequency derivative of the highest optical branches at Γ and at K, corresponding to E_{2g} and A_1' points respectively. This feature can be explained by Kohn anomalies. In fact, in semimetallic systems the atomic vibrations are partially screened by electrons: this can occur only for phonons, whose wavevector could connect two electronic states at the Fermi surface. As in graphene, the band gap is zero only at two equivalent points K and K'=2K, Kohn anomalies will appear only in Γ and K points at Brillouin zone. They cause a strong interaction between electron and phonons, that makes E_{2g} and A_1' symmetry points responsible for the main features of Raman spectrum of graphene [50].

Among the six normal modes (two doubly degenerate), the in-plane optical E_{2g} phonon is the only Raman active mode: it is due to the in-plane streching of carbon-carbon bonding and it gives rise to the G band, which is signature of all sp^2 carbon

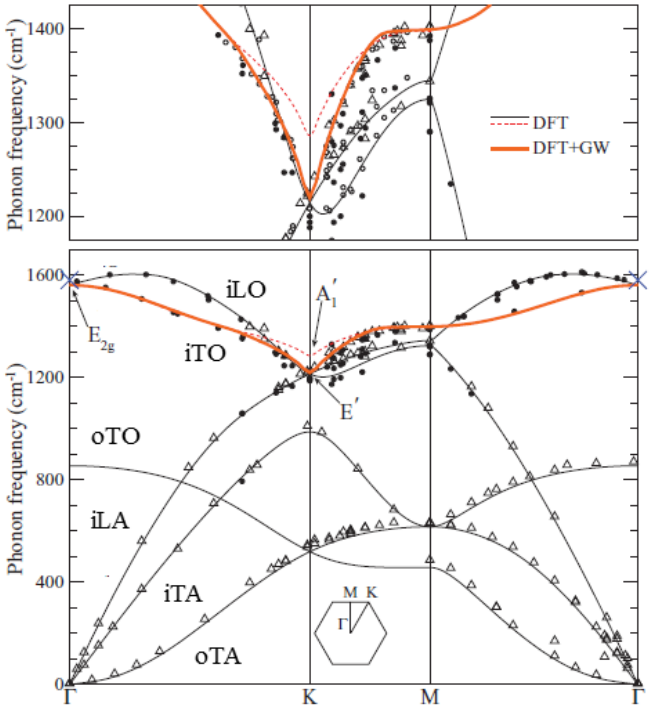

Figure 2.3: Experimental and simulated phonon dispersion of graphene. The solid lines represent DFT calculations with GW corrections from Refs. [40,47]. The symbols represent inelastic X-ray scattering measurements from Refs. [39] (full circles) and [41] (open triangles). The six phonon branches are labeled. (Adapted from Ref. [48]).

allotropes [51]. The A_1' vibration mode corresponds to the breathing modes of six-atom rings and requires a defect for its activation: thus it is prohibited in pristine graphene. As the number of graphene sheets increases progressively towards graphite, the two atoms of the unit cell in each layer are no more equivalent. In fact graphite has four atoms per unit cell and all the optical modes become Davydov-doublets. It follows that there are two Raman active E_{2g} modes in graphite, each doubly degenerate [12].

2.4 Optical properties

Graphene has unprecedented thermoelectrical characteristics: high electrical conductivity ($\sim 1.0 \cdot 10^8$S/m), high melting point (4510 K), high thermal conductivity

($2000-4000$ W m^{-1}K^{-1}, 5000 W/m K), highest current density ($\sim 1.6\cdot 10^9$A/cm^2), including a high electron mobility (200000 cm^{2}V^{-1} s^{-1} at electron density $\sim 2\cdot 10^{11}$cm^{-2}) [5, 8, 52, 53]. In particular, in this section, we discuss more in detail the peculiar optical properties of graphene.

Absorption: The optical absorption of graphene arises from two distinct contributions: intraband and interband optical transitions [54, 55]. The weight of each term depends on the spectral range of interest. In the far-infrared region,the optical response is dominated by the free-carrier (or intraband) response (Fig.2.4.a), which is described in good approximation by the Drude Model [6]. In the mid-to near-infrared and visible region, the absorbance is attributed primarly to interband transitions (Fig.2.4.b); the response is almost frequency indipendent and its value equals the fine structure constant $\alpha = e^2/4\pi\epsilon_o\hbar c$ [7]. The optical response can be tuned and controlled through electrostatic gating (Fig.2.4.c), which induces Pauli blocking (i.e. a consequence of the exclusion principle according to which electron transitions are inhibited if the arrival state is occupied by another electron) of the optical transitions due to a change in the Fermi energy [56, 57]. Finally, in the UV range the transitions approach the saddle-point singularity and the interband optical absorption increases exhibiting excitonic effects [58, 59].

The absorption response due to interband transition can be calculated from the Fermi golden rule [54] by adopting a time-dependent first order perturbation theory. Let us introduce the optical conductivity $\sigma(\omega)$ of graphene, which links the electric current density $\boldsymbol{j}$ and the electric field vector $\boldsymbol{E}$:

$$j(\omega) = \sigma(\omega)E(\omega)$$

By applying the Dirac cone approximation where we assume that the conductivity is only contributed by the carriers on the Dirac cone (valid only if the Fermi energy and the photon energy are within the visible range), we obtain.

$$\sigma(\omega) = \frac{e^2}{4\hbar}\left(f\left(-\frac{\hbar\omega}{2}\right) - f\left(\frac{\hbar\omega}{2}\right)\right) = \frac{e^2}{4\hbar}\frac{sinh\left(\frac{\hbar\omega}{2k_BT}\right)}{cosh\left(\frac{\hbar\omega}{2k_BT}\right) + cosh\left(\frac{E_F}{2k_BT}\right)} \qquad (2.4.11)$$

where f is the Fermi-Dirac distribution, E_F the Fermi energy, k_B the Boltzmann constant and T the temperature. When the Fermi level is located at the Dirac point,

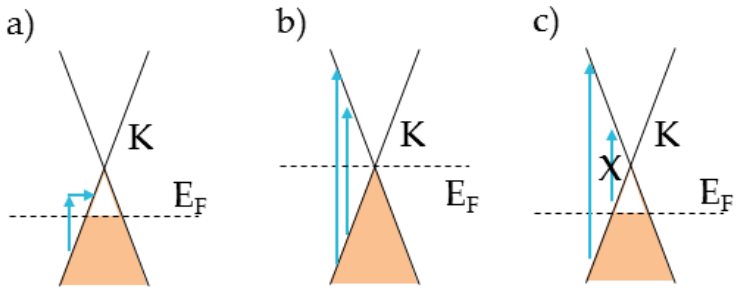

Figure 2.4: a) A schematic representation of the intraband absorption process. To conserve momentum, scattering with phonons or defects (horizontal arrow) is needed. b) Schematic of interband optical transitions in graphene and change of the optical response due to Pauli blocking induced by electrostatic doping. Solid black lines represent SLG electronic dispersion, i.e. the Dirac cones at K and K' vertices. Band population is associated to occupied states (shaded areas). Interband transition are accompanied by photon absorption (blue arrows).

the whole conductance band is empty: there is always an electron-hole pair that can be excited by an incident photon with corresponding energy. The result is a broad absorption energy for photon energy across the whole spectrum. When $\hbar\omega \sim k_B T$ and $E_F \ll \hbar\omega, k_B T$, the interband optical conductivity is approximately a constant in the visible range: $\sigma(\omega) = e^2/4\hbar$. The transmittance T of graphene in the air at normal incidence is given by

$$T = (1 + \sigma/2c\epsilon_o)^{-2} \tag{2.4.12}$$

which can be obtained straightforwardly by solving the Maxwell equation with appropriate boundary conditions. By replacing σ in the previous equation, we have:

$$T = (1 + e^2/8\hbar\epsilon_o)^{-2} = (1 + \pi\alpha/2)^{-2} \sim 1 - \pi\alpha \tag{2.4.13}$$

where $\pi\alpha \sim 2.3\%$. It follows that SLG has a transmittance of about 97.7%. Moreover, the independence of T on both frequency and material properties can be understood by simple considerations. Indeed, in perturbation theory the optical absorption is the product of three terms: the photon energy ($\propto \omega$), the joint density

of states ($\propto \omega/v_F^2$) and the square of the transition matrix element ($\propto v_F^2/\omega^2$). It follows the perfect cancelation of ω and v_F dependence.

More complex calculations have been done beyond the Dirac cone approximation and they show that the corrections to this model are surprisingly small, only a few percent [60]. In addition it has been experimentally proved that the optical sheet conductance of graphite is proportional to the number of layers N, as multilayer graphene can be essentially considered a decoupled N layers graphene [7]. Obviously, the model can be integrated, introducing many-body interactions to the electromagnetic response of graphene and its behaviour at different doping condition [56].

Emission: The fast (100fs-1ps) and efficient non-radiative charge recombination channels prevents any light emission due to the absence of a gap [54, 61, 62]. As result, the only widely investigated type of light emission from graphene is the inelastic scattering associated with phonon creation or annihilation, i.e. Raman scattering [12]. However, hot-luminescence can be observed at peculiar condition of the electronic distribution, e.g. at large electronic temperature or at large E_F. These conditions can be photoinduced impulsively or obtained by applying a gate voltage, respectively [61–67].

Optoelectronics applications: Since its isolation in 2004 [17], graphene has been in focus of research activities due to recognition of its great potential to underpin new disruptive technologies, substituting materials used in existing applications but also leading to radically new devices [2]. Indeed, as already shown, it has attractive electronic and optical properties, making it ideal for photonics and optoelectronics [3]. For example, photodetectors measure photon flux or optical power by converting the absorbed photon energy into electrical current. As graphene absorbs from UV to THz [54], graphene based photodetectors could work over a much broader wavelength range. Moreover, the response time is ruled by the carrier mobility. As, graphene has huge mobilities, these detectors can work on ultrafast timescales [68]. In addition, the ultrafast carrier dynamics, combined with large absorption and Pauli blocking make graphene an ideal ultra-broadband, fast saturable absorber [69, 70]. Other possible applications are photovoltaic devices [5], light-emitting devices [71]

and touch screens [23].

Light damaging: In nonlinear optical applications, graphene interacts with intense, ultrashort laser pulses: clearly there exists an upper limit for the photon flux that this layer can withstand. So this has to be controlled in order to define the damage threshold, which is an important parameter in every nonlinear experiment involving this material. Laser-induced damage of samples arises from either thermal or non-thermal effects.

Continuous-wave lasers produce thermal damage by photon absorption and subsequent energy dissipation through phonons, which at sufficient incident optical energy can be violent enough to break bonds. Conversely, the energy from femtosecond laser pulses is transferred at rates significantly faster than the phonon relaxation time. In multilayer graphene, it could cause two different ablation mechanisms [72]. The one responsible for the low fluence ablation threshold is the removal of intact graphite sheets and it does not involve melting. In fact the laser pulse induces strong vibrations of the graphite planes, which lead to collisions of the planes. As a consequence, the planes at the top and at the bottom are removed from the surface of the film. In contrast, the high fluence threshold corresponds to bond breaking processes inside the graphite layers and leads to ultrafast melting and expansion of the film [73].

We define the damage threshold as the point at which the exposure to a laser beam creates an hole in the carbon lattice. Its evaluation is fundamental to understand the power of incoming fields that can be used in the experiments. Thus, the laser pulse parameters - its duration, optical fluence, exposure time and frequency - are important for examining the performance and limitation of graphene-based optic and photonic devices. As damaging relies on breaking bonds, it depends on graphene substrate and on growth procedure. In the case of micro-mechanical exfoliation of graphite, 150 fs Ti:Sapphire laser with 76 MHz repetition causes ablation in 10-15 layer graphene after $2\,s$ exposure time at $\sim 4.2\,mJ/cm^2$ [74]. Let us consider the case of CVD process: in the range from 50 fs to 1.6 ps, the energy fluence at which the graphene damaged is nearly the same ($\sim 200\,mJ/cm^2$). Nevertheless, below this threshold multiple exposures could lead to the early degradation of the

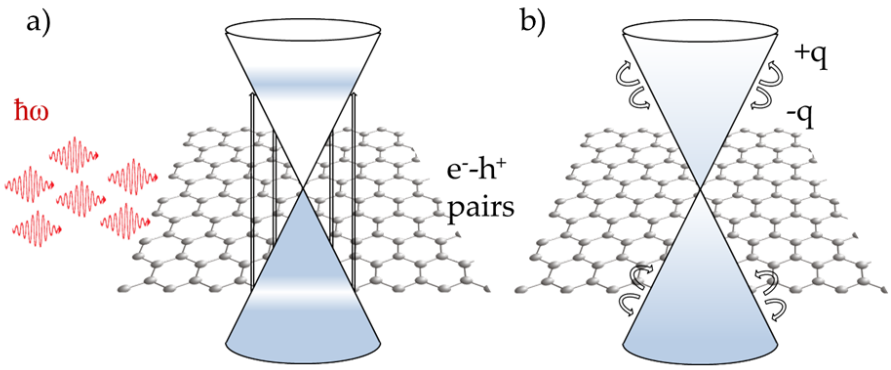

Figure 2.5: Sketch of the light-matter interaction in graphene. a) Photons (in red) impinge on graphene creating e-h pair. b) The fast e-e scattering determine an hot Fermi-Dirac distribution on fs timescale.

lattice [75].

2.5 Ultrafast dynamics in graphene

Over the last decade, non-equilibrium dynamics of charge carriers and phonons have aroused great interest, leading to many theoretical and experimental studies [10, 11]. Their main purpose is to describe the different relaxation processes of the electrons (holes) in the conduction (valence) band, which can be conveniently excited by ultrashort pulsed laser. The excitation of a system with above band-gap photons creates a non-thermal electronic population in the conduction band. The transient electronic temperature (T_{el}) of this carriers distribution will be much higher than the lattice temperature (T_l). Then the photoexcited carriers experience a wide variety of possible relaxation processes. These include electron-electron (e-e) scattering, electron-phonon (e-ph) scattering, recombination and generation mechanisms, charged impurity scattering and Auger processes, such as impact ionization and Auger recombination. Eventually photogenerated carriers recombine via radiative or non-radiative mechanisms thus bringing the system back to its equilibrium state. In graphene, the absence of a gap causes the generation of electron-hole (e-h) pair at any optical excitation (Fig.2.5.a). When photons impinge on graphene,

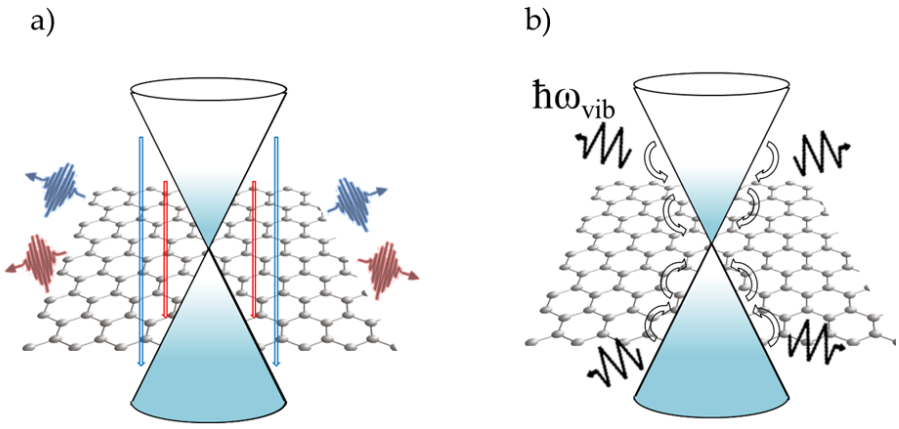

Figure 2.6: Sketch of the e-h pair recombination processes in graphene. a) Radiative channel: hot-luminescence; b) e-ph scattering on ps timescales (phonons with energy $\hbar\omega_{vib}$ are depicted as zigzag arrows).

they create a highly nonequilibrium hot electron distribution, which first relaxes on an ultrafast timescale to a thermalized, but still hot, Fermi-Dirac distribution (Fig.2.5.b) and then slowly cools down eventually reaching thermal equilibrium with the lattice [76–87].

The entire scenario of experimental and theoretical studies points to the existence of two different timescales. A fast initial relaxation on a timescale of some tens of femtoseconds is responsable for the establishment of a hot Fermi Dirac distribution in the conduction band due to Coulomb- induced e-e scattering. This fast and efficient relaxation channel is associated to linear gapless dispersion band which guarantees the energy-momentum conservation required by the e-e scattering.

Once the hot Fermi-Dirac distribution is reached, the slower (hundreds of femtoseconds) process is associated with carrier cooling and it can takes place through radiative mechanisms, known as hot-luminescence (Fig.2.6.a), and non-radiative mechanisms, such as e-ph scattering (Fig.2.5.b). Optical-phonons [78, 81] are the first (in time) relaxation channel of excited electronic states, due by the strong coupling of electrons with optical phonons near the K and Γ points in correspondence with Kohn anomalies. The e-ph scattering can be intra or interband and intra or intervalley. The intraband intravalley e-ph scattering involving an arbitrary small momentum transfer is the predominant mechanism. Indeed, interband scattering is

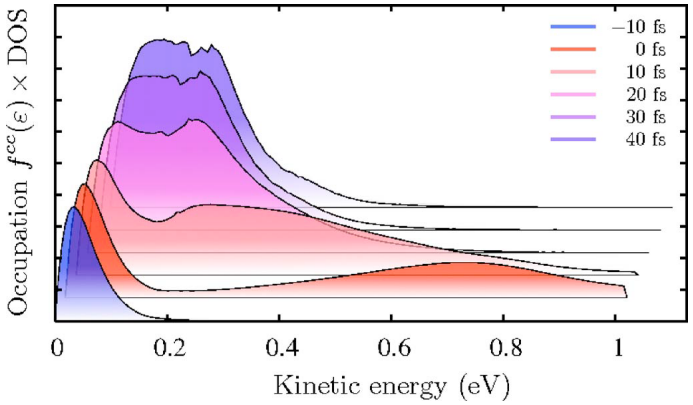

Figure 2.7: Temporal evolution of the angle-integrated population, i.e. the occupation of the conduction band times the density of states (DOS) after excitation with laser pulse at t=0. (Adapted from [76]).

less efficient as, in order to relax to the valence band, all electrons have to cross the vicinity of the K point, which has a low density of states and therefore acts as a bottleneck for the dynamics. Moreover, inter-valley scattering processes involve two different Dirac cones. Therefore a large momentum transfer to scatter electrons between two cones is needed, and the scaling of the Coulomb matrix with $1/q^2$ (where q is the exchanged momentum) suppresses these processes. Consequently the inter-valley scattering plays a minor role in the relaxation dynamic in graphene. Moreover, acoustic phonons are essentially decoupled with the electronic states but they are coupled with the optical phonons acting on a timescale longer than a picosecond.

These relaxation mechanisms are shown in Fig.2.7, wherein the population of the conduction band integrated over the angle is calculated, looking at the dynamics shortly after an optical excitation at 1.6 eV and 10 fs f temporale duration [76]. Before the pulse arrives, a slight Fermi tail reaches into the conduction band due to the finite temperature. The laser pulse creates a non-thermal population 800 meV above the band crossing. After 10 fs, the distribution has already partly relaxed and the distribution function 30 and 40 fs shows only minor differences. This is due to the finite population of the initially quasi-unoccupied phonon modes.

The ultrafast dynamics of the electronic distribution has been object of several works both experimental [66,78,86,88] and theoretical [76,77,79–85,87] for the pur-

pose of determining the temporal timescale and the parameters that affect it. In particular, monitoring graphene transient absorption [86] enables the direct measurement of the distribution function in real time. For example, the time-evolving hot-electron distribution inhibits, due to Pauli blocking, the absorption of the probe pulse at lower photon energies with respect to the pump, thus yielding an increase in transmission. Furthermore, the time evolution of these transient measurements gives access to the typical timescales characterizing the electrons dynamics [66, 78, 86].

Generally when a system is photoexcited, the relaxation towards equilibrium condition involves also radiative processes. In particular, among the single-photon interaction, fluorescence corresponds to the emission of redshifted light. Indeed, in semiconductors systems the e-h pairs, generated by the light-matter interaction, firstly relax on the bottom of the conduction band through intraband phonon-induced scattering. Then, the pair recombinate, emitteing light. The absence of a gap in graphene prevents any emission of light. Indeed, the fast e-e and e-ph scattering act on timescale much shorter than those of the typical recombination, without emitting photons [3].

Nevertheless, graphene could emit light if the fast non-radiative channels were slowed down [61, 63, 64, 89, 90]. For example, photoluminescence emission from graphene is observed after impulsive photoexcitation. Indeed, the high peak power promotes a large electronic density in the conduction band. This clogging effect prevents the action of e-e and e-ph decay channels, facilitating the radiative one. This emission is observed in both Stokes and Antistokes side and shows a non-linear dependence on fluence. The blueshifted emission at increased fluence and nonlinearity allows to preclude the conventional hot-luminescence, while the large non-quadratic variation of the emitted light as a function of fluence excludes the possibility to address it to two-photon absorption. The graphene nonlinear PL is particularly efficient and broadband due to several unique properties of graphene: i) carrier-carrier scattering requires both energy and momentum conservations, which are readily satisfied in the linear bands of graphene; ii) the line bands lead to a symmetric distribution of non-nequilibrium electrons and holes, which facilitates direct recombination of excited e-h pairs; iii) the energy acquired by an e-h pair via intra-

band scattering cannot be more than its kinetic energy, which equals $\hbar\omega - E_g$, and it is the maximum in gapless materials such as graphene; iv) The greatly reduced dielectric screening in the 2D graphene results in a very high Coulomb scattering rate that is essential for establishing the strong e-h recombination [91].

This non equilibrium photoluminescence recalls the grey body emission and can be in first approximation described by Planck's law [61, 62, 64, 67]:

$$I(\hbar\omega, T_e) = \mathcal{R}(\hbar\omega)\tau_{\mathrm{em}}\eta\frac{\hbar\omega^3}{2\pi^2c^2}\left(e^{\frac{\hbar\omega}{kT_e}} - 1\right)^{-1} \tag{2.5.14}$$

where η is the emissivity, defined as the dimensionless ratio of the thermal radiation of the material to the radiation from an ideal black surface at the same temperature as given by the Stefan-Boltzmann law [92], τ_{em} is the emission time and $\mathcal{R}(\hbar\omega)$ is the frequency-dependent, dimensionless responsivity of the detection chain. Refs. [61,62,67] reported that, although Eq.2.5.14 does not perfectly reproduce the entire grey body emission, the good agreement on a$\sim$ 0.5eV energy window is sufficient to extract T_{e}. Furthermore, hot-luminescence emission is a notable fingerprint of the out-of-equilibrium electronic distribution.

2.6 Raman Spectroscopy

Raman spectroscopy [93] is based on the inelastic scattering of an incoming electromagnetic field (ν_o), that produces a change in the polarization of sample's molecules. When a system interacts with an intense electromagnetic source, most of the light is scattered by the sample without changing its wavelength through an elastic process, called Rayleigh Scattering. Nevertheless, the coupling between the vibrational modes (ν_{vib}) of the sample and the driving frequency of the electric field is able to generate new spectral components (see Fig. 2.8). The system changes its vibrational state following the incoming photon and it can reach a virtual excited state. Subsequently, it will spontaneously relax back to ground state: this explains the strong Rayleigh component in the spectrum. If the system relaxes back to an excited vibrational state, the emission of Stokes (redshited) photons: $\nu_s = \nu_o - \nu_{vib}$ is observed. Moreover, it is necessary to consider the possibility that the Raman process can be activated from an excited vibrational level: relaxation to the ground

state will generate the emission of light at higher frequency, named the Anti-Stokes (blueshifted) component: $\nu_{as} = \nu_o + \nu_{vib}$. The inelastic scattering of light is known as the Raman effect, named in honor of Indian scientist Sir Chandrasekhara Venkata Raman (1988-1970), who discovered this effect in 1927 [93].

Remarkably, only a tiny fraction of the scattered light (typically one photon over ten millions) is scattered inelastically, which justifies the spread of this spectroscopic technique after the invention of the laser. Due to a small cross section ($\sim 10^{-30}\text{cm}^2$/molecule), spontaneous Raman has a very weak signal and requires high laser power and long integration times. In addition, the signal is often overwhelmed by a fluorescent background from the sample, limiting its application. In a real experiment we do not probe a single molecule, but an assembly of molecules with their random initial phases and orientations; thus each of them will act as an independent source of radiation, that will sum incoherently, spreading in a 4π steradian solid angle. Although we can collect only a small fraction of the produced signal, Raman spectroscopy overcomes the limitations of IR spectroscopy [94]. Unlike Raman scattering, infrared spectroscopy is based on changes of dipole moment and, for centrosymmetric molecules, IR and Raman spectroscopy are completely complementary. Although infrared spectroscopy is also a powerful tool in imaging, it is limited to low spatial resolution because of the long wavelength of light used. Furthermore, the absorption of water in the infrared region makes it difficult to use for samples rich in water. However this absorption does not limit the applicability of Raman spectroscopy, thanks to a wider range of tunability for electromagnetic sources used. After all, in Raman process a single intense narrowband laser is able to provide information about all possible vibrations of a sample, whereas for IR absorption a narrowband laser would give access to a limited narrowband absorption. Nowadays, Raman spectroscopy is widely used characterization tool for studying liquids, gases and solids [95, 96].

2.6.1 Classical picture of light scattering

In the classical framework, the incoming electromagnetic field $\mathbf{E}_o$ induces microscopic dipole moments $\boldsymbol{\mu}(t)$ by pertubing the electronic charge density in the atoms

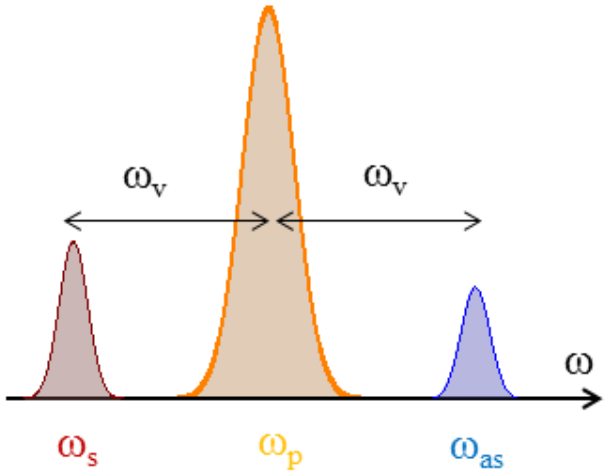

Figure 2.8: Output frequencies of spontaneous Raman process.

of the crystal:

$$\boldsymbol{\mu(t)} = -e\mathbf{r}(t) \tag{2.6.15}$$

where $\mathbf{r}(t)$ quantifies the motion respect to the equilibrium position and it depends on the interaction between the charge and the nucleus. Moreover, we define the macroscopic polarization $\mathbf{P}(t)$:

$$\mathbf{P}(t) = N\boldsymbol{\mu}(t) \tag{2.6.16}$$

In the linear response limit - i.e.low intensity field and harmonic binding potential energy - $\mathbf{P}(t)$ is related to $\mathbf{E}_o$ by:

$$\mathbf{P}(t) = \epsilon_0 \chi^{(1)} \mathbf{E}_0(t) \tag{2.6.17}$$

where $\epsilon_0 = 8.85 \cdot 10^{-12} F \cdot m^{-1}$ is the electric permittivity in the vacuum and $\chi^{(1)}$ is the first-order electric susceptibility and represents the efficacy to perturb all the electronic charge density out of their equilibrium condition. Generally, $\chi^{(1)}$ is a second rank tensor but, without loss of generality, we assume that the crystal is isotropic so that $\chi^{(1)}$ is represented by a scalar. The driving frequency of a visible electromagnetic field is in the THz region, causing only the motion of the electronic density, i.e. the nucleus are too heavy to adiabatically follow the field and the electronic resonances are due to the electrons. Despite of it, the electronic density

adiabatically adjusts to the nuclear motion to minimize the energy of the system. Hence, the induced dipole is related to $\mathbf{E}_0$ by the electronic polarizability $\alpha(t)$:

$$\boldsymbol{\mu}(t) = \alpha(t)\mathbf{E}_0(t) \tag{2.6.18}$$

As $\alpha(t)$ varies with the nuclear motion, it can be expanded as a Taylor series in the atomic displacement $\boldsymbol{Q}(t)$. At first order in $\boldsymbol{Q}(t)$, we have:

$$\alpha(t) = \alpha_0 + \left(\frac{\partial\alpha}{\partial\mathbf{Q}}\right)_0 \mathbf{Q}(t) \tag{2.6.19}$$

$\partial\alpha/\partial Q$ indicates how the polarizability α spatially changes in the molecule and the subscript 0 stands for the equilibrium position of the atoms. A given atomic vibration can be decomposed into a sum of normal modes (i.e.phonons), therefore the nuclear motion can be approximated, without loss of generality, as a phonon of frequency ω_v and wavevector $\mathbf{k}$:

$$\mathbf{Q}(t) = 2\mathbf{Q}_0 \cos(\omega_v t - \mathbf{k}\cdot\mathbf{r} + \phi) \tag{2.6.20}$$

Substituting Eqs. 2.6.18 and 2.6.19 and 2.6.20 into Eq. 2.6.16 and assuming that the incident field $\mathbf{E}_0(t)$ is monochromatic, $\mathbf{E}_0(t) = \mathbf{A}e^{-i(2\pi\nu_0 t - \mathbf{k}_i\cdot\mathbf{r})} + c.c.$, we have:

$$\begin{aligned}\mathbf{P}(t) =& N\alpha_0\mathbf{A}cos(2\pi\nu_o t - \mathbf{k}_i\cdot\mathbf{r}) + \\ &+N\left(\frac{\partial\alpha}{\partial\mathbf{Q}}\right)_0 \cdot \frac{\mathbf{Q}_o\mathbf{A}}{2}(cos[2\pi(\nu_o - \nu_{vib})t - (\mathbf{k}_i + \mathbf{k})\cdot\mathbf{r}] + \\ &+cos[2\pi(\nu_o + \nu_{vib})t - (\mathbf{k}_i - \mathbf{k})\cdot\mathbf{r}])\end{aligned} \tag{2.6.21}$$

The linear polarization $\mathbf{P}$, induced on the sample by electromagnetic field E_o, is given by the sum of three terms, depicted in Fig. 2.8:

- The elastic component (Rayleigh scattering) oscillates with the same frequency ν_i of the incoming electric field and it has the same wavevector $\mathbf{k}_i$.
- The Antistokes term oscillates with a frequency $\nu_s = \nu_i + \nu_{vib}$ and has a wavevector $\mathbf{k}_s = \mathbf{k}_i + \mathbf{k}$. This component is blue-shifted and it is associated to the annihilation of a phonon of frequency ν_{vib} and wavevector $\mathbf{k}$.
- The Stokes term oscillates with a frequency $\nu_s = \nu_i - \nu_{vib}$ and has a wavevector $\mathbf{k}_s = \mathbf{k}_i - \mathbf{k}$. This component is red-shifted and it is associated to the creation of a phonon of frequency ν_{vib} and wavevector $\mathbf{k}$.

Notably, a normal mode of the sample is Raman-active if the polarizability is changed during the vibration, i.e. $\partial\alpha/\partial Q \neq 0$ [97]; actually there must take place a change in the shape, dimension or orientation of the electronic distribution.

Otherwise, any Raman signatures are observed. In addition, Eq. 2.6.21 highlights the two fundamental relations for Raman scattering: energy and momentum conservation.

$$\nu_i = \nu_s \pm \nu_{vib} \tag{2.6.22}$$

$$\mathbf{k}_i = \mathbf{k}_s \pm \mathbf{k}_{vib} \tag{2.6.23}$$

The process just depicted corresponds to first-order Raman process because it involves only one-phonon. However, the description can be easily extended to higher orders in $\mathbf{Q}$, rising to multiple-phonon Raman scattering. Remarkably, Eq. 2.6.23 shows another important properties of Raman scattering: one-phonon Raman scattering in crystals probes only zone-center phonons, i.e. phonons with $\mathbf{q} \sim 0$. However, multiple-phonon processes can still probe others points of the first Brillouin zone but the total phonon wavevector must be equal to zero [98].

The intensity of the scattered radiation I_s can be calculated from the time-averaged power radiated by the induced polarizations $\mathbf{P}$ into unit solid angle. It will depend on the polarization of the scattered radiation $\mathbf{e}_s$, es, as $|\mathbf{P} \cdot \mathbf{e}_s|^2$. We deduce that I_s is proportional to:

$$I_s \propto \nu_s^4 |\mathbf{e}_i \cdot \left(\frac{\partial\alpha}{\partial\mathbf{Q}}\right)_0 \mathbf{Q}_0 \cdot \mathbf{e}_s|^2 \tag{2.6.24}$$

where $\mathbf{e}_i$ is the polarization of the incident radiation. Notice that the scattered intensity is proportional to the vibration amplitude Q squared. In other words, there will be no scattering if no atomic vibration is present. Moreover, I_s depends on the forth power of ν_s. Consequently, short wavelenghts are scattered more efficiently than the longest ones.

We can now define a complex second rank tensor, the Raman tensor, as:

$$\mathcal{R} = \left(\frac{\partial\alpha}{\partial\mathbf{Q}}\right)_0 \frac{\mathbf{Q}_0}{|\mathbf{Q}_0|} \tag{2.6.25}$$

and the Raman intensity can be expressed as:

$$I_s \propto \nu_s^4 |\mathbf{e}_i \cdot \mathcal{R} \cdot \mathbf{e}_s|^2 \tag{2.6.26}$$

Notably, the scattering radiation vanishes for certain choices on the incident and scattered polarizations. These so-called Raman selection rules are very useful for determining the symmetry of Raman-active phonons. The simplest example of Raman selection rules can be found in centrosymmetric crystals. In these crystals, phonons can be classified as having even or odd parity under inversion. Since the crystal is invariant under inversion, its tensor properties, such as $(\partial\alpha/\partial Q)$, should remain unchanged under the same operation. On the other hand, the phonon displacement vector Q of an odd- parity phonon changes sign under inversion, implying that $(\partial\alpha/\partial Q)$ changes sign. Hence the Raman tensor of odd-parity phonons in centrosymmetric crystals (within the approximation that the phonon wavevector is zero) must vanish [98].

2.6.2 The quantum description

Classical description of Raman scattering in condensed matter is similar to that in molecules, but it refers to the atomic vibrations in terms of phonons. Nevertheless, the main differences, occuring when substituting a discrete level system with an energy band one, could be enlightened by introducing microscopic quantum theory. To describe microscopically the inelastic scattering of light by phonons in a semiconductor, we have to specify the state of the three systems involved: incident and scattered photons with frequencies ω_i and ω_s, respectively; the electrons in the semiconductor and the phonons involved in the scattering. The scattering proceeds in three steps [98, 99]:

- The incident photon excites the semiconductor from an initial state $|i\rangle$ into an intermediate state $|a\rangle$ by creating an electron-hole pair (or exciton), via the electron-radiation interaction Hamiltonian, $\mathcal{H}_{eR}$.
- This electron-hole pair is scattered into another intermidiate state $|b\rangle$ (e-h pair) by emitting (Stokes) or annihiliting (Antistokes) a phonon of frequency ω_{vib} via the electron-phonon interaction Hamiltonian (EPC), $\mathcal{H}_{EPC}$.
- The electron-hole pair in $|b\rangle$ recombines radiatively with emission of the scattered photon ω_s.

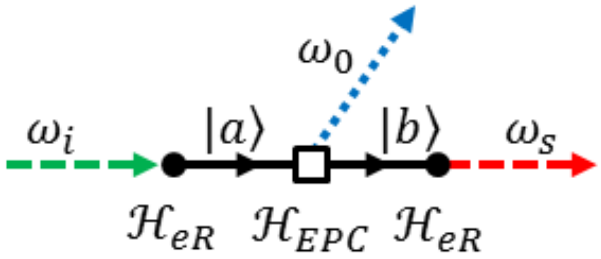

Figure 2.9: Feynman diagram of the Raman Stokes process described in the main text. The incident (ω_i) and scattered (ω_s) light are represented with green and red dashed arrows. The emitted phonon has a frequency ω_0 and it corresponds to the blue dashed arrow. $|a\rangle$ and $|b\rangle$ are the two electronic intermediate states. The vertex corresponds to the quasiparticles interaction: the Hamiltonian involved in each vertex is indicated.

The intermediate states $|a\rangle$, $|b\rangle$ can be either real states (i.e. they correspond to eigenstates of the system) or virtual states (i.e. they do not coincide with any eigenstates of the system). Notably, virtual transitions do not have to conserve energy, although they still have to conserve momentum. If at least one of these two states is real, the process is said to be resonant.

Feynman Diagrams

As long as all the interactions in the above Raman scattering processes are weak, the scattering probability (for phonons) can be calculated with third-order perturbation theory [99]. However, it is not a trivial matter to enumerate all the terms involved in such a third-order perturbation calculation. This is usually done, systematically, with the help of Feynman diagrams. The rules for drawing Feynman diagrams are [98, 99]:

- Excitations such as photon, phonons and electron-hole pairs in Raman scattering are represented by lines (or propagators).
- The intersection between two propagators represents the interaction between the corresponding excitation.

- The annihilation or creation of a quasiparticle in the interaction is indicated by the excitation propagator with an arrow. When the arrow points towards a vertex, the excitation is annihilated. Otherwise, it is created.

- Once a diagram has been drawn for a certain process, other possible processes are derived by permuting the time order in which the vertices occur in this diagram.

An example of Feynman diagram of the Raman Stokes process is shown in Fig.2.9. The probability to scatter a system from the initial state $|i\rangle$ can be derived, via the Fermi Golden Rule [98, 99]. In the case depicted in Fig.2.9, we have:

$$I_s \propto \left| \sum_{|a>,|b>} \frac{< i|\mathcal{H}_{eR}(\omega_s)|b >< b|\mathcal{H}_{EPC}|a >< a|\mathcal{H}_{eR}(\omega_i)|i >}{[\hbar\omega_i - (E_a - E_i)][\hbar\omega_i - \hbar\omega_0 - (E_b - E_i)]} \right|^2 \times \delta[\hbar\omega_i - \hbar\omega_0 - \hbar\omega_s] \tag{2.6.27}$$

where E_i , E_a and E_b are the energy of the states $|i\rangle$, $|a\rangle$ and $|b\rangle$, respectively. The δ-function indicates the energy conservation condition. Note that the summation on all the possible intermediate states $|a\rangle$ and $|b\rangle$ has to be taken into account. To have the complete response, it is necessary to consider all the six terms of the series, calculated in Ref. [98, 99].

Stokes and Antistokes intensites ratio

Classically, the probability of Stokes and Antistokes processes is the same. On the contrary, the quantum theory shows that the probability to annihilate or create a phonon depends on the phonon statistics, which is given by the Bose-Einstein distribution function [98–100]. At a given temperature T, the average number of phonons $n_{vib}(T)$ with energy E_{vib} is given by:

$$n_{vib}(T) = \frac{1}{exp\left(\frac{E_{vib}}{k_B T}\right) - 1} \tag{2.6.28}$$

where $k_{\mathrm{B}} = 1.38{\cdot}10^{-23}\mathrm{J\ K^{-1}}$ the Boltzmann constant. The probability for the Stokes and Antistokes processes differs because in the Stokes process the system goes from n_{vib} phonons to $n_{vib} + 1$, while in the Antistokes process the opposite occurs. Using time reversal symmetry, the matrix elements for the transition from n_{vib} to $n_{vib} + 1$

(Stokes) and from $n_{vib}+1$ to n_{vib} (Antistokes) are the same, and the intensity ratio between the Stokes (I_s) and Antistokes (I_{as}) signals are:

$$\frac{I_s}{I_{as}} \sim \frac{\omega_s^4}{\omega_{as}^4} exp\left(\frac{E_{vib}}{k_B T}\right) \propto \frac{n_{vib}+1}{n_{vib}} \tag{2.6.29}$$

Note that the impact of the ratio $\frac{\omega_s^4}{\omega_{as}^4}$ is typically much smaller thanthe exponential thus I_{as} is expected to be less intense than I_s, a condition which is ubiquitously observed in most material systems. Moreover, Raman spectrum can be used as a thermometer for the sample, just by considering the ratio $\frac{I_s}{I_{as}}$, which depends univocally on T. Indeed, for $T \to \infty$ the ratio is equal to 1 and the two intensities are equal, as in the classical case. It is important to remember that the time reversal assumption does not hold when resonance Raman scattering with sharp energy levels takes place. In this case, strong deviations from Equation 2.6.29 can be observed [101–103].

2.7 Raman spectroscopy in graphene

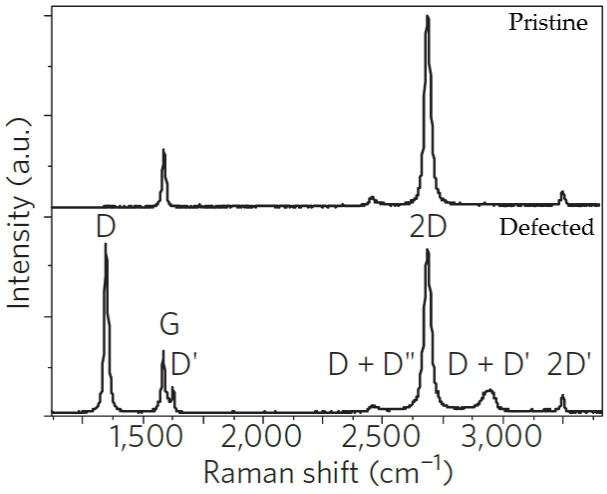

Figure 2.10: SLG Raman spectra in pristine (top panel) and defected (bottom panel) case. (Adapted from Ref [12]).

The first researches about Raman processes in solids can be dated back to 1960s [104,105], but graphene differs from usual semiconductors in several aspects. First of

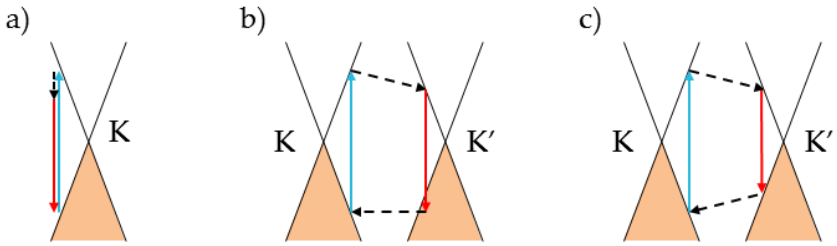

Figure 2.11: Examples of Dirac cone formalism applied to three Raman processes responsable for G (a), D (b) and 2D (c) modes.

all, the linear gapless electronic dispersion implies resonances for any laser frequency ω_i. Secondly, excitons cannot be intermediate states due to the gapless energy dispersion. Third, in the IR-visible range the electronic spectrum has approximately symmetric conduction and valence bands, while in semiconductors we can often consider the following inequality $m_h \gg m_e$ for effective mass m of holes and electrons [12].

The first Raman spectrum of graphite was measured in 1970 [106], but the full theoretical understanding of this spectrum was only achieved in the years 2000-2010 [39]. In 2006 [107] the first Raman spectrum of isolated monolayer graphene was performed. The SLG Raman spectra, shown in Fig.2.10, appears extremely simple: just a couple of very intense bands in the $1000 - 3000$ cm^{-1} region and few other overtones. Nevertheless, their shape, intensity and position allows us to deeply characterize our sample (e.g. number of layers, presence of defects, fermi energy), becoming a powerful probe in analysing both vibrational and electronic properties [12].

Dirac cone formalism [12] is a powerful understanding tool able to reproduce the main effects on the Raman spectrum. This graphical description, shown in Fig. 2.11, is set in the energy (y-axis) - momentum (x-axis) space. Solid black lines represent SLG electronic dispersion, i.e. the Dirac cones at K and K' vertices. Band population is associated to occupied states (shaded areas). Interband transition are accompanied by photon absorption (blue arrows) and emission (red arrows). Phonon emission corresponds to intraband transitions (dashed arrows). Defect activated

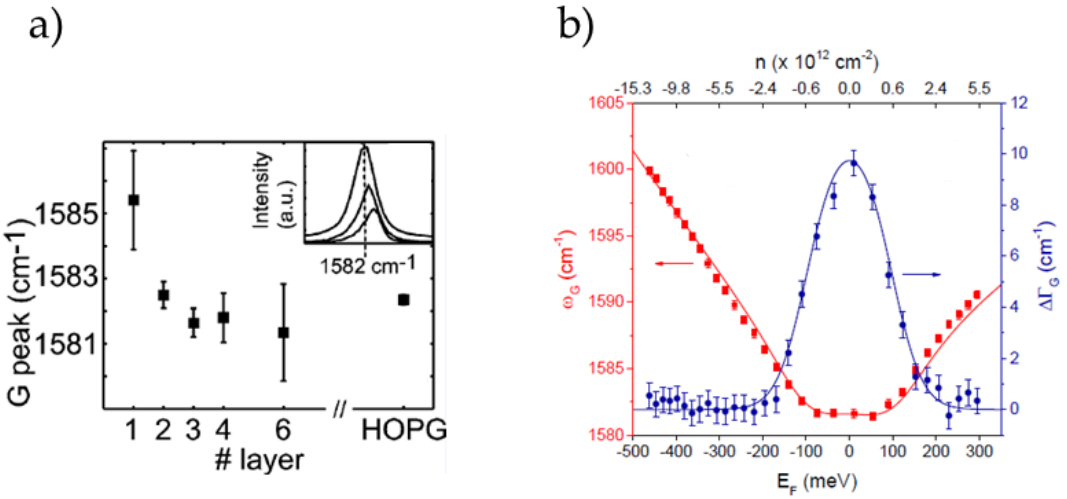

Figure 2.12: a) Frequency of G mode vs number of stacked layers. The inset shows the G peak for HOPG (upper peak), double- (middle peak), and single-layer (lower peak) graphene. The vertical dashed line indicates the reference value for bulk graphite. (Adapted from Ref. [108]). b) POS(G) and FWHM(G) at room temperature as a function of electron concentration and E_F. Red squares and blue circles indicated the experimental data, while blue and red line derives from the calculation. (Adapted from Ref. [109]).

processes imply the electron scattering on a defect, formalized as a phonon with zero energy (horizontal dotted arrows).

In the following we will briefly describe the main features of graphene Raman spectrum and explain the principal mechanisms that contribute to it.

One-phonon process: G-band

The G peak [110] is due to the in-plane bond stretching of sp^2 atoms in graphene layer and it is attributed to E_{2g} point symmetry, corresponding to Γ vertice in the first Brillouin zone. It is the only one-phonon mode in the $1000 - 3000$ cm^{-1} region, that satisfies the correct symmetry and wavevector conservation, as $\mathbf{q} \sim 0$. This phonon is deeply correlated to the number of layers n; indeed the G-band intensity decreases with n (see Fig.2.12.a), while different researches shows that its peak position, which is about 1580 cm^{-1} in graphite, depends on n, observing a redshift

as it increases [108, 111, 112].

Aother significant parameter, which affects the G mode in the Fermi energy E_F. Actually, it is well-known that graphene is a zero-gap semiconductor that becomes a metal if its Fermi energy is tuned applying a gate voltage [8]. By doping graphene, the change in the Fermi surface moves the Kohn anomaly away from $q = 0$, inducing a stiffening of the Raman G peak [9] (see Fig.2.12.b). At the same time, the sharpening of the FWHM occurs because of the blockage of the decay channel of phonons into electron-hole pairs due to the Pauli exclusion principle, when the electron-hole gap becomes higher than the phonon energy [113].

Finally, edges can be viewed as extended defects, breaking the translational symmetry, even though a perfect zigzag or armchair edge still preserves the translation symmetry along the edge. Then, the G peak can be modified near an edge. The edge changes the electronic states, which affects the EPC correction to the phonon frequency and electron-phonon and electron-photon matrix elements. This produces a strong polarization dependence of G-band intenisity and dependence of its position on laser spot location [114].

One phonon 2nd order scattering: D-band mode

The D peak of graphene is found at approximately 1350 cm^{-1} and it involves phonons with $|q| \approx |K|$ or $|K'|$. As shown in Fig.2.11.b, it is activated by the presence of defects,then it is proportional to the number of defects in the lattice and its intensity, compared to the intensities of the other peaks, is an extremely good indicator of the quality of the graphene sheet; in fact, ideally, a pristine graphene sheet should have no D peak whatsoever (see Fig.2.10). In their work, Ferrari et al. [115] introduced a three stage classification of disorder, that allows to explain the evolution of the spectrum, in terms of defects and disorder. Moreover, edges could be considered as extended defects, as they break translational symmetry. It follows that they activate D peak too. Nevertheless, it is demonstrated that due to translational invariance along the edge, a perfect zigzag edge cannot scatter electrons in intravalley mechanisms preventing the presence of the D mode [114].

Two phonon 2nd order scattering: 2D-band mode

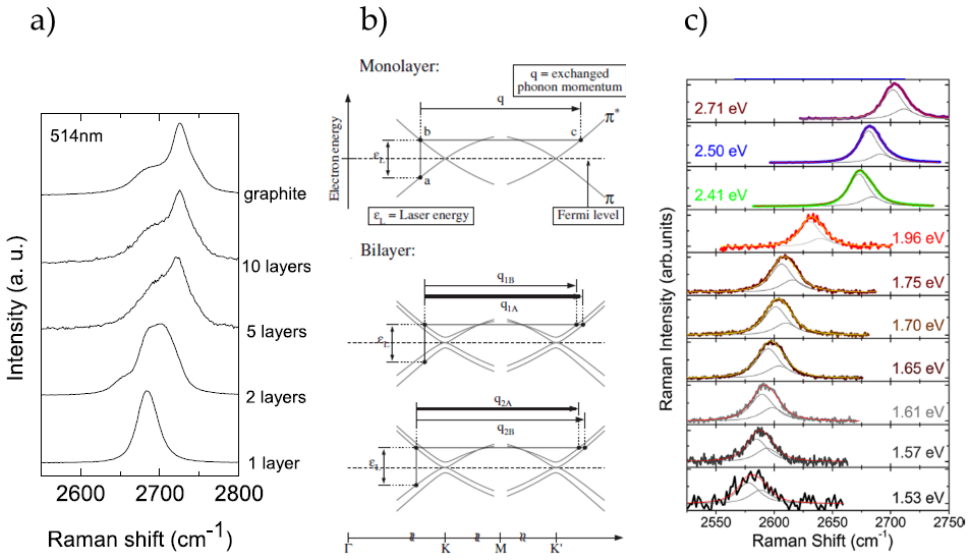

Figure 2.13: a) Evolution of the spectra at 514 nm with the number of layers n. (Adapted from Ref. [107]). b) Double Resonant mechanisms for the 2D peak in single layer (upper panel) and bilayer (lower panel). (Adapted from Ref. [107]). c) Raman 2D-mode spectra measured for laser photon energies in the range $1.53-2.71$ eV on the supported graphene. (Adapted from Ref. [117]).

Double resonance involves two phonons of opposite momenta and all the excited state electron scattering events are inelastic, as no defects are required for their activation. Graphite peaks, labeled as 2D ($\sim$ 2700cm^{-1}) and 2D' ($\sim$ 3250cm^{-1}), originate from 2-phonon double resonance and they are always observable in sp^2 Raman spectra [48, 116].

The double resonant Raman process is particularly suitable for the determination of number of layers n and relative orientations, as it is closely linked to the details of the electronic band structure. This appears extremely clear if we consider the bilayer graphene (BLG), shown in Fig.2.13.a-b. In fact, the interaction of the graphene planes causes the π and π^* bands to divide into four bands, with a different splitting for electrons and holes. The incident light couples only two pairs of the four bands, while the two almost degenerate phonons in the highest TO optical branch couple all electron bands, giving rise to four processes involving phonons with different momenta. Due to the phonon dispersion around K, they correspond to

different frequencies, that give four 2D peaks in bilayer graphene [107] (Fig.2.13.a). Making the same analysis for trilayer graphene, it is demostrated that the number of allowed Raman peaks in the 2D band is fifteen. It can be noticed that, increasing n until we reach the bulk graphite, the high frequency side of the 2D band has an higher intensity than for fewer graphene layers. Nevertheless, not all multilayers are Bernald stacked: then, it is possible to observe more complex 2D peak shapes in samples grown for example by chemical vapour deposition [37, 118].

The 2D peak shows a dependence of its position due to the character of the doping; in fact it shifts to lower frequencies under a high electron concentration (n-doping), while it is redshifted in presence of a high hole concentration (p-doping). For this reason, it is a powerful means to define the sign of the charges [113].

Another important aspect is the dependance of POS(2D) with laser energy ω_i [12, 116, 117, 119]:

$$\Delta POS(2D) = \frac{dPOS(2D)}{d\omega_i} = 2\frac{v_q^{TO}}{v_F} \approx 100\text{cm}^{-1}\text{eV}^{-1} \tag{2.7.30}$$

It is clear that there exist many other mechanisms that could influence the Raman spectra of graphene, such as the effects of perturbations, the presence electric and magnetic fields, the strain, the presence of functional groups, the temperature, the excitation energy and the polarization of the incoming light. Although they go beyond the purpose of this thesis, a wide dissertation can be found in many reviews about the subject [12, 37].

2.8 Beyond graphene: towards heterostructures-based devices

The emergence of the new two-dimensional materials (2DMs) scientific community is due to the unique electronic, optical, vibrational, thermal, mechanical and chemical properties of these systems. Many of these properties can be swiftly controlled, e.g. by means of electrostatic gating or optical stimuli. Beyond the rise of graphene [8], the more recent (re)discovery of the vast family of transition-metal dichalcogenides (TMDCs) [120, 121], has fuelled an unprecedented cross-disciplinary research effort.

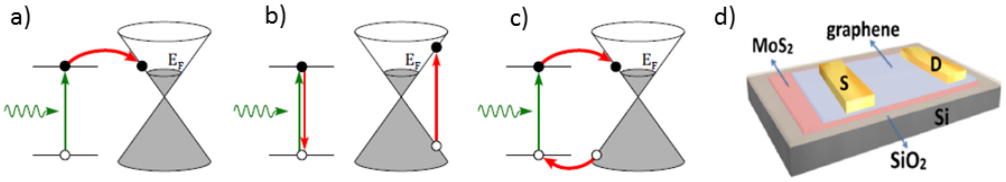

Figure 2.14: Schematic illustration of charge transfer (a), F$\acute{}$orster energy transfer (b) and Dexter energy transfer between a two-level system and a graphene monolayer (Adapted from Ref. [124]). Three-dimensional schematic view of a vdWH device (d) made of a monolayer graphene on top of a monolayer MoS_2 (Adapted from Ref. [125]).

2DM, such as graphene, boron nitride (BN) or semiconducting TMDs (thereafter denoted MX_2, with M=Mo, W, Re and X = S, Se, Te) are composed of covalently bonded atomic layers that stack, due to weak Van der Waals interactions.

Actually, although bulk MX_2 are semiconductors with an indirect bandgap, quantum confinement leads to a peculiar transition from indirect to direct bandgap that occurs at monolayer thickness [122] in several MX_2. These MX_2 are thus endowed with unique optical, opto-electronic, and also valley properties [121, 123]. In order to design efficient devices, one has to explore the intrinsic response of isolated monolayers, and their evolution in more complex environments.

In this stimulating context, graphene, MX_2 and BN are choice building block for van der Waals heterostructures (i.e., mechanically stacked layers of 2DM) (vdWH) [126,127]. VdWH exhibit atomically thin interfaces that are fundamentally different from the conventional metal-semiconductor (Shottky) barriers or p-n junctions. Recent demonstrations of hybrid graphene-MX_2 photodetectors, two-dimensional MX_2-M'X'_2 p-n junctions and light-emitting diodes (for reviews, see [68,121]) are illustrating the rapid progress of this field towards optoelectronic applications. VdWH-based devices are governed by band alignment, interactions with the underlying substrate, and near-field quantum phenomena, such as photoinduced-interlayer charge transfer (ICT) and energy transfer (IET). For instance ICT is the key process that leads to photodetection and it corresponds to the spatial transfer of the photoexcited electron from the two-level system of the donor MX2 to an available state with lower energy

in the acceptor graphene sheet. IET can be described in terms of direct transfer of energy from the photoexcited electron in the two-level system to graphene through dipole-dipole interaction (F*ö*rster-type dipole-dipole interaction) or as the transfer of two opposite charge, leading to no macroscopic charge transfer (Dexter-type electron-exchange); it is very useful for energy harvesting or color conversion.

In practice, although evidence for photo-induced ICT has been reported in MX_2-M'X'_2 heterostructures [128] and graphene-MX_2 heterostructures [125, 129], quantitative investigations (transfer timescale, efficiency) of IET and ICT in vdWH remain scarce. Preliminary results [130] show the great potentiality of Raman Spectroscopy to address IET and ICT jointly, as it is an accurate tool to quantitatively measure the charge carrier density in graphene [12]. Thus, these heterostructures could represent a powerful outlook for the non-linear and Raman techniques shown in this work. Actually, our setup could unveil the role of photoexcitation, by working at different fluence of the incoming beam and tuning the wavelength of the involved electric fields, in order to evaluate the presence of additional mechanisms such as exciton-exciton annihilation or saturation effects.

Part II: Results

Chapter 3

Narrowband CARS in graphene

Coherent Raman imaging (CRI) has aroused great interest in the last decades and these methods are now poised to begin emerging as widely used tools for obtaining functional information. Notably, a great deal of efforts is still put in this field. They are addressed to three significant prospectives that could make them prevail over the Spontaneous Raman counterpart [131]. First of all, the recent development of new time and Fourier-domain techniques and alternative detection schemes [132–134] are aimed to go beyond the current performances. Indeed, it requires to reach faster acquisition speed and to generate good quality signal over the largest possible spectral range. Nowadays, the majority of the CRI methods can reach speed of approximately 10 μs per cm^{-1} in biological samples, similarly to the best spontaneous systems, but still have to find a compromise with the desired spectral coverage [135]. In addition, CRI are largely employed in lipids imaging [136], which has a key role in the diagnostics of several diseases such as atherosclerosis and cancer. They are actually posited as a viable surgical guidance tool too [135]. Nevertheless, in order to introduce these tools beyond the lab setting, it is necessary to develop a new technology able to realise portable, cheap and user-friendly equipments. Nowadays, there exist many Spontaneous Raman spectrometers able to bring simplicity to Raman measurements without compromising the ability to handle even the most complex samples . Indeed they are involved in everyday life, such as hospitals, airports and forensic science. The case of CRI is more complex due to the requirement of pulsed excitations and a new application is still far away [137]. Finally, even if in the biological field a wealth

of studies has demonstrated that CRI can surpass Spontaneous Raman in terms of pixel acquisition times, allowing for video rate imaging, relatively less studies have been reported in nanostructured materials (e.g. micro- and nano-structured polymer materials, structured metals, organic microcrystallites, single wall carbon nanotubes highly oriented pyrolytic graphite) [138].

Graphene, in the role of layered material with high third order non-linearity, is capturing the attention in Coherent Raman studies as a response to the last two issues. Indeed, it has been proposed as active medium for the realization of synchronized all-fiber laser for coherent Raman spectroscopy [139]. Actually, due to its compactness and all-optical synchronization, this is an ideal source for CRI and it could be implemented in a portable equipment supplied by microscope and detection, as expected in the goals of "Graphene Flagship, Core 2".

In particular, this work, content of the chapter, is aimed to shed light on the graphene Coherent anti-Stokes Raman Scattering (CARS) response and how to exploit it to develop an imaging protocol with chemical selectivity. Indeed, despite the large $\chi^{(3)}$, no CARS peak profiles, equivalent to those observed Spontaneous Raman, have been observed to date to the best of our knowledge. Ref. [140] reported a dip in the third order non linear spectral response of SLG at the G phonon frequency. This was interpreted as an anomalous anti-resonance and phenomenolocally described it in terms of Fano lineshape, i.e. a coupling between the electronic continuum and a discrete phonon state [141]. Here, we address this effect to the interference between CARS signal and another third-order process, the NVRB, and we associate a key role to the resonant process, due to SLG gapless behaviour in the light-matter interaction.

3.1 A brief roadmap towards Coherent Raman Microscopy

The optical microscope has been widely used for materials and biological imaging: optical contrast provided by the light transmitted through the sample, in its original version, is not directly related to the chemical structure of the specimen. The signal

is analysed through a magnification system and the resolution is subject to the diffraction limit. In fact, the probe wavelength introduces a spatial resolution, which represents a limit for the experiment.

Beside the obvious resolution issues, contrast (i.e. the ability to discriminate the sample from the surroundings) is the most critical parameter in optical microscopy and several efforts have been devoted to develop novel microscopic protocols able to superseed such limitation. In this respect, fluorescence microscopy offers the advantage that, neglecting other sources of background signal, such as Raman scattering, the spectral shift of the fluorescence signal makes it a zero-background detection scheme. However, it is often necessary to introduce a label to create contrast by staining the sample with fluorescent marker molecules [142]. Nevertheless, staining could alter the physiological environment of the sample in an irreversible way. Furthermore, the main issue encountered in fluorescence microscopy is that fluorophores lose their ability to fluoresce due to a process called photobleaching. This photobleaching phenomenon can severely limit the time over which a sample can be observed by fluorescence microscopy. On the other hand, its resolution has significantly increased after the introduction of the confocal geometry [143]. Unfortunately both conventional optical and fluorescence microscopy are not chemically selective [144], i.e. it is not possible to discriminate different areas of the sample on account of their chemical bonds.

Vibrational contrast mechanisms, based on infrared and spontaneous Raman scattering spectroscopies, allow for label-free, non-invasive chemically selective imaging, as different molecules oscillate at their specific frequencies. However, as clarified in Chapter 2, the cross section of such processes is low, leading to small signal intensities and long acquisition times.

The development of ultrashort laser pulses made possible the exploration of nonlinear optical effects as means of contrast generation in label-free microscopy. A first step has been to develop imaging techniques based on Two-Photon Excited Fluorescence (TPEF), Second Harmonic Generation (SHG), Third Harmonic Generation (THG) and Two Photon Absorption (TPA) [145]. However, they are still affected by some of the drawbacks indicated above, such us the absence of chemical sensitivity.

More recently, CRI has emerged as the way to superseed all such limitations. Due to the nonlinear dependence of the detected signal on the input fields, the signal is emitted only within a small volume around the focal point, introducing 3D imaging capability. Moreover these intense radiation sources enable the generation of nonlinear effects due to coupling with vibrational modes, exciting molecules coherently; it establishes a definite phase relation between the amplitudes of wavefunctions of the target molecules, enhancing the overall emitted signal. In addition the spatial coherence of the incident laser pulse creates a definite spatial distribution, which results in a spatial coherence in the scattered signal leading to a directional emission [146].

Coherent Raman Spectroscopy (CRS) is based on interaction of the three fields, coordinated in time and space [147]: in the degenerate case, there are only two Raman pulses, called the pump pulse (PP at frequency ω_p) and the Stokes pulse (SP at frequency ω_s). Their frequency difference must be equal to a Raman-active vibrational mode of the sample $\Omega = \omega_p - \omega_s$. This inelastic interaction can be described in terms of a nonlinear four-wave mixing (FWM) process, related to third-order polarizability [146]:

$$P_{\alpha}^{(3)}(k_{CRS}, \omega_{CRS}) = \chi_{\alpha\beta\gamma\delta}^{(3)}(\omega_{CRS}, \omega_p, -\omega_s, \omega_p)\, E_{\beta}(k_p, \omega_p)\, E_{\gamma}(k_s, \omega_s)\, E_{\delta}(k_p, \omega_p) \tag{3.1.1}$$

Among the possible Coherent Raman techniques we can distinguish:

- Coherent anti-stokes Raman Scattering (CARS) [135]: In CARS, a new spectral component $\omega_{as} = 2\omega_p - \omega_s$ is produced during the interaction; neglecting the non-vibrationally resonant background (NVRB), whose role will be extensively debated in the next sections, the signal is background free and it can be analysed with homodyne detection.

- Stimulated Raman Scattering (SRS) [135]: SRS is characterized by the detection of Raman gain on Stokes signal: as it is a weak change, it requires heterodyne detection, using modulator and lock-in amplifier.

- Raman Induced Kerr Effect Scattering (RIKES) [148]: If CARS and SRS can be often depicted as scalar interaction, RIKES detects the change of birifrangence in the sample, caused by the Raman Effect. Thus, the signal is

emitted at the same frequency as the incoming field, but with orthogonal polarization: the detection can be done by both homodyne or heterodyne methods.

Compared to spontaneous Raman scattering, CRS, in particular CARS, shows an enhancement of signal by a factor $10^2 - 10^5$ due to the stimulatation of molecular vibrations in phase. This improvement, along with a nonlinear dependence on the intensities of the incoming fields, permits faster acquisition times and the use of lower incident power, reducing sample damage. Moreover, the intrinsic nonlinearity of the process provides 3D sectioning of the sample, essential in imaging characterization protocols. Besides, incoherent techniques, like spontaneous Raman, scale as the molecular density N, while CARS signal is typically proportional to N^2, depending on the detection scheme, heterodyne or homodyne [146].

CARS case, though coherent signal allows easy separation from background fluorescence, is affected by the presence of NVRB, that distorts lineshape and reduces the chemical contrast. For this reason at low concentrations and low power, spontaneous methods may offer a sensitivity advantage, providing high-resolution broadband spectra, free from NVRB. However, unlike coherent techniques, they cannot take advantage of heterodyne schemes that have been shown to provide modest signal-to-noise improvements and sensitivity to lower concentration [149] .

3.2 Ultrashort pulse propagation

In Chapter 2, we have already discussed about the effect of an applied electric field $\mathbf{E}(t)$ on a system in the linear dipole approximation. Indeed, it determines the movement of positively charged particles in the direction of the field and negative charges in the opposite direction, inducing a series of electric dipole moments [146]. By adding up all the N electric dipoles per unit volume, the macroscopic polarization $\mathbf{P}$ is proportional to $\mathbf{E}$ [145, 150, 151]:

$$\mathbf{P}(\mathbf{r}, t) = \epsilon_o \chi^{(1)} \mathbf{E}(\mathbf{r}, t) \tag{3.2.2}$$

where ϵ_o is the permittivity of free space and $\chi^{(1)}$ is known as linear susceptivity. For stronger fields (i.e. the applied field is of the order of the field that binds the

electron to the atom $E_a \approx 2 \cdot 10^7$ esu), the electron is farther displaced from its equilibrium position; the binding potential can no longer be assumed harmonic as in the linear response condition. In this case, the dependence between the **E** and **P** is no more strictly linear; actually $\mathbf{P}(\mathbf{r}, t)$ can be written as a power series in the field to include the nonlinear electronic motions [145, 150, 151]:

$$\mathbf{P}(\mathbf{r}, t) = \epsilon_o \left[\chi^{(1)}\mathbf{E}(\mathbf{r}, t) + \chi^{(2)}\mathbf{E}^2(\mathbf{r}, t) + \chi^{(3)}\mathbf{E}^3(\mathbf{r}, t) + \dots\right] \tag{3.2.3}$$

where the quantities $\chi^{(n)}$ corresponds to nonlinear optical susceptibilities of n-th order. In order to describe the interaction between the electromagnetic field and matter, it is necessary to express $\mathbf{E}(\mathbf{r}, t)$, in terms of its temporal and spatial propagation. This can be seen from the following scalar wave equation form (Helmontz equation), which can be derived from Maxwell's equations, assuming the propagation of plane waves along the z-axis in free space [145, 150, 151]:

$$\frac{\partial^2 E(z,t)}{\partial z^2} - \frac{1}{c^2}\frac{\partial^2 E(z,t)}{\partial t^2} = \mu_o \frac{\partial^2 P(z,t)}{\partial t^2} \tag{3.2.4}$$

where $\mu_o = 4\pi \times 10^{-7} H \cdot m$ is the vacuum permeability. The time varying polarization $P(z, t)$ is on the right hand side of the equation, thus acts as a driving term for the electric field, modifying it during its propagation and generating new components. Let us assume a quasi-monochromatic electric field $E(z, t)$ in the plane wave form, propagating along the z-axis with a central frequency ω_o:

$$E(z,t) = \frac{1}{2}A(z,t)e^{i(\omega_o t - k_o z)} + c.c. \tag{3.2.5}$$

where $A(z, t)$ is the complex field envelope and k_o is the field wavevector. Referring to the Helmontz equation 3.2.4, $P(z, t)$ includes both linear and nonlinear terms:

$$P(z,t) = P_L(z,t) + P_{NL}(z,t) = p_L(z,t)e^{i(\omega_o t - k_o z)} + p_{NL}(z,t)e^{i(\omega_o t - k_p z)} \tag{3.2.6}$$

where k_p and $p_{NL}(z, t)$ are wavevector and the envelope of polarization wave, respectively. Eq. 3.2.4 can be more easily solved in the frequency domain by applying Fourier transform to the fields:

$$\tilde{E}(z,\omega) = \tilde{A}(z,\omega - \omega_o)e^{-ik_o z}, \tag{3.2.7a}$$

$$\tilde{P}_L(z,\omega) = \tilde{P}_L(z,\omega - \omega_o)e^{-ik_o z}, \tag{3.2.7b}$$

$$\tilde{P}_{NL}(z,\omega) = \tilde{P}_{NL}(z,\omega - \omega_o)e^{-ik_p z}. \tag{3.2.7c}$$

where the sign $\sim$ indicates the corresponding quantities in the frequency domain. In the same way we write the frequency domain version of Eq. 3.2.4:

$$\frac{\partial^2 \tilde{E}(z,\omega)}{\partial z^2} + \frac{\omega^2}{c^2}\tilde{E}(z,\omega) = -\mu_o \omega^2 \tilde{P}(z,\omega) \tag{3.2.8}$$

Note that we can express the derivatives with respect to the longitudinal propagation coordinate z as follow:

$$\frac{\partial^2 \tilde{E}}{\partial z^2} = \left(\frac{\partial^2 \tilde{A}}{\partial z^2} - 2ik_o \frac{\partial \tilde{A}}{\partial z} - k_o^2 \tilde{A} \right) \tag{3.2.9}$$

To allow a deeper analysis it is possible to make the so called Slowly Varying Envelope Approximation (SVEA); it consists in neglecting field variation of A over propagation lengths of the order of the wavelength and it breaks down only at extreme focusing condition; this means that $\partial^2 \tilde{A}/\partial z^2 \ll 2ik_o \partial \tilde{A}/\partial z$.

By merging Eqs. 3.2.7, 3.2.8 and 3.2.9, we obtain:

$$\begin{aligned} &- 2ik_o \frac{\partial \tilde{A}(z,\omega-\omega_o)}{\partial z} e^{-ik_o z} - k_o^2 \tilde{A}(z,\omega-\omega_o) e^{-ik_o z} + \frac{\omega^2}{c^2}\tilde{A}(z,\omega-\omega_o) e^{-ik_o z} = \\ &= -\mu_o \omega^2 \tilde{p}_L(z,\omega-\omega_o) e^{-ik_o z} - \mu_o \omega^2 \tilde{p}_{NL}(z,\omega-\omega_o) e^{-ik_p z} \end{aligned} \tag{3.2.10}$$

By keeping in mind that $P_L(z,\omega) = \epsilon_o [n^2(\omega) - 1]\tilde{A}(z,\omega)$, where $n(\omega)$ is the system refractive index, and observing that the second and the third term can be simplified on the left hand side, the previous equation can be expressed as follows:

$$2ik_o \frac{\partial \tilde{A}(z,\omega-\omega_o)}{\partial z} = \mu_o \epsilon_o \omega^2 [n^2(\omega) - 1]\tilde{A}(z,\omega-\omega_o) + \mu_o \omega^2 \tilde{p}_{NL}(z,\omega-\omega_o) e^{-i\Delta k z} \tag{3.2.11}$$

where $\Delta k = k_p - k_o$ is the wavevector mismatch between P_{NL} and E. Now, we notice that in a dispersive medium $n(\omega)$ is a function of the frequency and the wavevector, thus it becomes a nonlinear function of ω:

$$\mu_o \epsilon_o \omega^2 [n^2(\omega) - 1] = k^2(\omega) - k_o^2 = (k(\omega) - k_o)(k(\omega) + k_o) \approx 2k_o(k(\omega) - k_o) \tag{3.2.12}$$

The wavevector $k(\omega)$ can be expanded in Taylor series as a function of ω:

$$k(\omega) = k(\omega_o) + \left.\frac{\partial k}{\partial \omega}\right|_{\omega_o} (\omega - \omega_o) + \frac{1}{2}\left.\frac{\partial^2 k}{\partial \omega^2}\right|_{\omega_o} (\omega - \omega_o)^2 + \dots \tag{3.2.13a}$$

$$\left.\frac{\partial k}{\partial \omega}\right|_{\omega_o} = \frac{n(\omega_o)}{c} + \left(\frac{n}{c}\frac{\partial \omega}{\partial \omega}\right)_{\omega_o} = \frac{1}{c}\left[n(\omega_o) + \omega_o \left(\frac{\partial n}{\partial \omega}\right)_{\omega_o}\right] = \frac{n_g}{c} = \frac{1}{v_g} \tag{3.2.13b}$$

$$\left.\frac{\partial^2 k}{\partial \omega^2}\right|_{\omega_o} = \frac{\partial}{\partial \omega}\left(\frac{1}{v_g}\right) = -\frac{1}{v_g^2}\left(\frac{\partial v_g}{\partial \omega}\right)_{\omega_o} = GVD \tag{3.2.13c}$$

where v_g indicates the group velocity of the carrier frequency v_g, GVD the group velocity mismatch and n_g is the ratio between light velocity in tha vacuum and the group velocity in the medium. Note that a second-order approximation is sufficient for moderate pulse bandwidths. Substituting Eq. 3.2.13 into Eq. 3.2.11, we obtain:

$$\begin{aligned}\frac{\partial \tilde{A}(z,\omega-\omega_o)}{\partial z} =& -i\frac{1}{v_g}\tilde{A}(z,\omega-\omega_o)(\omega-\omega_o) - i\frac{GVD}{2}\tilde{A}(z,\omega-\omega_o)(\omega-\omega_o)^2 - \\ &- i\frac{\mu_o\omega_o c}{2n}\tilde{p}_{NL}(z,\omega-\omega_o)e^{-i\Delta kz}\end{aligned} \tag{3.2.14}$$

We can now retrieve the basic propagation equation in time domain by applying the inverse Fourier transform:

$$\frac{\partial A(z,t)}{\partial z} + \frac{1}{v_g}\frac{\partial A(z,t)}{\partial t} + i\frac{GVD}{2}\frac{\partial^2 A(z,t)}{\partial t^2} = -i\frac{\mu_o\omega_o c}{2n}p_{NL}(z,t)e^{-i\Delta kz} \tag{3.2.15}$$

This expression includes both dispersion and nonlinear effects in the pulse propagation. The group velocity mismatch produces the temporal chirping, responsible for pulse broadening; whereas $p_{NL}(z,t)$ shows up as the source term that drives and modifies the electric field [152] [151].

3.2.1 Four-wave mixing

In order to determine the temporal evolution of the electric field, we choose the retarded frame, which moves with the pulse at the group velocity v_g: indeed we can transform the coordinates accordingly: $z' \equiv z$ and $t \equiv t - z/v_g$.

$$\frac{\partial A(z,t)}{\partial z} = -i\frac{\mu_o\omega_o c}{2n}p_{NL}(z,t)e^{-i\Delta kz} \tag{3.2.16}$$

Moreover, broadening effects are typically negligible in the case of ps pulses and, accordingly, the GVD term has been neglected in Eq.3.2.14 [145]. Considering a centrosymmetric material ($\chi^{(2)} = 0$), let us focus on the Four-Wave Mixing (FWM) interaction, which is related to the third order susceptibility $\chi^{(3)}$:

$$P_{NL}(z,t) = P^{(3)}(\omega_4; \pm\omega_1 \pm \omega_2 \pm \omega_3) \sim \chi^{(3)}(\omega_4; \pm\omega_1 \pm \omega_2 \pm \omega_3)E^3(z,t) \tag{3.2.17}$$

where the notation $\chi^{(3)}(\omega_4; \pm\omega_1 \pm \omega_2 \pm \omega_3)$ is introduced to underline the different possible combination of the three interacting field and the corresponding energy

conservation. The total electric field $E(z,t)$ can be expressed as the superposition of four interacting field, given as:

$$E(z,t) = \sum_{j=1}^{3} A_j(z,t)e^{i(\omega_j t - k_j z)} + c.c. \tag{3.2.18}$$

After inserting Eq. 3.2.18 into Eq. 3.2.17, a large number of terms arises from $E^3(z,t)$. In the case of CRS processes, which we are interested in, we will focus on those terms characterized by the following energy conservation law:

$$\omega_4 = \omega_1 - \omega_2 + \omega_3 \tag{3.2.19}$$

The relevant nonlinear polarization for each field is expressed as:

$$P_{NL}^{\omega_1}(z,t) = \frac{3}{8}\epsilon_o\chi^{(3)}A_2^*(z,t)A_3(z,t)A_4(z,t)e^{i[(+\omega_2-\omega_3+\omega_4)t-(+k_2-k_3+k_4)z]} \tag{3.2.20a}$$

$$P_{NL}^{\omega_2}(z,t) = \frac{3}{8}\epsilon_o\chi^{(3)}A_1(z,t)A_3(z,t)A_4^*(z,t)e^{i[(\omega_1+\omega_3-\omega_4)t-(k_1+k_3-k_4)z]} \tag{3.2.20b}$$

$$P_{NL}^{\omega_3}(z,t) = \frac{3}{8}\epsilon_o\chi^{(3)}A_1^*(z,t)A_2(z,t)A_4(z,t)e^{i[(-\omega_1+\omega_2+\omega_4)t-(-k_1+k_2+k_4)z]} \tag{3.2.20c}$$

$$P_{NL}^{\omega_4}(z,t) = \frac{3}{8}\epsilon_o\chi^{(3)}A_1(z,t)A_2^*(z,t)A_3(z,t)e^{i[(\omega_1-\omega_2+\omega_3)t-(k_1-k_2+k_3)z]} \tag{3.2.20d}$$

where the factor 3/8 derives from the degeneracy factor, that involves all the possible permutations for the three distinct fields. Substituting each Eq. 3.2.20 one by one into Eq. 3.2.16, we derive four coupled wave equations for FWM processes, that describe many different processes with four interacting fields, such as CARS, SRS and RIKES:

$$\frac{\partial A_1(z,t)}{\partial z} = -i\alpha_1\chi^{(3)}A_2^*(z,t)A_3(z,t)A_4(z,t)e^{-i\Delta kz} \tag{3.2.21a}$$

$$\frac{\partial A_2(z,t)}{\partial z} = -i\alpha_2\chi^{(3)}A_1(z,t)A_3(z,t)A_4^*(z,t)e^{-i\Delta kz} \tag{3.2.21b}$$

$$\frac{\partial A_3(z,t)}{\partial z} = -i\alpha_3\chi^{(3)}A_1^*(z,t)A_2(z,t)A_4(z,t)e^{-i\Delta kz} \tag{3.2.21c}$$

$$\frac{\partial A_4(z,t)}{\partial z} = -i\alpha_4\chi^{(3)}A_1(z,t)A_2^*(z,t)A_3(z,t)e^{-i\Delta kz} \tag{3.2.21d}$$

where $\alpha_j = \frac{3\omega_i}{8cn_i}$ and $\Delta k = k_4 - k_1 + k_2 - k_3$ is the wavevector mismatch. It is important to notice that the effect of the driving term $P^{(3)}$ depends critically on the phase-matching condition: as the term $e^{-i\Delta kz}$ tends to unity ($\Delta kz \to 0$), it significantly increases. Furthermore, note that if we are in the degenerate case, wherein two or more frequency are equal, the number of equations decreases [145, 150, 151].

3.3 Coherent anti-Stokes Raman Scattering (CARS)

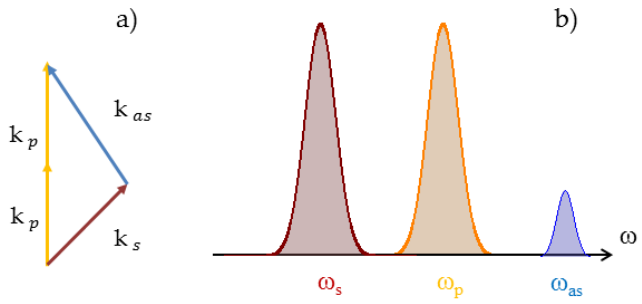

Figure 3.1: Phase matching condition for CARS process (a) and the output frequencies (b).

Coherent anti-Stokes Raman Scattering is associated to the $\chi^{(3)}$ [153]. The "two-color" CARS is a degenerate FWM process, because only two lasers are involved to excite the sample. Let us consider Eqs. 3.2.21; we introduce the pump (ω_p), Stokes (ω_s) and anti-Stokes (ω_{as}) frequencies, assuming that:

$$\begin{aligned} \omega_1 &= \omega_3 = \omega_p \\ \omega_2 &= \omega_s \\ \omega_4 &= \omega_{as} \end{aligned} \tag{3.3.22}$$

Eqs. 3.2.21 become:

$$\frac{\partial A_p(z,t)}{\partial z} = -i\alpha_p \chi^{(3)} A_p^*(z,t) A_s(z,t) A_{as}(z,t) e^{-i\Delta k z} \tag{3.3.23a}$$

$$\frac{\partial A_s(z,t)}{\partial z} = -i\alpha_s \chi^{(3)} A_p(z,t) A_p(z,t) A_{as}^*(z,t) e^{-i\Delta k z} \tag{3.3.23b}$$

$$\frac{\partial A_{as}(z,t)}{\partial z} = -i\alpha_{as} \chi^{(3)} A_p(z,t) A_s^*(z,t) A_p(z,t) e^{-i\Delta k z} \tag{3.3.23c}$$

where the phase matching term is equal to (see Fig.3.1.a):

$$\Delta k = k_{as} - (2k_p - k_s) \tag{3.3.24}$$

In order to find the solution, we can integrate eq. 3.3.23c over the sample length L:

$$\begin{aligned} \int_o^L dA_{as}(r,t) &= \int_0^L \left[-i\alpha_{as} \chi^{(3)} A_p A_s^* A_p e^{i\Delta k z} \right] dz = \\ &= -i\alpha_{as} \chi^{(3)} A_p A_s^* A_p \int_o^L e^{-i\Delta k z} dz \end{aligned} \tag{3.3.25}$$

Let us assume that PP and SP amplitudes are much larger compared than CARS signal, which is completely generated by the interactions of the two beams on the sample; we can suppose the following initial conditions: $A_{as}(0,t) = 0$, $A_s(r,t) = A_s \simeq const$ and $A_p(r,t) = A_p \simeq const$. It means that, according to the non-depletion assumption, the amplitudes A_p and A_s remain unchanged during the interaction.

$$A_{as}(L,t) = -i\alpha_{as}\chi^{(3)}A_pA_s^*A_pLe^{\frac{i\Delta kL}{2}}\,\mathrm{sinc}\left(\frac{\Delta kL}{2}\right) \tag{3.3.26}$$

The intensity of the generated signal at ω_{as} is given by [150]:

$$I_{as}(L,t) \propto |A_{as}(L,t)|^2 = \alpha_{as}^2|\chi^{(3)}|^2I_p^2I_sL^2\,\mathrm{sinc}^2\left(\frac{\Delta kL}{2}\right) \tag{3.3.27}$$

Equation 3.6.50 reveals the main features of CARS interaction:

- It is a nonlinear process, as it is directly proportional to I_p^2 and I_s.
- Since it depends on $|\chi^{(3)}|^2$, I_{as} is proportional to the square of the molecular density (N^2); in addition, as we will detail in the following, the squared dependence of $\chi^{(3)}$ strongly affects the spectral CARS response, due to the interplay between non-resonant and resonant $\chi^{(3)}$ terms.
- Although the signal is directly proportional to L^2, the phase-matching term $sinc^2\left(\frac{\Delta kL}{2}\right)$ introduces a limitation to the effective length, in which it is possible to gather nonlinear signal. In fact, the sinc function significantly decreases as its argument differs from 0. Hence the limit is given by the condition $\Delta kL_c < \pi$, where L_c is called "coherence interaction length". In order to collect as much signal as possible, the condition $L/L_c \to 0$ has to be satisfied. Iin the experimental setup tight focusing is generally preferred in order to relax the phase-matching condition [154]. In addition the phase-matching condition implies that CARS signal is normally only generated in a specific direction, at which constructive interference of the anti-Stokes field occurs.
- CARS interaction produces a new spectral component $\omega_{as} = 2\omega_p - \omega_s$ (see Fig.3.1.b), that can be counted with homodyne detection, using short-pass wavelength filters.

3.4 Light-matter interaction: a semi-classical approach

In the previous section, we have focused on CARS as a nonlinear optics process; now let us put more attention to the light-matter interaction to retrieve an analytical expression for $\chi^{(3)}$. The classical description of an active vibrational mode driven by the incident optical field is modelled by a damped harmonic oscillator at frequency ω_v, whose motion as a function of vibrational coordinate Q is expressed by the following equation [145, 146, 150, 151]:

$$\frac{d^2Q(t)}{dt^2} + 2\gamma\frac{dQ(t)}{dt} + \omega_v^2 Q(t) = \frac{F(t)}{m} \tag{3.4.28}$$

where γ is the damping constant, m is the reduced nuclear mass, and $F(t)$ is the external driving force of the oscillation from the incident optical fields, which in CARS process is given by:

$$F(t) = \left.\frac{\partial\alpha}{\partial Q}\right|_o E_p E_s^* e^{-i(\omega_p-\omega_s)t} \tag{3.4.29}$$

The incoming fields introduce a time-varying force that oscillates at their difference frequency $\omega_p - \omega_s$. Note that it is experienced by the nuclear mode: it is proportional to $\left.\frac{\partial\alpha}{\partial Q}\right|_o$, which is related to the coupling between electrons and phonons through the derivative of the polarizability α, analogously to the Spontaneous Raman case. We look for a solution of the equation that can be written as:

$$Q(t) = Q(\omega_p - \omega_s)[e^{-i(\omega_p-\omega_s)t} + e^{i(\omega_p-\omega_s)t}] \tag{3.4.30}$$

where $Q(\omega_p - \omega_s)$ is the amplitude of the molecular vibration. Substituting this expression in Eq. 3.4.28, it follows that this amplitude can be expressed as:

$$Q(\omega_p - \omega_s) = \left.\frac{\partial\alpha}{\partial Q}\right|_o \frac{E_p E_s^*}{m} \frac{1}{\omega_v^2 - (\omega_p-\omega_s)^2 - 2i\gamma(\omega_p-\omega_s)} \tag{3.4.31}$$

Hence, $Q(\omega_p - \omega_s)$ depends on the amplitudes of the applied light fields and on the magnitude of the coupling between the nuclear coordinate and the electronic polarizability $\left.\frac{\partial\alpha}{\partial Q}\right|_o$. Furthermore, when the frequency difference of PP and SP is equal to the resonant frequency ω_v, the molecular vibration of the active Raman mode will be resonantly enhanced.

The presence of the driven nuclear motion affects the optical properties of the material; in fact when a probe field passes through the medium, it will be modulated by the resonant molecular vibrational mode and, in CARS case, we look at the component generated at the anti-Stokes blueshifted frequency. In degenerate CARS PP provides also the probe field; so if we sum the contribution of all N dipoles we obtain the following expression for the total nonlinear polarization at frequency $\omega_{as} = 2\omega_p - \omega_s$:

$$P(t) = N\frac{\partial\alpha}{\partial Q}\bigg|_o Q(t)E_p(t) = P(\omega_{as})e^{-i(\omega_{as})t} \tag{3.4.32}$$

Consequently, we can deduce the expression for the amplitude of the nonlinear polarization $P(\omega_{as})$:

$$P(\omega_{as}) = \left(\frac{\partial\alpha}{\partial Q}\bigg|_o\right)^2 \frac{N}{m}\frac{E_p^2 E_s^*}{\omega_v^2 - (\omega_p - \omega_s)^2 - 2i\gamma(\omega_p - \omega_s)} = 3\chi_r^{(3)}(\omega_{as})E_p^2 E_s^* \tag{3.4.33}$$

where we have defined the vibrationally resonant third-order susceptibility $\chi_r^{(3)}$:

$$\chi_r^{(3)} = \left(\frac{\partial\alpha}{\partial Q}\bigg|_o\right)^2 \frac{N}{3m}\frac{1}{\omega_v^2 - (\omega_p - \omega_s)^2 - 2i\gamma(\omega_p - \omega_s)}. \tag{3.4.34}$$

$\chi_r^{(3)}$ is an inherent property of the medium that describes the sample response to the incident optical fields. When the frequency difference of incident optical fields matches the frequency of a vibrational mode (vibrationally resonant process), it will be maximized.

Although the classical description of CARS can provide a simplified relationship with the medium, it does not take into account the possibility of virtual states and non-resonant conditions. For this aim, we have to consider the semiclassical description which incorporates the quantum mechanical character of the material into the picture, whereas the description of the field remains classical. A mathematical expression for FWM process can be obtained by using density matrix formalism [99]. This also allows the inclusion of virtual levels, short lived intermediate quantum states that mediate otherwise forbidden transitions in a multiphoton process. In the following, we will briefly introduce the main mathematical tools necessary to describe the nonlinear polarization, largely discussed in Ref [99]. Then we will focus on CARS response.

3.4.1 Density matrix

The time evolution of a quantum mechanical state is represented by its time-dependent state $|\psi(t)\rangle$, whose evolution is described by the Schrödinger equation:

$$\frac{d}{dt}|\psi(t)\rangle = -\frac{i}{\hbar}H(t)|\psi(t)\rangle \tag{3.4.35}$$

By solving this equation, it is possible to determine the eigenvalues E_n and the correspondent eigenstates $|\phi_n\rangle$, which form a complete and orthonormal basis set in Hilbert-space. Clearly, each $|\psi(t)\rangle$ can be expanded in terms of the new basis $|\phi_n\rangle$.

$$|\psi(t)\rangle = \sum_n |\phi_n\rangle\langle\phi_n||\psi(t)\rangle = \sum_n c_n(t)|\phi_n\rangle$$

We now define the density matrix $\rho(t)$ of a pure state:

$$\rho(t) = |\psi(t)\rangle\langle\psi(t)|$$

$$\rho(t) = \sum_{n,m} c_n(t)c_m^*(t)|n\rangle\langle m| = \sum_{n,m}\rho_{nm}(t)|n)\rangle\langle m| \tag{3.4.36}$$

wherein $\rho_{nm}(t) = c_n(t)c_m^*(t)$. So, the expectation value of an operator A is simply given by:

$$\langle A\rangle = \sum_{n,m} A_{nm}\rho_{nm}(t) = \mathrm{Tr}(\rho A)\ .$$

According to the Ehrenfest theorem, Liouville-Von Neumann equation expresses ρ time evolution as:

$$\frac{d\rho}{dt} = -\frac{i}{\hbar}[H,\rho]\ . \tag{3.4.37}$$

Generally, in condensed phase systems, we have to deal with statistical ensembles, rather than pure states. As there is no way to write a wavefunction of a statistical average, but the density matrix of a statistical ensemble is defines as:

$$\rho = \sum_n P_n|\phi_n\rangle\langle\phi_n|\ ,$$

where P_n be the probability of a system being in a pure state $|\phi_n\rangle$.

As the density operator for a statistical ensemble is a linear superposition of the density operator of the pure states, the equation obtained for pure states, that are

both linear in ρ, also can be applied for statistical average. The off-diagonal terms of the density matrix are called coherences, while the diagonal terms are called populations and are real, indeed the trace of the density matrix must be equal to 1 [99]. So the use of the density matrix and the Liouville-Von Neumann equation allows the study of the time-evolution of statistical average. Therefore the presence of the commutators in Eq. 3.4.37 results in field-matter interactions both from the ket and the bra side of the density operator. Hence, an initial population state is able to evolve in a generic coherence state, as will be pointed out in next sections.

3.4.2 Interaction picture

Consider a system coupled to an external field by means of the dipole moment operator μ. The overall Hamiltonian $H(t)$ is given by:

$$H(t) = H_0 + H'(t) \qquad \text{with} \qquad H'(t) \ll H_0 \ , \qquad H'(t) = \mu E(t), \tag{3.4.38}$$

where H_0 is a simpler time-independent Hamiltonian and $H'(t)$ is small time-dependent Hamiltonian, that can be treated perturbatively; this last condition allows to find the solutions of $H(t)$ starting from the solutions of H_0, using a power expansion in $H'(t)$ limited to a finite number of terms. The assumption of a time-independent H_0 and of a weak $H'(t)$ corresponds to our systems, with a strong molecular field plus a weak effective radiation-matter interaction. Actually, in this limit, the time-dependent perturbation theory is a widely used tool to describe the light-matter interaction.

The interaction scheme represents the best approach to determine the system time evolution and in this representation both wavefunctions and operators evolve in time:

$$\begin{aligned}
&|\psi_S(t)\rangle = U(t,t_0)\,|\psi_I(t)\rangle && \rightarrow \quad |\psi_I(t)\rangle = U^\dagger(t,t_0)\,|\psi_S(t)\rangle\,, \\
&A_S = U(t,t_0)\,A_I U^\dagger(t,t_0) && \rightarrow \quad A_I = U^\dagger(t,t_0)\,A_S\,U(t,t_0), \\
&\frac{d}{dt}\,|\psi_S(t)\rangle = -\frac{i}{\hbar}H_S(t)\,|\psi_S(t)\rangle && \rightarrow \quad \frac{d}{dt}\,|\psi_I(t)\rangle = -\frac{i}{\hbar}H'_I(t)\,|\psi_I(t)\rangle\,.
\end{aligned} \tag{3.4.39}$$

where $|\psi(t)\rangle$ indicates the system wavefunction, A is a generic operator and the subscripts S and I indicate the Schrödinger and interaction scheme, respectively.

$U(t,t_0)$ is the non-interacting propagator and it is a unitary operator: $U(t,t_0) = e^{-\frac{i}{\hbar}H_0(t-t_0)}$.

Note that the interaction picture can be considered as an intermediate representation between Schrödinger and Heisenberg picture. Whereas in the other two pictures either the state vector or the operators carry time dependence, in the interaction picture both carry part of the time dependence of observables.

It is now possible to integrate the Schrödinger equation in the interaction scheme between t_0 (initial time) e t:

$$|\psi_I(t)\rangle = |\psi_I(t_0)\rangle - \frac{i}{\hbar}\int_{t_0}^{t} dt_1 H'_I(t_1)\,|\psi_I(t_1)\rangle \ .$$

Now we ripete the same procedure, expaning the term $|\psi_I(t_1)\rangle$ in the integral.

$$|\psi_I(t)\rangle = |\psi_I(t_0)\rangle + \sum_{n=1}^{\infty}\left(-\frac{i}{\hbar}\right)^n \int_{t_0}^{t} dt_n \int_{t_0}^{t_n} dt_{n-1}\ldots \int_{t_0}^{t_2} dt_1 T[H'_I(t_n)H'_I(t_{n-1})\ldots H'_I(t_1)]\,|\psi_I(t_0)\rangle \ .$$

T indicates the time-ordered product defined as:

$$T[A(t_1)B(t_2)] = \begin{cases} A(t_1)B(t_2) & t_1 \le t_2 \\ B(t_2)A(t_1) & t_1 > t_2 \end{cases}$$

Then, converting the expression again in the Schrödinger scheme, we have:

$$|\psi_S(t)\rangle \equiv U(t,t_0)\,|\psi_I(t)\rangle = U(t,t_0)\,|\psi_S(t_0)\rangle + \sum_{n=1}^{\infty}\left(-\frac{i}{\hbar}\right)^n \int_{t_0}^{t} dt_n \int_{t_0}^{t_n} dt_{n-1}\ldots$$

$$\int_{t_0}^{t_2} dt_1 U(t,t_n)H'(t_n)U(t_n,t_{n-1})H'(t_{n-1})\ldots \underbrace{U(t_2,t_1)}_{\text{Free propagator}} \underbrace{H'(t_1)}_{\text{Interaction}} \underbrace{U(t_1,t_0)\,|\psi_S(t_0)\rangle}_{\text{Free propagator}} \ .$$

The physical interpretation of this equation appears clearly: the system evolves without interacting with the external field until t_1, when it interacts for the first time, then it continues to evolve imperturbed until t_2, when we have a second interaction, and so on.

We may now perform the same power expansion for the density matrix by considering the analogy between the Schrödinger equation and Liouville-Von Neumann equation:

$$\rho_I(t) = \rho_I^{(0)}(t_0) + \sum_{n=0}^{\infty}\left(-\frac{i}{\hbar}\right)\int_{t_0}^{t} dt_n \int_{t_0}^{t_n} dt_{n-1}\ldots\int_{t_0}^{t_2} dt_1 \\ [H'_I(t_n),[H'_I(t_{n-1})\ldots[H'_I(t_1),\rho(t_0)]\ldots]] \ . \tag{3.4.40}$$

Then, going back to the Schrödinger scheme we have:

$$\rho(t) = \rho^{(0)}(t) + \sum_{n=1}^{\infty} \left(-\frac{i}{\hbar}\right) \int_{t_0}^{t} dt_n \int_{t_0}^{t_n} dt_{n-1} \ldots \int_{t_0}^{t_2} dt_1$$
$$U(t,t_0) \left[U(t_n,t_0) H'(t_n) U^\dagger(t_n,t_0) \ldots \left[U(t_1,t_0) H'(t_1) U^\dagger(t_1,t_0), \rho(t_0)\right], \ldots\right] U^\dagger(t,t_0). \tag{3.4.41}$$

Note that since the density matrix contains a ket and a bra, the interaction can be either from the left or from the right. This can be seen easily by writing the commutator explicitly. Hence, once we explicitly write $H'_I(t)$, we have:

$$\rho^{(n)}(t) = \left(-\frac{i}{\hbar}\right)^n \int_{-\infty}^{t} dt_n \int_{-\infty}^{t_n} dt_{n-1} \ldots \int_{-\infty}^{t_2} dt_1 \, E(t_n) \, E(t_{n-1}) \ldots E(t_1)$$
$$U(t,t_0) \left[\mu_I(t_n), \left[\mu_I(t_{n-1}) \ldots \left[\mu_I(t_1), \rho(-\infty)\right] \ldots\right]\right] U^\dagger(t,t_0), \tag{3.4.42}$$

where $\mu_I(t) = U^\dagger(t,t_0) \mu U(t,t_0)$.

3.5 Nonlinear Polarization

As discussed previously, the polarization $P(t)$ represents the macroscopic response of the system to an external eletric field it is given by the expectation value of the dipole operator μ:

$$P(t) = \langle \mu \rangle = \mathrm{Tr}(\mu \rho(t)) \,. \tag{3.5.43}$$

When inserting Eq. 3.4.41 into Eq. 3.5.43, we obtain for the n-th order polarization:

$$P^{(n)}(t) = \left(-\frac{i}{\hbar}\right)^n \int_{-\infty}^{t} dt_n \int_{-\infty}^{t_n} dt_{n-1} \ldots \int_{-\infty}^{t_2} dt_1 \, E(t_n) \, E(t_{n-1}) \ldots E(t_1)$$
$$\left\langle \mu_I(t) \left[\mu_I(t_n) \left[\mu_I(t_{n-1}), \ldots \left[\mu_I(t_1), \rho(-\infty)\right] \ldots\right]\right]\right\rangle \,. \tag{3.5.44}$$

Frequently, a different set of time variables τ is preferred:

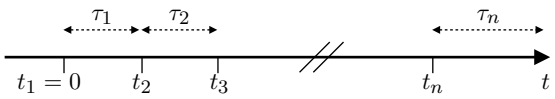

$$
\begin{aligned}
&t_1 = 0 \\
&\tau_1 = t_2 - t_1 \\
&\tau_2 = t_3 - t_2 \\
&\dots \\
&\tau_n = t - t_n
\end{aligned}
$$

The time variables t_i denote absolute time points, while the time variables τ_i indicate time intervals. By introducing this new temporal notation, we get:

$$
\begin{aligned}
&P^{(n)}(t) = \left(-\frac{i}{\hbar}\right)^n \int_0^\infty d\tau_n \int_0^\infty d\tau_{n-1} \dots \int_0^\infty d\tau_1 \\
&E(t-\tau_n)\, E(t-\tau_n-\tau_{n-1}) \dots E(t-\tau_n \cdots - \tau_1) \\
&\langle \mu_I(\tau_n + \tau_{n-1} + \dots \tau_1)\, [\mu_I(\tau_{n-1} + \dots \tau_1), [\mu_I(\tau_{n-2} + \dots \tau_1) \dots [\mu_I(0), \rho(-\infty)] \dots]] \rangle \ .
\end{aligned}
$$

Hence, the n-th order nonlinear response can be indicated as a convolution of n electric fields with the n-th order nonlinear response function $S^{(n)}$:

$$
\begin{aligned}
&P^{(n)}(t) = \int_0^\infty d\tau_n \int_0^\infty d\tau_{n-1} \dots \int_0^\infty d\tau_1 \\
&E(t-\tau_n)\, E(t-\tau_n-\tau_{n-1}) \dots E(t-\tau_n \cdots - \tau_1)\, S(\tau_n, \tau_{n-1} \dots \tau_1) \ ,
\end{aligned}
\tag{3.5.45}
$$

where $S^{(n)}$ is:

$$
\begin{aligned}
&S^{(n)}(\tau_n, \dots \tau_1) = \left(-\frac{i}{\hbar}\right)^n \\
&\langle \mu_I(\tau_n + \tau_{n-1} + \dots \tau_1)\, [\mu_I(\tau_{n-1} + \dots \tau_1), \dots [\mu_I(0), \rho(-\infty)] \dots] \rangle \ .
\end{aligned}
\tag{3.5.46}
$$

If we now write explictly the commutators, we have two terms for each of them, i.e. 2^n term. Nevetheless, we do not have to consider also the complex conjugates, that give rise to the same system response, obtaining 2^{n-1} indipendent terms only (i.e. one term at the first order, 4 at the third order). In this way, the nth-order polarizability can be written as the convolution between n electric fields and the nonlinear response function. It is worth pointing out that the last interaction

$\mu_I(\tau_n + \tau_{n-1} + \ldots \tau_1)$ has a different role in the system evolution compared to the other interactions, because it is not a part of the commutator: the interactions at times 0, τ_1, ..., $\tau_n + \tau_{n-1} + \ldots \tau_1$ generate a non-equilibrium density matrix, whose offdiagonal elements allow to emit a light field at time $\tau_n + \tau_{n-1} + \ldots \tau_1$. Since $P^{(n)}(t)$ is a physical observable, and is given by the expectation value of a Hermitian operator, it is real. The same arguments also holds for the electric field $E(t)$. Consequently, the response function $S^{(n)}$ must be real as well. Furthermore the polarization at any time can depend only on the electric field at earlier times. This comes from the principles of causality.

As already pointed in the introduction of this chapter, the approach followed to get the n-th order polarization $P^{(n)}(t)$ induced in the system is to use a semi-classical theory, which treats the sample as a quantum system, but considers the interaction with classical external fields. Mukamel et al. have introduced a quantum electrodynamical (QED) description [155] that uses the quantization of the electrical field. The advantages of QED approach arise when we are dealing with processes deeply related to the quantum nature of the electromagnetic field, such as incoherent phenomena of matter-field interaction (like fluorescence, two photon fluorescence, spontaneous Raman), interaction with vacuum (or low fluence) field or entangled states. Processes where the detected signal is obtained from the uncorrelated contributions of the individual particles are termed incoherent (and are not able to generate stationary interference). Such signals hence scale as the number of particles N in the interaction volume. In the coherent processes, on the other hand, the contributions of the constituent particles add up on the level of amplitudes rather than intensities, and the effect is proportional to N^2. Since CARS is a coherent process and we are dealing with a macroscopic sample, our semiclassical approach leads to a final result that is identical to the one obtained by QED, and makes the physics more direct.

3.5.1 Third-order interaction

As already discussed, CARS is associated to the third order optical response of the system. Therefore, we have to consider the third term of the P expansion series.

$$P^{(3)}(t) \propto \int_0^\infty d\tau_3 \int_0^\infty d\tau_2 \int_0^\infty d\tau_1 E(t-\tau_3)E(t-\tau_3-\tau_2)E(t-\tau_3-\tau_2-\tau_1)S^{(3)}(\tau_1,\tau_2,\tau_3) \ . \tag{3.5.47}$$

with:

$$S^{(3)}(\tau_1,\tau_2,\tau_3) = \langle \mu(\tau_3+\tau_2+\tau_1)\big[\mu(\tau_2+\tau_1),\big[\mu(\tau_1),\big[\mu(0),\rho(-\infty)\big]\big]\big]\rangle \ . \tag{3.5.48}$$

If we now write the commutators explicitly, we have:

$$\begin{aligned}
S^{(3)}(\tau_1,\tau_2,\tau_3) = &\langle \mu(\tau_3+\tau_2+\tau_1)\mu(\tau_2+\tau_1)\mu(\tau_1)\mu(0)\rho(-\infty)\rangle && \Longrightarrow R_4 \\
&- \langle \mu(\tau_3+\tau_2+\tau_1)\mu(\tau_2+\tau_1)\mu(\tau_1)\rho(-\infty)\mu(0)\rangle && \Longrightarrow R_1^* \\
&- \langle \mu(\tau_3+\tau_2+\tau_1)\mu(\tau_2+\tau_1)\mu(0)\rho(-\infty)\mu(\tau_1)\rangle && \Longrightarrow R_2^* \\
&+ \langle \mu(\tau_3+\tau_2+\tau_1)\mu(\tau_2+\tau_1)\rho(-\infty)\mu(0)\mu(\tau_1)\rangle && \Longrightarrow R_3 \\
&- \langle \mu(\tau_3+\tau_2+\tau_1)\mu(\tau_1)\mu(0)\rho(-\infty)\mu(\tau_2+\tau_1)\rangle && \Longrightarrow R_3^* \\
&+ \langle \mu(\tau_3+\tau_2+\tau_1)\mu(\tau_1)\rho(-\infty)\mu(0)\mu(\tau_2+\tau_1)\rangle && \Longrightarrow R_2 \\
&+ \langle \mu(\tau_3+\tau_2+\tau_1)\mu(0)\rho(-\infty)\mu(\tau_1)\mu(\tau_2+\tau_1)\rangle && \Longrightarrow R_1 \\
&- \langle \mu(\tau_3+\tau_2+\tau_1)\rho(-\infty)\mu(0)\mu(\tau_1)\mu(\tau_2+\tau_1)\rangle && \Longrightarrow R_4^*
\end{aligned}$$

The presence of the commutators in Eq. 3.5.47 generates several contributions for the density matrix, even in low order expansions; for this reason it is helpful to represent all the terms generated by the expansion of the commutators by a diagrammatic approach. Indeed, each term corresponds to a Feynman diagram (shown in Fig. 3.2, wherein we do not include the complex conjugates diagrams). Feynman diagrams are an elegant wayl to represent the different contributions to the system response and they can be read using the following rules:

- Two vertical lines represent the time evolution of the ket and bra of the ρ. Time is running from the bottom to the top.
- Interactions with light fields are represented by arrows. The last interaction derives from the trace operation $P^{(n)}(t) = \langle \mu\rho^{(n)}(t)\rangle$ and it is usually represented by a different (dashed or wavy) arrow.

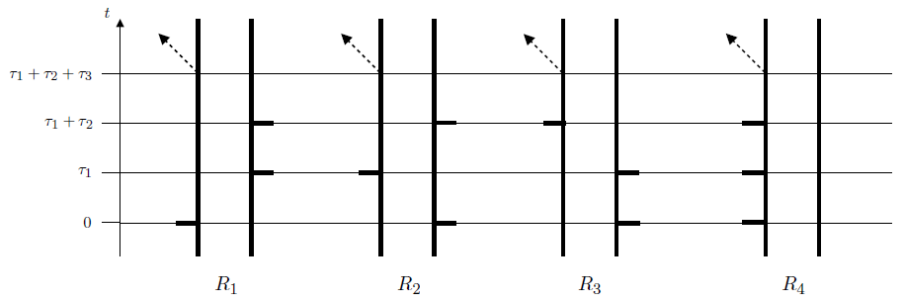

Figure 3.2: Diagrams corresponding to the third order terms of the system response.

- Each diagram has a sign $(-1)^n$, where n is the number of interactions from the right. The last interaction does not have to be considered in this rule.
- An arrow pointing to the right represents an electric field with $e^{-i\omega t+ikr}$, while an arrow pointing to the left represents an electric field with $e^{i\omega t-ikr}$. The emitted light, i.e. the last interaction, has a frequency and wavevector equal to the sum of the input frequencies and wavevectors, considering that the electric field can be written in the form: $E(t) = E_0(e^{-i\omega t+ikr} + e^{i\omega t-ikr})$.
- An arrow pointing towards the system represents an up-climbing of the corresponding side of the density matrix, while an arrow pointing away represents a de-excitation.
- The last interaction must end in a population state.

To compute the complete response, we have to take into account the electric fields. Let suppose that it is composed by three pulsed lasers:

$$E(t) = E_1(t)(e^{-i\omega t} + e^{i\omega t}) + E_2(t)(e^{-i\omega t} + e^{i\omega t}) + E_3(t)(e^{-i\omega t} + e^{i\omega t}) \ , \qquad (3.5.49)$$

Then, Eq. 3.5.47 includes 864 different terms (we have already excluded the complex conjugates). Each of them will correspond to part of the system response, i.e to a Feynman diagram. Nevertheless, there are some considerations that can be taken into account to reduce the number of significant terms.

- **Time-ordering**: when the laser pulses are shorter than the time separation between them, they do not overlap in time so we have strict time ordering.

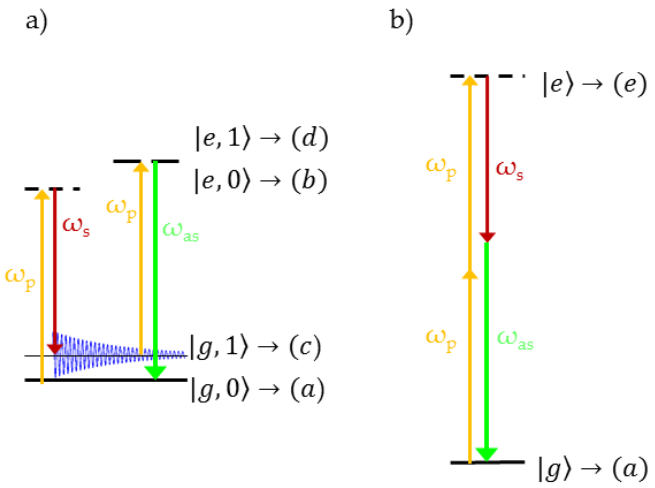

Figure 3.3: Ladder energy diagram for CARS (a) and NVRB (b) processes.

- **Rotating wave approximation**: it consists in supposing that the electric field frequency is much higher than the Rabi frequency [145]. Then, only terms containing either $e^{-i\omega t}$ or $e^{i\omega t}$ will contribute to the response, but not both. The number of terms becomes 4.

- **Phase-matching**: as we have already seen, the wavevector of P is $k = \pm k_1 \pm k_2 \pm k_3$. Then, we can be experimentally interested to a specific measurements direction. However, given the validity of the rotating wave approximation, only one set of signs will survive, which allows further reducing of the number of terms.

3.6 Diagrammatic approach in CARS

Fig. 3.3.a shows the ladder energy diagram for CARS, considering the degenerate case: $\omega_1 = \omega_3 = \omega_p$ and $\omega_2 = \omega_s$. The ladder energy representation is analougous to the Feynman diagram, already explained. Horizontal lines represent the system energy level; if these lines are dashed we are referring to a virtual state. Electric field interactions are indicated by an arrow, which is solid if the field acts on the bra side of the density matrix, dashed otherwise. Time runs from the left to the right. In Fig. 3.3.a, a and c denote the vibrational ground state, $|g,0\rangle$, and the first

vibrational excited level, $|g,1\rangle$, with respect to the electronic ground state $|g\rangle$. b and d indicate the vibrational ground state, $|e,0\rangle$, and the first vibrational excited level, $|e,1\rangle$, with respect to the excited electronic state $|e\rangle$. Actually, the diagram in Fig. 3.3.a is not the only one possible, involving the considered incoming fields. Indeed we should take into account those FWM mechanisms, that utilize the same input frequency components but are no more in resonance with the vibrational states of the system as shown in Fig. 3.3.b. We call this contribution to the system response Non-Vibrationally Resonant Background (NVRB). This additional term has to be considered in the response calculation, as it will interfere with the CARS diagram, significantly affecting the overall response.

Considering SP at $\Delta t_S = 0$ with relative delay with PP $\Delta t = \Delta t_P$, their electric fields can be written as [145]: $E_P(t,\Delta T) = A_P(t,\Delta T)e^{-i\omega_P t}$ and $E_S(t,0) = A_S(t,0)e^{-i\omega_S t}$, where $A_{P/S}(t,\Delta T)$ indicates the PP/SP temporal envelope. Energy level diagrams in Fig. 3.3 show the processes that generate CARS and NVRB, that can be computed [99]:

$$\begin{aligned} &P^{(3)}_{CARS}(t) \propto (i)^3 \mu_{ba}\mu_{cb}\mu_{cd}\mu_{ad} \int_0^\infty d\tau_3 \int_0^\infty d\tau_2 \int_0^\infty d\tau_1 \\ &A_P(t-\tau_1-\tau_2-\tau_3,\Delta t)A_S^*(t-\tau_2-\tau_3)A_P(t-\tau_3,\Delta t) \\ &e^{-i\omega_P(t-\tau_1-\tau_2-\tau_3,\Delta t)}e^{+i\omega_S(t-\tau_2-\tau_3)}e^{-i\omega_P(t-\tau_3,\Delta t)}e^{-i\bar{\omega}_{ba}\tau_1}e^{-i\bar{\omega}_{ca}\tau_2}e^{-i\bar{\omega}_{da}\tau_3} \end{aligned} \tag{3.6.50}$$

$$\begin{aligned} &P^{(3)}_{NVRB}(t) \propto (i)^3 |\mu_{ea}|^4 \int_0^\infty d\tau_3 \int_0^\infty d\tau_2 \int_0^\infty d\tau_1 \\ &A_P(t-\tau_1-\tau_2-\tau_3)A_P(t-\tau_2-\tau_3)A_S^*(t-\tau_3) \\ &e^{-i\omega_P(t-\tau_1-\tau_2-\tau_3,\Delta t)}e^{-i\omega_P(t-\tau_2-\tau_3,\Delta t)}e^{+i\omega_S(t-\tau_3)}e^{-i\bar{\omega}_{ea}\tau_1}e^{-i\bar{\omega}_{ea}\tau_2}e^{-i\bar{\omega}_{ea}\tau_3} \end{aligned} \tag{3.6.51}$$

where $\bar{\omega}_{ij} = \omega_i - \omega_j - i\gamma_{ij}$, $\gamma_{ij} = \tau_{ij}^{-1}$ is the dephasing rate of the $|i\rangle\langle j|$ coherence and μ_{ij} is the transition dipole moment between i and j states. The ω_{ca} level in Eq.3.6.50 is the frequency of the Raman mode coherently stimulated in the CARS process, while ω_{ba} and ω_{da} are frequency differences between the involved electronic levels. ω_e is the energy of the electronic excited level involved in the NVRB scattering process.

By Fourier transforming, the fields can be expressed in the frequency domain as: $\hat{E}_P(\omega,\Delta T) = \int_{-\infty}^{+\infty} E_P(t,\Delta T)e^{i\omega t}dt$ and $\hat{E}_S(\omega,0) = \int_{-\infty}^{+\infty} E_S(t,0)e^{i\omega t}dt$; the fre-

quency dispersed signal corresponds to :

$$P^{(3)}_{CARS}(\omega) \propto \eta_{\mathrm{CARS}}\,(i)^3 \int_{-\infty}^{\infty} dt\, e^{i\omega t} \int_0^{\infty} d\tau_3 \int_0^{\infty} d\tau_2 \int_0^{\infty} d\tau_1 \int_{-\infty}^{\infty} d\omega_1 \int_{-\infty}^{\infty} d\omega_2 \int_{-\infty}^{\infty} d\omega_3$$
$$\hat{A}_P(\omega_1,\Delta t)\hat{A}^*_S(\omega_2,0)\hat{A}_P(\omega_3,\Delta t) e^{-i(\omega_P+\omega_1)(t-\tau_1-\tau_2-\tau_3)} e^{+i(\omega_S+\omega_2)(t-\tau_2-\tau_3)}$$
$$e^{-i(\omega_P+\omega_3)(t-\tau_3)} e^{-i\bar{\omega}_{ba}\tau_1} e^{-i\bar{\omega}_{ca}\tau_2} e^{-i\bar{\omega}_{da}\tau_3} \tag{3.6.52}$$

where $\eta_{\mathrm{CARS}} = \mu_{ba}\mu_{cb}\mu_{cd}\mu_{ad}$. In this way all the temporal integrals can be solved analytically by using the energy conservation, represented by the delta distribution:

$$\delta(\omega - 2\omega_P + \omega_S - \omega_1 + \omega_2 - \omega_3) = \int_{-\infty}^{\infty} dt\, e^{i(\omega-2\omega_P+\omega_S-\omega_1+\omega_2-\omega_3)t}, \tag{3.6.53}$$

Then we have:

$$P^{(3)}_{CARS}(\omega) \propto -\eta_{\mathrm{CARS}} \int_{-\infty}^{\infty} d\omega_1 \int_{-\infty}^{\infty} d\omega_2 \int_{-\infty}^{\infty} d\omega_3 \delta(\omega - 2\omega_P + \omega_S + \omega_1 - \omega_2 + \omega_3)$$
$$\frac{\hat{A}_P(\omega_1,\Delta t)\hat{A}^*_S(\omega_2,0)\hat{A}_P(\omega_3,\Delta t)}{(\omega_P + \omega_1 - \bar{\omega}_{ba})(\omega_P - \omega_S + \omega_1 - \omega_2 - \bar{\omega}_{ca})(2\omega_P - \omega_S + \omega_1 - \omega_2 + \omega_3 - \bar{\omega}_{da})} \tag{3.6.54}$$

The ω_2 integral can be simplified:

$$P^{(3)}_{CARS}(\omega,\Delta t) \propto -\eta_{\mathrm{CARS}} \int_{-\infty}^{\infty} d\omega_1 \int_{-\infty}^{\infty} d\omega_3$$
$$\frac{\hat{A}_P(\omega_3,\Delta t)\hat{A}_P(\omega_1,\Delta t)\hat{A}^*_S(2\omega_P - \omega_S - \omega + \omega_3 + \omega_1, 0)}{(\omega_P + \omega_3 - \bar{\omega}_{ba})\,(\omega - \omega_P - \omega_1 - \bar{\omega}_{ca})\,(\omega - \bar{\omega}_{da})} \tag{3.6.55}$$

Note that in the case of real levels resonance enhancement occurs [99]. In a similar way, using $\eta_{\mathrm{NVRB}} = |\mu_{ea}|^4$, Eq.3.6.51 can be written as:

$$P^{(3)}_{NVRB}(\omega,\Delta t) \propto -\eta_{\mathrm{NVRB}} \int_{-\infty}^{\infty} d\omega_1 \int_{-\infty}^{\infty} d\omega_2$$
$$\frac{\hat{A}_P(\omega_1,\Delta t)\hat{A}_P(\omega_2,\Delta t)\hat{A}^*_S(2\omega_P - \omega_S - \omega + \omega_1 + \omega_2, 0)}{(\omega_P + \omega_1 - \bar{\omega}_{ea})\,(2\omega_P + \omega_1 + \omega_2 - \bar{\omega}_{ea})\,(\omega - \bar{\omega}_{ea})} \tag{3.6.56}$$

The homodyne anti-Stokes signal, $I(\omega_{as})$, generated by CARS and NVRB, originates from the electric field emitted by the overall third order polarization, $P^{(3)}$, detected as [146]:

$$I(\omega_{as}) \propto |P^{(3)}_{CARS}(\omega_{as}) + P^{(3)}_{NVRB}(\omega_{as})|^2. \tag{3.6.57}$$

Critically, for general PP and SP spectral profiles, these integrals have not an analytic expression and they have to be evaluated numerically. However, we can extract

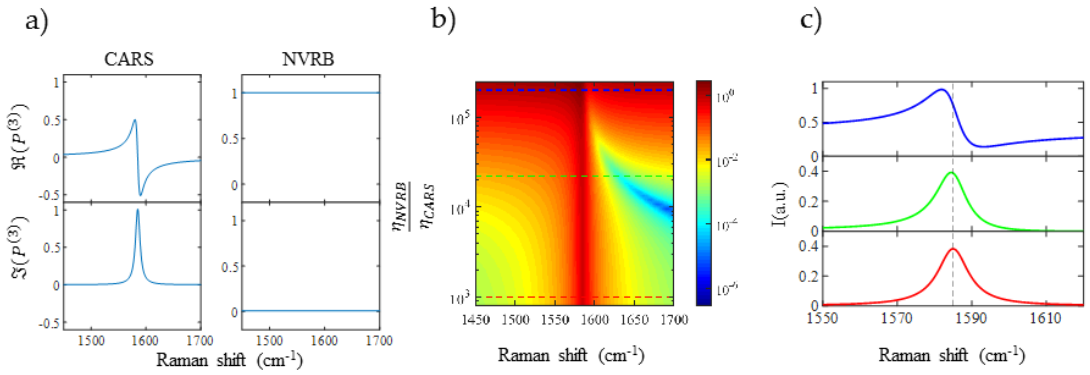

Figure 3.4: CARS and NVRB spectral shapes derived from Eqs. 3.6.58,3.6.59 in the electronically non-resonant case, considering $\omega_{ca} = POS(G) = 1590$ cm^{-1} [12], $\tau_{ba} = \tau_{da} = \tau_{ea} = 10$fs [86], $\gamma_{ca} = \Gamma_G/2 = 6$cm^{-1} [44](where $\Gamma_G = FWHM(G)$). In panel (a) normalized $\Re(P^{(3)}_{CARS})$, $\Im(P^{(3)}_{CARS})$ and $\Re(P^{(3)}_{NVRB})$, $\Im(P^{(3)}_{NVRB})$. Colormaps indicate I^{NR}_{as} for different ratios $\eta_{\text{NVRB}}/\eta_{\text{CARS}}$. In panels (c), selected profiles corresponding to three ratios from the colormap are reported: $\eta_{\text{NVRB}}/\eta_{\text{CARS}} = 0.1, 3, 20$ represented in red, green and blu respectively.

some physical insigth in the peculiarities of the CARS response, by firstly considering monocromatic fields with no inter-pulse delay: $\hat{E}_P(\omega) = E_P \cdot \delta(\omega - \omega_P)$, $\hat{E}_S(\omega) = E_S \cdot \delta(\omega - \omega_S)$. From Eqs.3.6.55 and 3.6.56, the nonlinear polarization of CARS and NVRB can be expressed as [99]:

$$P^{(3)}_{CARS}(\omega) \propto -\frac{\eta_{CARS} E_P^2 E_S^*}{(\omega_P - \bar{\omega}_{ba})(\omega - \omega_P - \bar{\omega}_{ca})(\omega - \bar{\omega}_{da})} = \\ = \chi^{(3)}_{CARS} E_P^2 E_S^* \tag{3.6.58}$$

$$P^{(3)}_{NVRB}(\omega) \propto -\frac{\eta_{NVRB} E_P^2 E_S^*}{(\omega_P - \bar{\omega}_{ea})(2\omega_P - \bar{\omega}_{ea})(\omega - \bar{\omega}_{ea})} = \\ = \chi^{(3)}_{NVRB} E_P^2 E_S^* \tag{3.6.59}$$

which can be used to calculate the total FWM spectrum according to Eq.3.6.57. Fig.3.4.a shows the real and imaginary par of both $P^{(3)}_{CARS}$ and $P^{(3)}_{NVRB}$. While the latter is a real constant function as we are now considering the non-electronically resonant case, $P^{(3)}_{CARS}$ presents both real and imaginary part. $\mathcal{R}e(P^{(3)}_{CARS})$ has a dispersive shape and it is related to the electronic contribution, while $\mathcal{I}m(P^{(3)}_{CARS})$ represents the resonance Raman response and it involves nuclear contribution: it

mirrors the spontaneous Raman line and has a Lorentzian shape. As shown in Eq. 3.6.57, I_{as} is proportional to $|\chi^{(3)}|^2$:

$$\begin{aligned} I_{as}^{NR} \propto |\chi^{(3)}|^2 = |\Re e\left(\chi_R^{(3)}\right) + i\Im m\left(\chi_R^{(3)}\right)|^2 + \chi_{NVRB}^{(3)}|^2 = \\ = |\chi_R^{(3)}|^2 + |\chi_{NVRB}^{(3)}|^2 + 2\Re e\left(\chi_R^{(3)}\right)\chi_{NVRB}^{(3)} \end{aligned} \tag{3.6.60}$$

Thus, the overall signal is given by the sum of three terms. The resonant term relies on vibrational resonances and contains the qualitative and chemically specific information about the sample. The second contribution, a purely nonresonant term, depends solely upon the electronic properties of the material. Furthermore, the resonant and non-resonant responses interfere with each other and this effect prohibits direct access to the quantitative information contained in $\chi_R^{(3)}$, generating a dispersive lineshape.

In Fig. 3.4.b, overall $|\chi^{(3)}|^2$ is plotted for different values of $\eta_{\mathrm{NVRB}}/\eta_{\mathrm{CARS}}$; these graphs highlight some important consequences of having a non-resonant background. First of all, as the ratio $\chi_R^{(3)}/\chi_{NVR}^{(3)}$ decreases (see Fig. 3.4.c), the addition of the three terms creates a redshift of the maximum of the CARS spectral peak. Moreover, it causes a negative dip at the blue end, leading to a dispersive lineshape highly different from the Lorentzian spectral profile, found in spontaneous Raman. This effect precludes an immediate quantitative interpretation of the spectrum and in congested regions spectral interference between multiple resonances could lead to nearly uninterpretable CARS spectra. Secondly, the nonresonant contribution introduces an offset which adds a background to the CARS image.

For $P_{NVRB}^{(3)}$ comparable to $P_{CARS}^{(3)}$, NVRB and CARS contributions have the same order of magnitude. Hence, this produces an intense NVRB and reduces the vibrational contrast, hampering imaging of non electronically resonant samples [144].

As NVRB derives not only from the sample but may also be emitted by the cuvette or cover-slip, on which it is mounted, it often overwhelms the resonant signal, reducing chemical sensitivity in CARS experiments. Indeed, contrast in microscopy depends on the possibility of discriminating the signal from the sample with respect to other contributions. The intensity of the resonant ratio, which provides chemical selectivity to CARS, is directly related to the oscillator strength and the number density of vibrational modes. In many cases, the purely resonant

contribution is detected on a strong nonresonant background signal. Consequently, laser-induced fluctuations or changes in alignment could limit the detectability of the small resonant contribution on top of the large and noisy nonresonant background.

Therefore, a brief description of the several methods developed to reduce or suppress the nonresonant contribution to the signal is reported in Appendix A [144].

3.7 SLG third-order nonlinear response

Since graphene appeared on the stage in early 2000s, its nonlinear optical properties have been widely explored, claiming the existence of "giant" nonlinearity [156–158]. In bulk materials the third-order nonlinearity is characterized by the third-order susceptibility $\chi^{(3)}$, which relates the polarization per unit volume P to the third power of the electric-field $\mathcal{E}$. In a two-dimensional conducting material like graphene it is more appropriate to describe the nonlinear response in terms of the sheet current $j^{(3)}$:

$$j^{(3)}(\omega_e) = \sigma^{(3)} E_1(\omega_1) E_2(\omega_2) E_3(\omega_3) \tag{3.7.61}$$

By solving the Liouville-Von Neumann equation for the density matrix [56], it can be derived that the third-order surface dynamical conductivity $\sigma^{(3)}$ is equal to $\frac{e^2}{\hbar}\left(\frac{eV}{\hbar\omega^2}\right)^2$. It is given by the product of the linear high-frequency interband conductivity $e^2/\hbar$ and the square of the electric-field parameter $\mathcal{F}_q$ divided for the electric field E, where $\mathcal{F}_q \sim eEV/\hbar\omega^2$ is the work done by the electric field during one oscillation period, eEV/ω, divided by the characteristic quantum energy $\hbar\omega$ [157].

Let us introduce the effective nonlinear susceptibility of graphene $\chi^{(3)}_{gr} \simeq \sigma^{(3)}/\omega d_{gr}$, where d_{gr} is the effective thickness of a graphene layer. Assuming that the typical nonlinear susceptibility of bulk insulator is $\chi^{(3)}_{bulk} \simeq a_B^4/e^2$ (a_B is the Bohr radius), we find:

$$\frac{\chi^{(3)}_{gr}}{\chi^{(3)}_{bulk}} \simeq \frac{\lambda^5}{a_B^4 d_{gr}} \left(\frac{e^2}{\hbar c}\right) \frac{V^2}{c^2} \tag{3.7.62}$$

Supposing that $\lambda \simeq 1\mu m$ and $a_B \simeq d_{gr} \simeq 1\mathring{A}$, we obtain

$$\chi^{(3)}_{gr} \simeq \chi^{(3)}_{bulk} \times 10^8 \tag{3.7.63}$$

By considering that insulating materials typically exhibit $|\chi^{(3)}_{bulk}| \simeq 10^{-15}$ esu, in graphene it is expected that $|\chi^{(3)}_{gr}| \simeq 10^{-8}$ esu [157].

Nonlinearity in graphene can be associated to both interband and, if doped, intraband optical transitions. In the first case, as the nonlinearity scales linearly with the number of graphene layers [159], we can conclude that it does not depend on Dirac-like dispersion of electrons, as it no longer exists in bilayer graphene. Nevertheless, it is really enhanced due to resonance at any electric field frequency, although it is limited by absorption effects. On the contrary, interband nonlinearity is caused by the electronic band dispersion: in fact electrons near the Dirac point are extremely nonlinear, though they are too few to provide meaningful nonlinear effects [156]. Unique optical and electronic properties, such as ultrawideband tunability and ultrafast saturable absorption, have contributed to the rise of graphene in photonics and optoelectronics, demonstrating its possible uses, from solar cells and light-emitting devices to touch screens, photodetectors and ultrafast lasers [3]. In particular, recent works [158, 160, 161] have highlited an electrically and broadband tunable third-order nonlinear susceptibility. By taking into account the graphene gapless dispersion and the Pauli blocking effect on the nonlinear conductivity, it has been experimentally proved and theoretically described an increase of THG signal by almost two order of magnitude by controlling the Fermi energy and the incident photon energy.

Furthermore, Ref. [140] reported the presence of a dip in the third order nonlinear FWM spectral response of SLG at the G phonon frequency. This lineshape at the Antistokes frequency was addressed to the interference between a continuum of electronic contributions and a discrete phonon state. Such description was phenomenologically interpreted in terms of Fano lineshape [141]:

$$I_{as}(\omega) \propto \frac{(\omega - \omega_G + \Gamma q)^2}{(\omega - \omega_G)^2 + \Gamma^2} \tag{3.7.64}$$

wherein ω_G is the G-phonon frequency, Γ is the phonon state broadening and q is a dimensionless parameter which gives the weight between the electronic continuum and the discrete phonon state. If $|q| \gg 1$ the discrete phonon state dominates and there is a peak lineshape (see Fig.3.5), otherwise the dominant electronic contribution gives rise to a dip, as in SLG case. As shown in Fig.3.5, depending on q value,

it is possible to find a dip, a dispersive lineshape or a peak. Notably, the authors

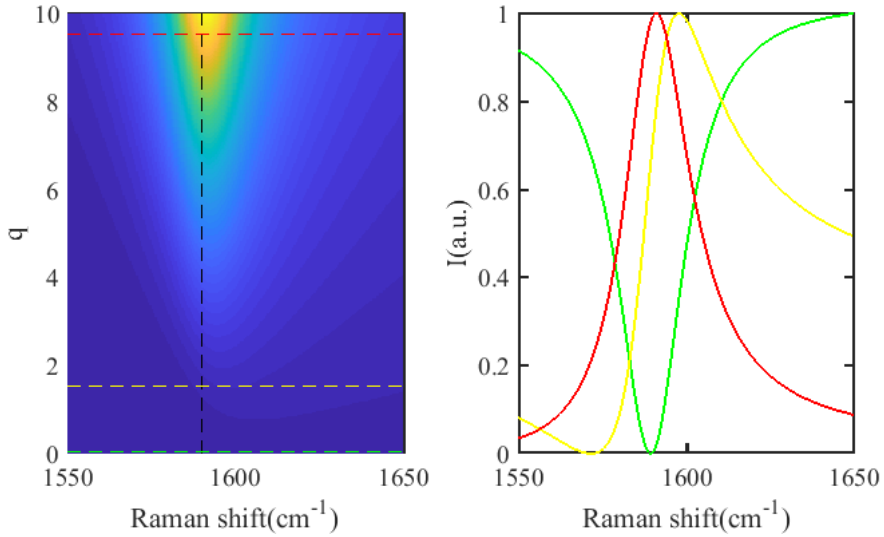

Figure 3.5: Colormap (left) plots Eq.3.7.64 as a function of q parameter and Raman shift $\omega - \omega_G$. The dashed vertical line indicates the SLG G-frequency at $\omega_G = 1590$ cm^{-1}. The horizonal lines correspond to particular q values, whose corresponding spectra are reported in the right panel. In Eq.3.7.64, we assume $\Gamma = 12$ cm^{-1} [44].

claim that in SLG the electronic contribution is expected to play a major role due to the absence of optical gap [140] as no CARS peak is observed.

3.8 Experimental methods

3.8.1 Development of CARS microscopy

The first CARS microscope was reported by the Reintjes group at the Naval Research Laboratory in 1982 [162]. Using two picosecond dye lasers with a noncollinear beam geometry, they detected the signal in the phase-matching direction with a two-dimensional detector. Nevertheless, the noncollinear beam geometry, adopted in their work, limited the image quality and the excitation with visible wavelengths resulted in a large NVRB.

Then, it was realised that when the excitation wavelengths were moved further from electronic transition, non-resonant background was reduced and unwanted

Rayleigh scattering was also minimized. Hence, by preferring near-infrared laser beams, in 1999 Zumbusch et al. [154] built a CARS microscope with collinear geometry: they chose a tight focusing condition, by using a lens with high numerical aperture. Actually, by reducing the focus volume, they noticed an efficient background signal rejection, reduction of photodamage to the sample and the possibility of studying the sample through a three-dimensional microscopy by sectioning at different focal planes. The reason for using a collinear beam geometry is that CARS needs to fulfill the phase-matching condition $\Delta\mathbf{k}l \ll \pi$, where l is the interaction length, while $\Delta\mathbf{k} = \mathbf{k}_{as} - (2\mathbf{k}_p - \mathbf{k}_s)$ is the wav-vector mismatch. In a collinear geometry with forward detection, the wavevector mismatch can be expressed as:

$$\Delta k = \frac{[n_{as}\omega_{as} - (2n_p\omega_p - n_s\omega_s)]}{c} \tag{3.8.65}$$

where n_j and ω_j $(j = p, s, as)$ are the refractive index and the frequency for the three different beams, respectively. Choosing an high numerical aperture objective produces a larger cone angle of the wavevectors of the excitation beams. Then, the nonlinearity of the interaction satisfies more easily the condition $\Delta k = 0$, revealing a better spatial resolution and image quality [163].

Since 1999, CARS microscopy has been developing, bringing about a rapid growth of literature in this scientific area. In the following, we sum up the mainl advantages of this technique [164] [165]:

- CARS microscopy provides a contrast mechanism based on molecular vibrations, that is intrinsic to the sample, circumventing the need for artificial labels, that could cause toxicity, artifacts and photobleaching.

- CARS microscopy is orders of magnitude more sensitive than spontaneous Raman microscopy. Therefore, it permits fast video-rate vibrational imaging at moderate average excitation powers.

- The nonlinearity of CARS process means that the signal is only generated at the focal volume where the laser intensities are more intense, promising a 3D sectioning capability.

- The anti-Stokes signal is blueshifted from the two excitation frequencies and it can thus be easily detected even in the presence of one-photon fluorescence background.

- By using the near-infrared excitation wavelengths, CARS microscopy has a large penetration depth (more than 0.3 mm) into the sample, allowing imaging through thick samples.

- Under typical conditions, photodamage effects are reduced thanks to low linear and nonlinear absorption of the two excitation beams.

3.8.2 Generation of pulses

As we have already extensively explained in the previous section, coherent Raman scattering requires the use of at least two synchronized sources, PP and SP, whose wavelengths could be tuned in order to match their frequency difference $\omega_P - \omega_s$ with a particular vibrational mode of the sample. The intrinsic nonlinearity of the process and its dependence on third-order susceptibility ($\chi^{(3)}/\chi^{(1)} \sim 10^{-10} - 10^{-12}$) justify the choice of ultrashort pulses: they allow the concentration of high peak intensities in a short temporal window, enhancing the the cross section of the nonlinear process [135].

Let us consider the realisation of an experimental setup for CRS with the intent to achieve both spectroscopic and microscopic information. The ideal excitation wavelength results from a compromise between optical resolution, penetration depth and sample damage threshold. As the resolution increases towards shorter wavelengths, typically the optimal wavelength range for both PP and SP is $780 - 1300$ nm, in order to access vibrational frequencies of the principal chemical functional groups , covering the 200-3600 cm^{-1} spectral range. Moreover, these wavelengths provides high penetration depth due to reduced scattering and allows for deeper CRS imaging inside the sample.

CARS sources employing pump beams, whose wavelengths are much shorter than 800 nm, can generate a large amount of multiphoton absorption, as TPA (Two-Photon Absorption), that could damage the sample owing to ultraviolet electronic

resonances. On the contrary, the upper limit depends on the sample; for example, most of biological samples are composed by water ($\sim 80 - 90\%$), that is marked by an absorption band above 1300 nm. So, it is alwayes better to work below this value [165].

Another fundamental issue is the spectral resolution. Vibrational linewidths are typically about $10-20\,\mathrm{cm}^{-1}$, which correspond to the bandwidth of a 1 ps-long transform limited Gaussian pulse. Both vibrationally resonant and non-resonant signals increase quadratically with the pulse spectral width $\Delta\omega$, but resonant contribution gradually saturates when $\Delta\omega$ approches Raman-line bandwidth; indeed only a small part of its spectral component is in resonance with the vibrational transition. Most of the frequency components will generate non-resonant background that, mixing up with the resonant signal, could not be easily substracted from the image. A good compromise between signal strength and spectral resolution is to use nearly 2 - 7 ps pulses for both pump and Stokes pulses [166].

Damaging can become an issue in nanostructures and biological samples. Coherent Raman intensity scales with the intensities of PP and SP; therefore it is necessary to balance high intensities with sample damage threshold. Using picosecond pulses, the optimal pulse energy for most samples ranges between 0.1-1 nJ. In addition, high pulse repetition rate (50-100 MHz) is necessary for high acquisition speed in imaging mode.

Coherent Raman scattering techniques require narrowband laser pulses, that can be easily tuned in wavelength. Compared with femtosecond pulses, whose sources are becoming more compact and reliable thanks to nonlinear effects [167], the generation of tunable synchronized picosecond pulses is technically more complex: for this reason several methods have been proposed to obtain narrowband picosecond pulses from broadband femtosecond ones. Many papers have been focused on working with a “spectral compressor”, based on linear approch, as spectral filtering using a narrow bandpass filter, but they are inefficient as the loss of energy is approximately proportional to the spectral narrowing.

It has been recently demonstrated a simple and powerful method for generating picosecond pulses, through the second harmonic (SH) generation process involving

a femtosecond pulse in presence of strong group velocity mismatch [168]. The full width at half maximum bandwidth of SH can be written as [151]:

$$\Delta\nu_{SHG} = \frac{0.886}{\left|\frac{1}{v_g[FF]} - \frac{1}{v_g[SH]}\right| L} = \frac{0.886}{|\delta|\, L} \tag{3.8.66}$$

In order to achieve large compression ratio, a long crystal (L) and high group velocity mismatch δ are required.

Note that second harmonic generation (SHG), and more generally Sum Frequency Generation (SFG), shows a significant dependence of the signal on phase-matching condition [145]:

$$I_3 \propto \chi^{(2)} I_1 I_2 L^2 sinc^2\left(\frac{L}{L_c}\right) \tag{3.8.67}$$

where $L_c = \Delta k/2$ is the coherence length Equation 3.8.67 explains that the maximum efficiency in emission is obtained when L is an integer multiple of L_c.

For this purpose, quasi-phase-matching techniques introduce a periodic change of $\chi^{(3)}$ phase in the crystal which causes the constructive interference of the signal emitted from these different regions [169]. A number of different approches have been proposed for the fabrication of quasi-phase matched structures: one of them is the Periodically poled Lithium Niobate (PPLN). It is a device composed of lithium niobate crystal, where the orientation of the optic axis is periodically alternated as a function of position within the material. If the period Λ of alternation of the cristalline axis is an integer multiple of L_c, each time the field intensity I_3 is about to begin to decrease as a consequence of the wavevector mismatch, a reversal of the sign of $\chi^{(3)}$ occurs, producing a monotonic growth of the signal. Therefore, periodically poled crystals allow efficient frequency conversion even with low powers and they also show high group velocity mismatch and absence of spatial walk-off. This aspect justifies the wide use of PPLN in generating picosecond pulses.

3.8.3 The fiber-laser source

The experimental setup exhibits a single fiber oscillator (see Fig. 3.6). The laser source is a commercial 40 MHz Er-doped fiber oscillator with two fiber amplified

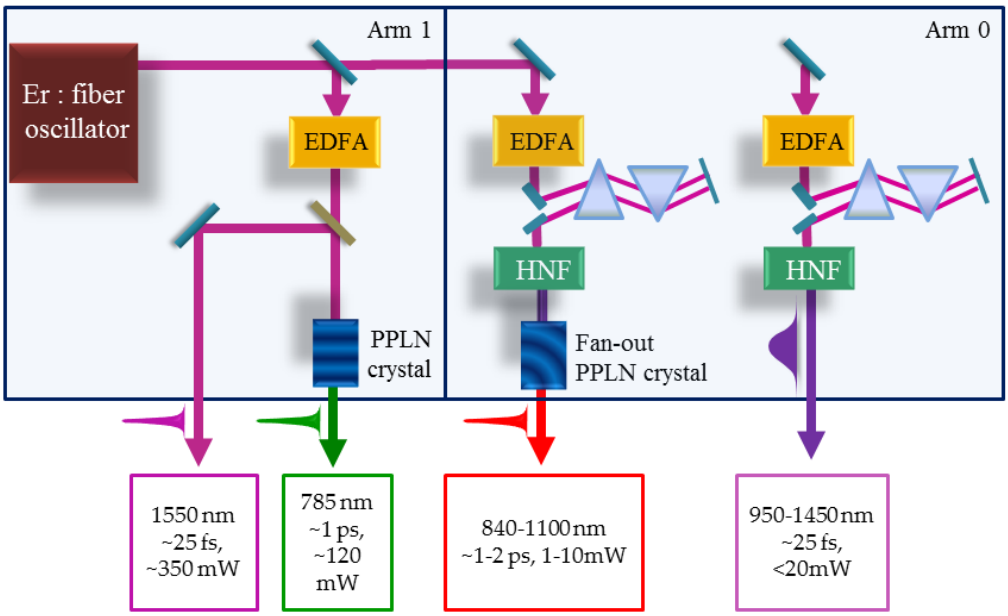

Figure 3.6: Scheme of the fiber laser source. EDFA, Erbium-Doped fiber amplified; HNF, high nonlinear fiber for SC generation; PPLN, Periodically poled Lithium Niobate.

branches (Toptica, FemtoFiber pro TNIR and FemtoFiber pro NIR), each one delivering nearly 25 fs long pulses at 1550 nm with 2.5 nJ energy and 250 mW average power. Pulses are amplified in both branches through Erbium-doped fiber amplifiers (EDFAs). Since the pulses originate from the same seed source, they are synchronized and phase-coherent.

Narrowband pulses are generated through a PPLN: the 1550 nm output of the EDFA is frequency doubled and compressed. This process explains the emission of the narrowband ($\sim 15\,\mathrm{cm}^{-1}$) pump pulse at the fixed wavelength ($\lambda = 784\,nm$) and 120 mW average power.

In the other laser arm, the amplified output, that has passed through the EDFA, is directed toward an highly nonlinear fiber (HNLF), where it undergoes spectral broadening. The supercontinuum (SC) develops spectral components on both sides of the fundamental wavelength: the overall dispersion of the input pulse can be controlled by acting on the Si prism pair, changing its position. The longest wavelengths correspond to a soliton, that can be tuned between 1700 nm and 2100 nm; it pro-

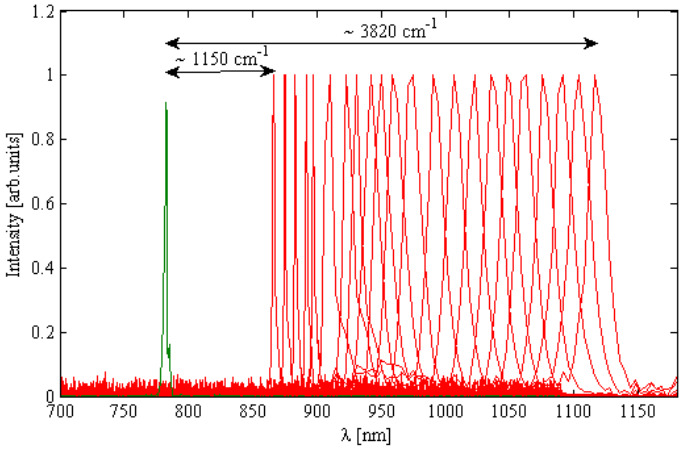

Figure 3.7: Spectra of PP (green) and tunable narrowband SP (red).

ceeds to a fan-out grating spanning PPLN, whose period of alternation of the axis inside the crystal change in a particular spatial direction. It means that, translating the crystal, phase-matching condition can be satisfied for different wavelengths: thus narrowband Stokes pulses can be continuously tuned in the range between 840 and 1100 nm.

Dispersive waves correspond to shorter wavelengths of the SC: this enables the emission of broadband Stokes pulses in the range of 950 - 1450 nm, that can be easily reduced closing two slits, situated close to the prism compressors. In fact these slits can cut spectral components that are spatially dispersed by the prism pair, rectifying the spectrum of the pulse.

3.9 Experimental setup

The experimental setup developed for narrowband CARS microscopy is shown in fig. 3.8. The power of both tunable narrowband SP and PP, generated from the laser source shown in Fig.3.6, are controlled by using neutral density filters. A telescope on the pump arm is adjusted to control its divergence and match the focal planes of the two pulses. Then they are overlapped in time by a computer-controlled delay line and combined by a 785 nm longpass filter (Semrock BLP01-785R-25). Collinearly introduced into the home-built microscope, the beams are focused on the sample

by the long working distance objective (Zeiss LD Plan-Neofluar 20x/0.4 Corr M27 ∞/0-1.5).

The long working distance, which is the distance between the closest structural element of the objective and the focal plane, is essential since the sample is usually on a cover-slip glass plate or in a cuvette.

Image scanning is performed by moving the sample with motorized X (Thorlabs ZST225B, Step motor TST 101) and Y (Mercury PI M-111.1DG) translation stages, having a travel distance of 25 mm in both X and Y directions with a one-step resolution up to $5\,\mu m$. Translation stages are controlled by the computer for acquiring microscope images. The focus condition on the sample is determined by its Z-position, which can be manually changed using a single-axis translator.

As this experimental setup is also designed to perform image scanning of 2D samples, like graphene, a careful control of the focusing condition and the damaging effects is required: at this aim, by introducing a 50:50 beamsplitter and a CMOS camera after the combiner, it is possible to collect light backreflected by the sample, obtaining easily its image in transmission.

The generated signal is collected and collimated in the forward direction by a second objective (Mitutoyo Plan Apo NIR Infinity-Corrected Objective 10X/0.26).

As recording a full narrowband CARS spectrum requires the tuning of ω_s point by point and the Stokes power is not constant as a function of the wavelength, CARS intensity has to be normalized with the Stokes power that is measured, collecting the Stokes beam by introducing a 805 nm shortpass dichroic mirror (Thorlabs DMSP805) after the condenser.

CARS signal is generated at the anti-Stokes wavelength, thus can be simply filtered out by blocking pump and Stokes beams before the detection by introducing a 750 nm hard-coated longpass filter (Thorlabs FELH0750). Then, the spectrum of the filtered CARS signal is focused on the spectrometer.

Experimental resolution

All optical microscopes are limited in the resolution that they can achieve. The concept of image formulation was deeply analysed by Ernst Abbe [170], who described

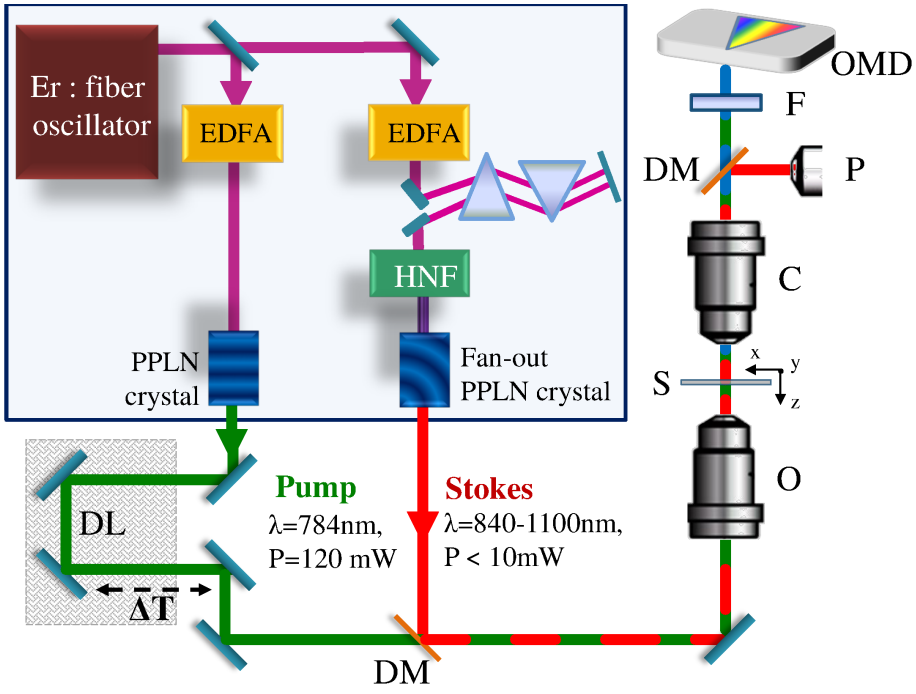

Figure 3.8: CARS setup. EDFA, Erbium-Doped fiber amplified; HNL, high non linear fiber for SC generation; DL, delay line; DM, dichroic mirror; O, objective; S, sample; C, condenser; P, powermeter; F, filter; OMD, optical multichannel analyzer. Purple, green and red lines represent the beam pathway of 1550nm, 784 nm (PP) and tunable SP.

the sample as complex gratings with details and openings of various sizes.

The resolution is defined as the minimal separation between points that reveals a certain level of contrast between them and, in terms of gratings, the accuracy of the image depends on the number of diffracted orders that the microscope can capture. According to Abbe criterion, the only ways to optimise lateral resolution are to decrease the imaging wavelength (λ), to increase the numerical aperture (NA) of the objective or to use an imaging medium having a large refractive index (n); in fact its expression is given by:

$$d_{lateral} = \frac{1.22\lambda}{2\,NA} \tag{3.9.68}$$

Thus, the image spot size produced by a 20x magnification objective having a numerical aperture of 0.40 in NIR light ($\sim 780nm$) is approximately 1.2 μm, whereas the spot size produced by a 100x objective of 1.4 numerical aperture is approximately

0.34 μm, almost a quarter of the previous one.

In the axial direction the diffraction limit is approximately three times larger and it is equal to:

$$d_{axial} = \frac{1.4\lambda n}{NA^2} \tag{3.9.69}$$

In CARS microscopes, the intrinsic nonlinear nature of the process confines the generation of the signal in the focal volume, without requiring any spatial filtering.

Notably an important role in the resolution issue is related to the objectives whose main characteristic is the numerical aperture $NA = n\,sin(\alpha)$, n is the refractive index of the medium between the specimen and the objective and α is the one-half of the objective angular aperture. As seen previously, numerical aperture significantly influences the resolution. As in pratice it is difficult to achieve numerical aperture higher than 0.95 for dry objectives; a material with higher refractive index than air is required to reach the value of 1.6. [171].

It is important to underline that the objective will work at the nominal NA value only if the entire entrance pupil is filled with the exciting laser light. Underfilling will reduce the spatial resolution and the peak intensity. Overfilling will cause some laser light to strike the metal mounting of the objective and it will be lost, also reducing the intensity of the spot.

In addition, for the most demanding imaging conditions low magnification objectives with a high numerical aperture should be chosen: in fact, light collection intensity increases as the fourth power of the numerical aperture, but only decreases as the square of the magnification [172].

The collection of the signal can be done in forward direction and the issue is to collect all the signal emitted by the sample. For this aim it is generally recommended to use another objective with the same numerical aperture; if it is not, an objective with a smaller NA is preferred. In fact, althougth it selects a smaller solid angle, it generates a bigger focus waist radius, that allows to recover the entire signal generated in the focal plane.

In addition to the spatial resolution achieved by the microscope, it should be considered the XY translation stages, that move the sample. In order to reach optimal performing condition, maximum positioning accuracy and stability, it is generally

suggested to use high-precision translation stages, typically expensive piezo-electric devices, that guarantee faster scanning and high resolution, up to 0.1 nm. Nevertheless, it is not possible to take advantage of the latter property, if the focus spot size is much bigger than XY translation step. Estimating a spot size of about $1.2\,\mu m$, it is reasonable using XY scanner stages with one-step resolution of about $0.05\,\mu m$.

As well as the spatial resolution, which is fundamental in imaging experiment, the experimental spectral resolution must also be considered. It significantly depends on the spectrometer used in the setup; in fact the observed signal $S[\lambda]_{obs}$ is given by the convolution of the resolution of the spectrometer $R[\lambda]$ and the real lineshape $S[\lambda]_{sam}$, associated to the sample:

$$S[\lambda]_{obs} = R[\lambda] * S[\lambda]_{sam}$$

This means that when the signal linewidth is significantly greater than the spectral resolution, the effect can be ignored and one can assume that the measured resolution is the same as the signal resolution.

In dispersive array spectrometers, there are three main factors that influence the spectral resolution of a spectrometer: the slit, the diffraction grating and the detector. The slit determines the minimum image size that the optical bench can form in the detector plane. The diffraction grating sets the total wavelength range of the spectrometer. The maximum number and size of discrete points, in which the spectrum can be digitized, depends on the detector. Thus, the spectral resolution ($\delta\lambda$) can be expressed as follow:

$$\delta\lambda = \frac{RF \cdot \Delta\lambda \cdot W_s}{n \cdot W_p} \tag{3.9.70}$$

W_s is the slit width, $\Delta\lambda$ the spectral range of the spectrometer, W_p the pixel width and n the number of pixels in the detector. As the resolution is defined as a FWHM, whose determination requires at least three pixels, the resolution factor (RF) is related to both slit and pixel widths: if $W_s = W_p$ the spectral resolution is equal to three times the pixel resolution ($\Delta\lambda/n$). In this case, the resolution factor is equal to 3.

In our experimental setup, we use a Photon Control SPM-002-E spectrometer, which is combined with a Toshiba TCD1304 CCD: it has a 25 μm slit, a 3648 pixel detector and a wavelength range of $20 - 1090$ nm. Its resolution is about $1.2/2\,nm$.

Generally gratings do not diffract incident polychromatic light with uniform efficiency. The overall shape of the diffraction curve is determined mainly by the groove facet angle, otherwise known as the blaze angle. Thus, it is possible to determine the blaze wavelength that corresponds to the maximum peak efficiency. Its plain operation depends on keeping the alignment of grating and detector safe. It follows that this instrument is particularly fragile and, if it is not handled with care, the misalignment of the grating could cause a shift of the measured spectrum. For this reason, it is important to calibrate the spectrometer during the measurements and quantify this potential shift in wavelength.

Focusing condition and sample damaging considerations

Graphene, although its reduced dimensionality, has a quite high absorption ($2.3 \pm 0.1\,\%$); therefore, sample damaging issues has to be taken into account under the tight focusing conditions which are required to achieve the desired spatial resolution.

First of all, after mounting the sample on the XY translational stages, it is necessary to identify those graphene flakes, that have been already characterised by means of spontaneous Raman spectroscopy, in order to be able to compare CARS measurements with SR data.

This early stage could be done by considering transmission and reflection properties of graphene. As it has been already explained in section 1.4, the opacitiy of each graphene layer is $2.3 \pm 0.1\,\%$ and it is practically independent of wavelength [7]. Then the identification of graphene on the substrate is obtained by the raster scanning of the sample, exploiting the transmitted light. The sample is backlit with a diode led lighting and the light, after have been focused onto the sample and then collected, is carried into a 1280 x 1024 pixels CMOS camera with monochrome sensor (Thorlabs DCC1545M). As long as the transmission of multilayer graphene can be expressed as $T \approx 1 - N\pi\alpha$, where N is the number of layers and α the fine structure constant, the contrast in transmission is negative. In fact the detected

intensity from graphene is smaller than that from the substrate and it appears that the darker color corresponds to the thicker sample. Thereby, as N decreases and tends to 1, the contrast significantly decreases, making a single monolayer almost imperceptible on the camera with respect to the substrate.

In this case, we have to introduce alternative methods for the identification; for example we can collect the transmitted Stokes pulse, introducing a 805 nm shortpass dichroic mirror after the condenser, and directly measuring the transmitted power through the sample.

Otherwise it is possible to observe on the camera the reflection of pump and Stokes pulses. Looking at the reflection, the contrast is higher and positive as the reflected light from a graphitic flake is compared against the low background reflection of a transparent substrate [173] [174] [175]. This last method is really useful also to check the focusing condition on the sample and to obtain a preliminary alignment to reach spatial overlap of the two beams.

Another possibility is to adopt NVRB as contrast method. As the third order susceptibility of graphene is higher than in the substrate, translating the coverslip along z-axis, which is light propagation's direction, we can decide for out-focus or in-focus condition, analysing glass-sample and sample-air interfaces in order to enhance resonant-non resonant ratio.

Acquisition times in imaging

Acquisition time in imaging mode is a critical issue, as it is required to have an experimental setup capable of fast scanning with high resolution. Many variables affect the acquisition speed, including the size of the image area, the number of pixels required and the acquisition time per pixel, which is itself dependent on the Raman intensity of the sample.

Traditional Spontaneous Raman spectral imaging has always been limited by relatively long acquisition times: typically they can be in the order of 1 -10 s per point, or longer, resulting in total measurement times of about hours or even days. Recently, ultrafast Raman spectral imaging techniques have been developed, that drastically reduce measurement times down to 5 ms/point: unfortunately these

methods cannot be used for every kind of sample, according to their Raman cross section.

The enhancement of Raman intensity in nonlinear coherent Raman spectroscopy allows to significantly reduce acquisition times, due to a more intense signal. In our case, the acquisition time per pixel varies from 200 ms in graphite to 1 s in monolayer graphene. It follows that acquiring a 3600 pixels image requires from 6 minutes up to a hour. Nevertheless, this estimation is slightly underrated, because we should also consider the speed of translation stages, the processing and saving times of the Labview control program. More realistically, a 3600 pixels narrowband CARS image requires up to two hours in our experimental setup [176].

3.9.1 Graphene sample and CW Raman Characterization

Exfoliated graphene samples are provided by "Cambridge Graphene Centre" (Prof. A. Ferrari) and are produced by micro-mechanical cleavage of bulk graphite and deposited on a Si substrate. SLG is grown on a 35μm Cu foil, following the process described in Refs.23,177. The substrate is heated to 1000°C and annealed in hydrogen (H_2, 20 sccm) for 30 minutes. Then, 5 sccm of methane (CH_4) is let into the chamber for the following 30 minutes so that the growth can take place [23, 177]. The sample is then cooled back to RT in vacuum (∼1 mTorr) and unloaded from the chamber. The sample is characterized by CW Raman spectroscopy using a Renishaw inVia Spectrometer equipped with a 100x objective. The Raman spectrum measured at 514 nm is shown in Fig.3.9 (red curve). This is obtained by removing the non-flat background Cu PL [178]. The absence of a significant D peak implies negligible defects [12, 107, 179, 180]. The 2D peak is a single sharp Lorentzian with FWHM(2D) $\sim$ 23cm^{-1}, a signature of SLG [107]. Pos(G) is $\sim$ 1587cm^{-1}, with FWHM(G) $\sim$ 14cm^{-1}. Pos(2D) is $\sim$ 2705cm^{-1}, while the 2D to G peak area ratio is $\sim$ 4.3. SLG is then transferred on glass by a wet method [19]. Poly-methyl methacrylate (PMMA) is spin coated on the substrate, which is then placed in a solution of ammonium persulfate (APS) and deionized water. Cu is etched [19, 23], the PMMA membrane with attached SLG is then moved to a beaker with deionized water to remove APS residuals. The membrane is subsequently lifted with the target

substrate. After drying, PMMA is removed in acetone leaving SLG on glass. The SLG quality is also monitored after transfer. The Raman spectrum of the substrate shows features in the D and G peak range, convoluted with the spectrum of SLG on glass (blue curve in Fig.3.9). A point-to-point subtraction is needed to reveal the SLG features. After transfer, the D peak is still negligible, demonstrating that no significant additional defects are induced by the transfer process, and the fitted Raman parameters indicate p doping $\sim$ 250meV [181, 182].

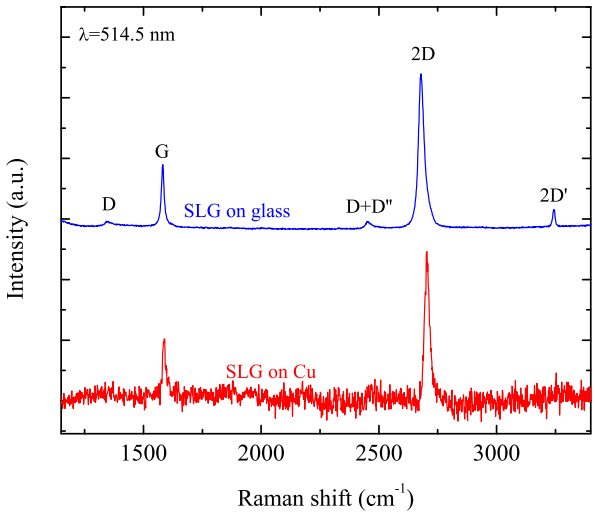

Figure 3.9: CW Raman spectra of SLG. Raman response of SLG on Cu (red line), and on glass (blue line) after the transfer from Cu substrate. In the latter case, the substrate spectrum is subtracted

3.10 Time-delayed CARS

CARS and NVRB are simultaneously generated by two light-matter interactions with PP and a single interaction with SP with different time ordering, see Figs.3.10a-b. Consequently, $P^{(3)} \propto E_P^2 E_S^*$. However, the temporal constrains for such interactions are significantly different for the two cases. As shown in Figs.3.10a-b, in the case of NVRB the three interactions must take place within the coherence time of the involved electronic excitation, which in SLG is $\sim$ 10fs [85, 86], i.e. much shorter than the pulses duration ($\sim$1ps). Hence, $P^{(3)}_{NVRB}(\omega_{as})$ is only generated during the temporal overlap between the two pulses $P^{(3)}_{NVRB} \propto E_P^2(t-\Delta T)E_S^*(t)$

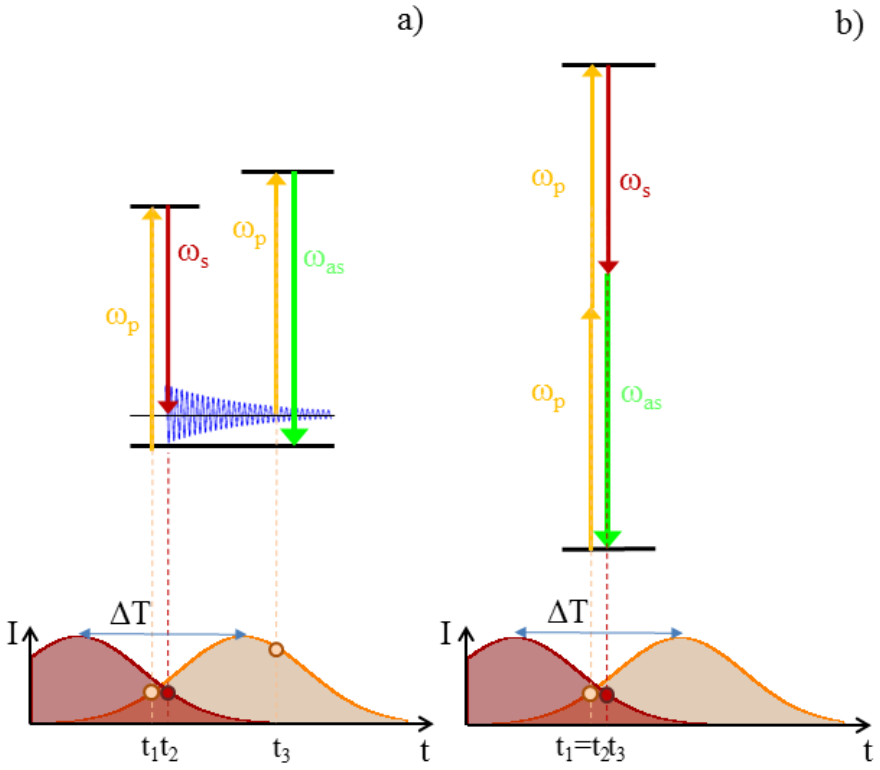

Figure 3.10: Temporal constraints for the sequence of the field-matter interactions (represented by circles on top of the pulse envelopes), for CARS (a) and NVRB (b).

(the three field interactions, in a representative NVRB event, are indicated by the three nearly coincident dots in Fig.3.10b). In CARS, however, the electronic lifetime only constraints the lag between the first two interactions which generate the vibrational coherence (the two stimulating field interactions are represented by the two nearly coincident dots in Figs.3.10a). This can be read out by the third field interaction within the phonon coherence time, $\tau \sim$ 1ps [44]. Thus, $P^{(3)}_{CARS} \propto E_P(t-\Delta T)E^*_S(t)\int_{-\infty}^{t} E_P(t'-\Delta T)e^{-t'/\tau}dt'$ [183].

Therefore, ΔT can be used to control the relative weight of $P^{(3)}_{CARS}$ and $P^{(3)}_{NVRB}$ [183–188]. For positive time delays within a few τ, $P^{(3)}_{CARS}/P^{(3)}_{NVRB}$ is progressively enhanced.

FWM intensity I_{as} is measured as a function of the frequency difference $\omega_p - \omega_s$. As pump frequency is fixed at $\omega_p \sim$ 784nm, the full spectrum is obtained by tuning Stokes wavelength between 850 and 940 nm, having access to SLG G-phonon. As

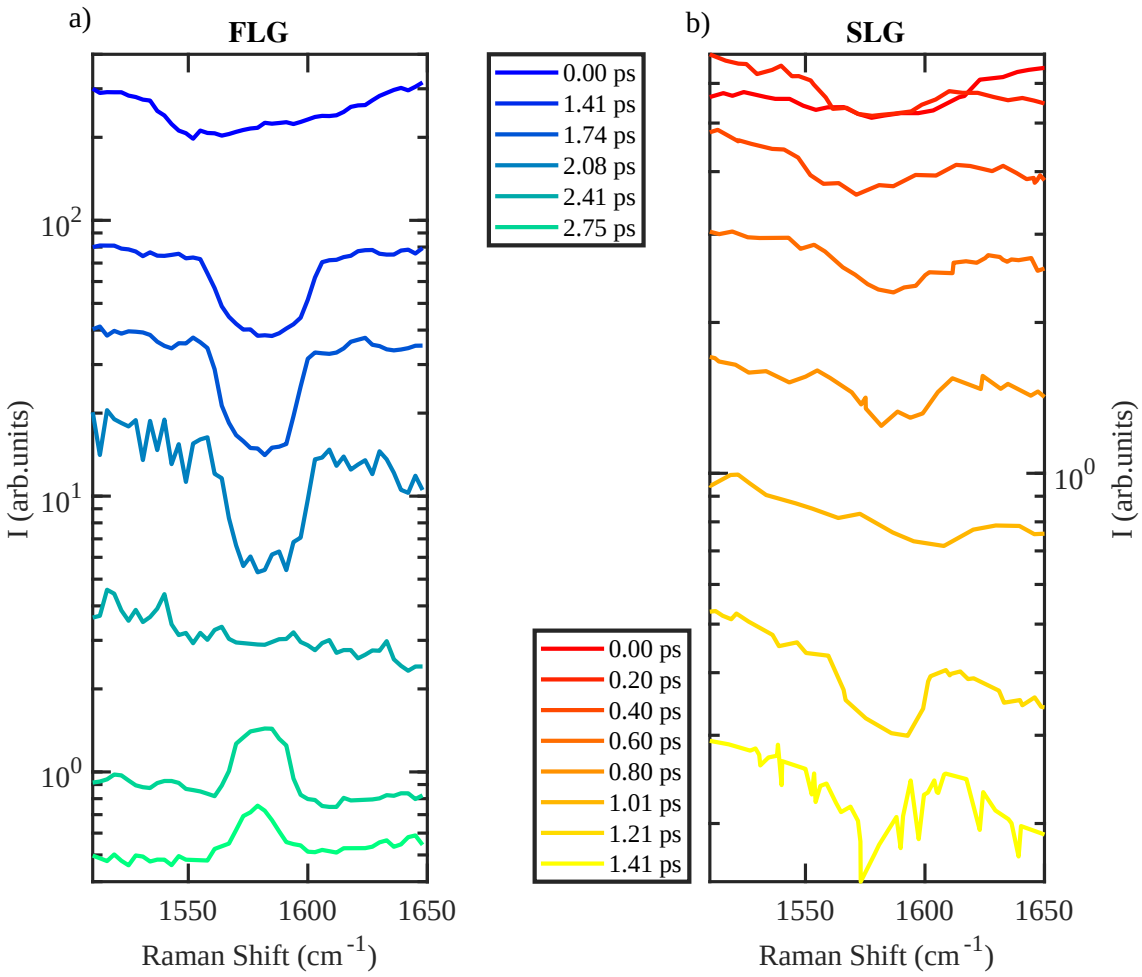

Figure 3.11: Narrowband CARS spectra as a function of ΔT in FLG (a) and SLG (b). Data are normalized by SP intensity. Exposure time are 200 ms/pixel (a) and 1 m/pixel (b).

SP power could change with wavelength, the signal is normalized by dividing for the SP intensity. In Fig.3.11, FWM intensity for different time delays ΔT between pulses is shown in both FLG (panel a) and SLG (panel b). For ΔT shorter than the vibrational dephasing time τ ~1.2ps [44], a Lorentzian dip at $\omega_{as} = \omega_P + \omega_G$ appears on the top of a background, as previously reported [140]. For $\Delta T > 2$ps, the dip lineshape evolves into a peak shape at the G phonon energy. Fig.3.11.b shows that SLG signal intensity is reduced with respect to FLG ($\sim$ 25 times less intense at $\Delta T = 0$ ps), implying a worse signal-to-noise ratio in the spectra and hampering the detection of CARS for $\Delta T > 1.4$ps, where the crossover to peak

lineshape is expected, based on the FLG measurements. This can be explained in terms of CARS and NVRB signals cross sections, which depend quadratically on the number of scatterers [138].

Notably, no dispersive features are observed at any ΔT, unlike what expected for the interference between NVRB and CARS [189]. Furthermore, our data reveal that the FWM response cannot be fully explained in terms of Fano resonance [140] (Eq.3.7.64), as this phenomenological description does not predict the absence of dispersive lineshape. Nevertheless, comparing our data with simulation in Fig. 3.4, we conclude that the conventional CARS description is not able to explain our data. An additional analysis is required.

3.11 Resonant CARS in graphene: a diagrammatic approach

The diagrammatic scenario, introduced in the previous sections and simulated in Fig. 3.4, is commonly applied to biological systems, wherein the electronic excited states involved in the processes are virtual states. We say that the processes are electronically non-resonant.

The cases of SLG and FLG, however, are different as they are resonant under any near infrared excitation [56]. Notably, among the possible processes, we consider only the dominant case $\tilde{\nu}_{ea} = 2\tilde{\nu}_P$, as resonance effects are enhanced by increasing the photon energy [190,191]. Moreover, as we are going to measure the signal related to G-phonon ($q \sim 0$), only one electronic level must be included in the calculation and, consequently, the nonlinear response can be derived assuming $\omega_{ba} = \omega_{dc} = \omega_P$.

Resonance implies an opposite sign in the CARS response, i.e. a spectral dip in $\Im(\chi^{(3)}_{CARS})$, related to two extra imaginary unit contributions in the denominator of Eq. 3.6.58, $(\omega_P - \bar{\omega}_{ba})$ and $(\omega - \bar{\omega}_{da})$, wherein the $i\gamma_{ba}$, $i\gamma_{da}$ components dominate. Also, the $-i$ contribution from $(2\omega_P - \bar{\omega}_{ea})$ results in a NVRB dominated by the imaginary part. This effect are highlighted by comparing Fig.3.4 with Fig.3.12. Clearly, the third term in Eq. 3.6.60 has to be replaced with the contribution from the interference of the spectral dip $\Im(\chi^{(3)}_{CARS})$ with the imaginary part $\Im(\chi^{(3)}_{NVRB})$.

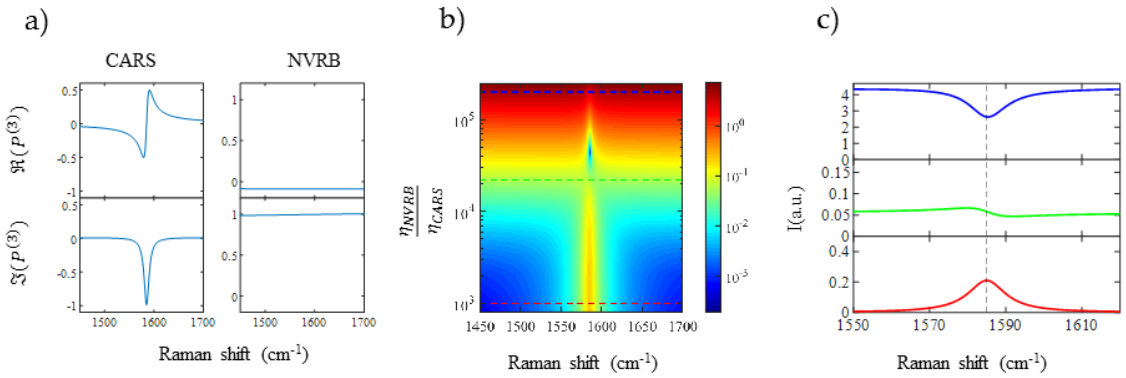

Figure 3.12: CARS and NVRB spectral shapes for derived from Eqs. 3.6.58 and 3.6.59 in the electronically resonant case, considering $\tau_{ba} = \tau_{da} = \tau_{ea} = 10$fs [86], $\gamma_{ca} = \Gamma_G/2 = 6\text{cm}^{-1}$ [44](where $\Gamma_G = FWHM(G)$). In panel (a) normalized $\Re e(P^{(3)}_{CARS})$, $\Im m(P^{(3)}_{CARS})$ and $\Re e(P^{(3)}_{NVRB})$, $\Im m(P^{(3)}_{NVRB})$. Colormaps indicate I^R_{as} for different ratios $\eta_{\text{NVRB}}/\eta_{\text{CARS}}$. In panels (c), a selection of profiles corresponding to three ratios from the colormap is reported: $\eta_{\text{NVRB}}/\eta_{\text{CARS}} = 0.1, 3, 20$ represented in red, green and blu respectively.

This leads to a signal that, under the electronic resonant regime, reads as [99]:

$$\begin{aligned} I(\omega_{as})^R &\sim |P^{(3)}_{NVRB}|^2 + |P^{(3)}_{CARS}|^2 + 2\Im(P^{(3)}_{NVRB})\Im(P^{(3)}_{CARS}) \\ &\propto |\chi^{(3)}_{NVRB}|^2 + |\chi^{(3)}_{CARS}|^2 + 2\Im(\chi^{(3)}_{NVRB})\Im(\chi^{(3)}_{CARS}) \end{aligned} \tag{3.11.71}$$

which indicates that the total FWM, at the phonon frequency, can be either a negative dip or a positive peak depending on the ratio between the resonant and the non resonant susceptibilities $(\chi^{(3)}_{CARS}/\chi^{(3)}_{NVRB})$, which is strictly related to the material properties [99]. Fig.3.12 shows the overall FWM response as a function of different ratio $\eta_{\text{NVRB}}/\eta_{\text{CARS}}$. Such interplay between NVRB and CARS unambiguously indicates that in graphene the electronically resonant pathways dominate over the non resonant ones. Notably, despite that for a given material the ratio $\eta_{\text{NVRB}}/\eta_{\text{CARS}}$ is fixed since it depends only on the material properties, the relative weight of the two FWM contributions can be tuned by using pulsed excitation and varying the temporal overlap between PP and SP fields [183], i.e. changing ΔT.

Notably, the electronically resonant diagrammatic scenario is able to retrieve the dip lineshape, observed in our experimental data (Fig.3.11), nevertheless a more

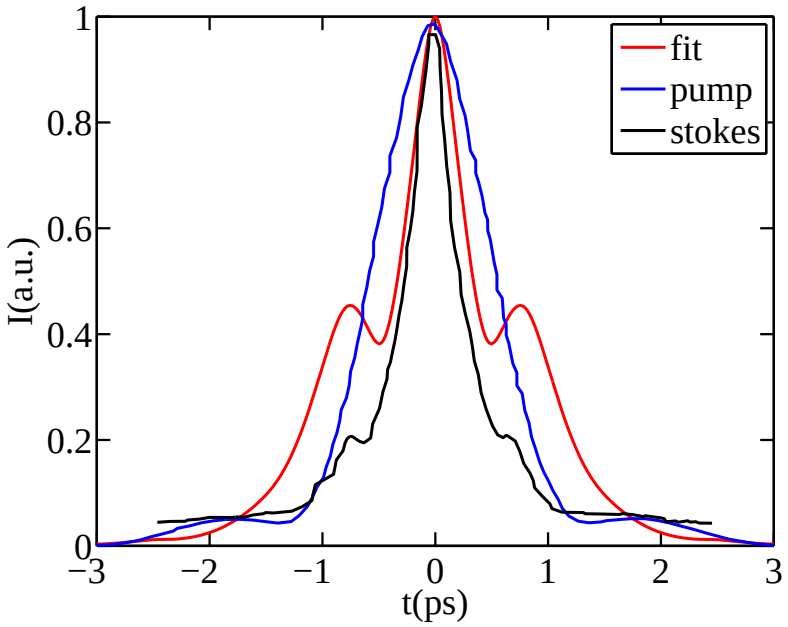

Figure 3.13: Second harmonic autocorrelation of PP (blue line) and SP (black line). The red line simulates the data using the profile obtained from the best fit (colored dashed lines).

quantitative picture can be derived by taking into account the temporal profiles of PP and SP. As model parameters in Eqs. 3.6.55 and 3.6.56, we use $\tilde{\nu}_{ca}$=1580cm^{-1} [12], while $\tau_{da} = \tau_{ba} = \tau_{ea} = 10 \pm 2$ fs, $\tau_{ca} = 1.1 \pm 0.1$ ps and the relative amplitude between NVRB and CARS contributions $\frac{\eta_{CARS}}{\eta_{NVRB}} = (3.0 \pm 0.7) \cdot 10^{-5}$ [44] are obtained as best fit to the experimental data (in very good agreement with Refs. [86]). To simplify the calculation, we assume the same temporal profile for PP and SP and in Fig. 3.13 the simulated autocorrelation profile (red line) is compatible with the experimentally measured ones (black and blue lines). The resulting spectra (colored dashed lines in Fig. 3.14), evaluated by scanning the PP frequency and the inter-pulse delay, are in good agreement with the experimental data with a single adjustable parameter: $\frac{\eta_{CARS}}{\eta_{NVRB}}$, combined with Eqs. 3.6.58 and 3.6.59, allows us to extract the ratio between the CARS and NVRB third order nonlinear susceptibilities: $\frac{|\chi^{(3)}_{CARS}|}{|\chi^{(3)}_{NVRB}|} \sim 1.3$ at the G phonon resonance.

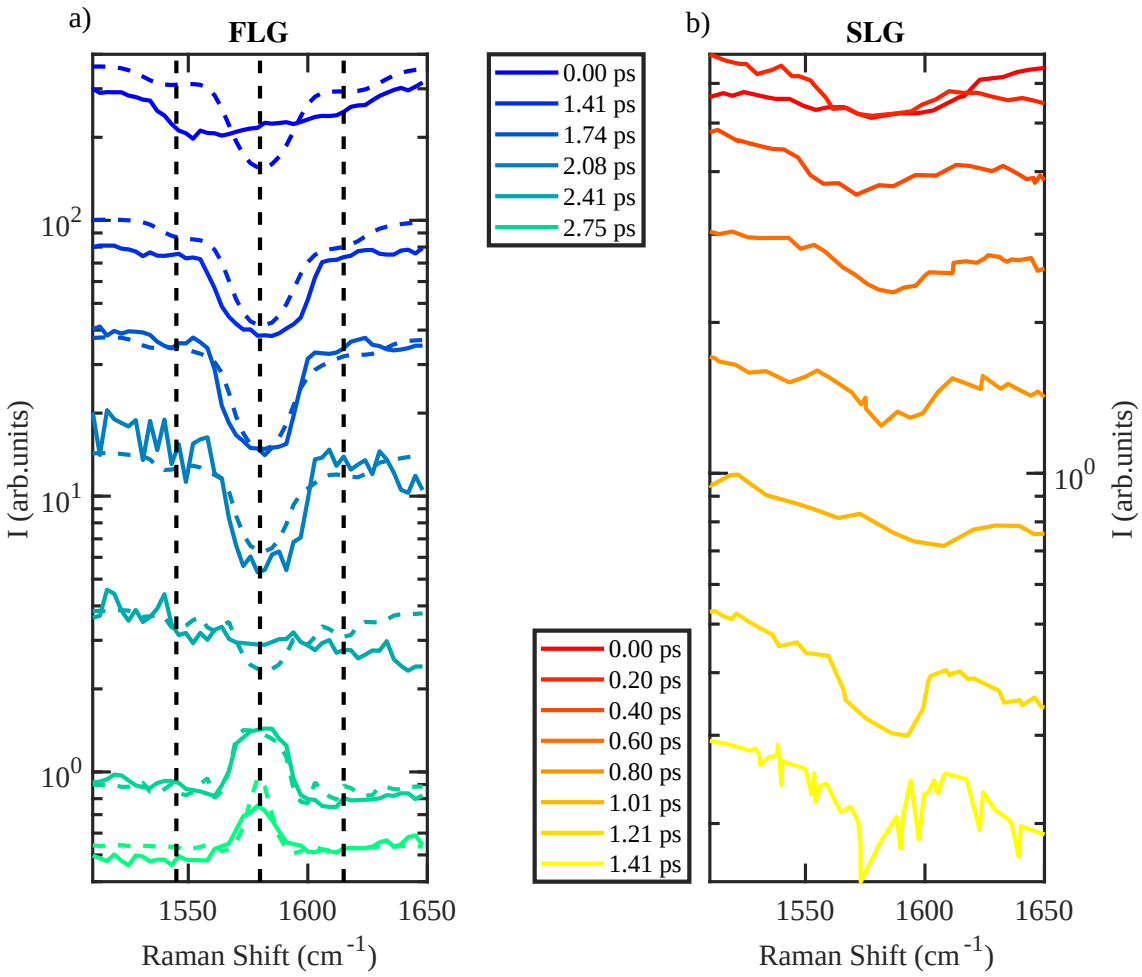

Figure 3.14: Narrowband CARS spectra as a function of ΔT in FLG (a) and SLG (b). Data are normalized by SP intensity. Exposure time 200 ms/pixel (a) and 1 m/pixel (b). In (a), coloured dashed lines are the fit calculated from the quantum treatment of the material through the density matrix description reported in the text. Vertical black dashed lines indicate 3 energies ($\tilde{\nu}_{1,2,3} - \tilde{\nu}_P = 1545$, 1576, 1607 cm^{-1}), taken as reference for FLG CARS microscopy.

3.12 CARS Imaging

Once we have addressed the pecular dip lineshape to the interference between CARS and NVRB, we evaluate how to use it to develop an imaging protocol with vibrational sensitivity. In literature Hendry et al. [157] has already exploited third-order nonlinear properties of graphene as a tool for imaging and quantifying graphene flakes. However, they set up their measurements by using NVRB, choosing pump

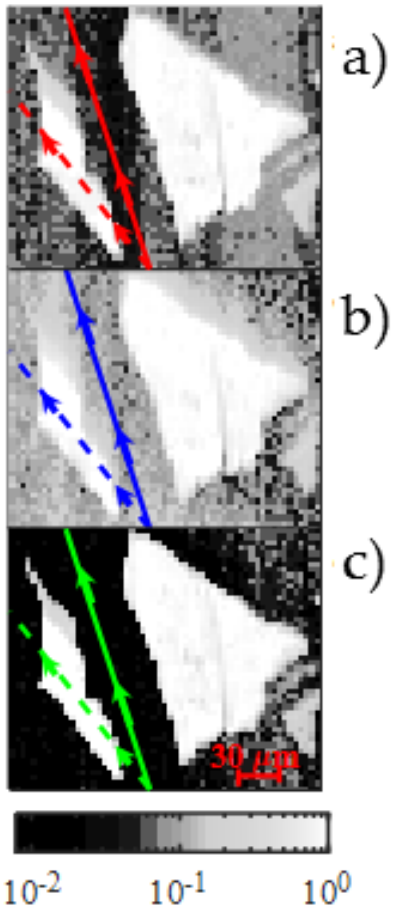

Figure 3.15: Nonlinear optical images of FLG measured under non vibrationally resonant (a) condition at 699nm and resonant (b) 697.5nm at $\Delta T = 1.7$ps. Panel (c) shows CARS image, obtained by the spectral dip (see Eq.3.12.72). The coloured solid and dashed lines indicate the path represented in Fig.3.17.

and Stokes wavelegths in order to avoid coherent anti-Stokes Raman scattering. This method has a notable ability to discriminate sample (whose pixel intensity is indicated with I_g) from substrate (I_{sub}) and it can be quantified in terms of 1) I_g compared to I_{sub}, evaluated as the difference $I_g - I_{sub}$; 2) the proximity of I_{sub} to $I = 0$. These two features can be quantified by the selectivity S:

$$S = \frac{|I_{gr} - I_{sub}|}{I_{sub}} \sim 1.7 \cdot 10^6$$

Nevertheless, this imaging protocol completely lacks of chemical sensitivity. It means that if we chose a substrate with high nonlinearity, this parameter S would be sig-

nificantly reduced. For this reason, in our work we want to exploit the resonant contribution, that will be the basis for a microscopy technique able to identify different samples on the same substrate by the tuning pulses' wavelength in order that their frequency differencecan match features of Raman spectra, singular to the different regions. Furthermore, it makes possible to discriminate the sample on different substrates, even with high nonlinearity as metals.

Notably, the suppression of NVRB produces also a reduction of resonant component, decreasing severely the intensity of the signal and consequently image contrast. To overcome this limitation, we decide to choose a condition for the delay between pump and Stokes pulses corresponding to a dip lineshape, alike the trace at $\Delta T = 1.2$ ps in Fig. 3.11. The vibrationally resonant contribution I_{vib} can be isolated by subtracting from the I_2 FWM signal at $\tilde{\omega}_2 - \tilde{\omega}_P \sim \tilde{\nu}_G$, the NRVB obtained by linear interpolation of the spectral intensities measured at the two frequencies at the opposite sides of vibrational resonance ($\omega_1 - \omega_P$=1545cm$^{-1} < \omega_G$ and $\omega_3 - \omega_P$=1607cm$^{-1} > \omega_G$):

$$I_{vib} = I_1 - I_2 + \frac{\omega_2 - \omega_1}{\omega_3 - \omega_1}(I_3 - I_1) \tag{3.12.72}$$

where the indexes i=1,2,3 refer to data at ω_1, ω_2, ω_3. This subtraction method allows us to isolate the term $\Im(\chi^{(3)}_{NVRB})\Im(\chi^{(3)}_{CARS})$ in Eq. 3.11.71, that is vibrationally resonant and contains the phonon information about energy and lifetime.

Figs.3.15(a-c) plot nonlinear optical images measured at two ω_S, corresponding to vibrationally non resonant and resonant conditions (a-b). Extracting for each image pixel I_1 (Fig.3.15.a), I_2 (Fig.3.15.c) and I_3 (not shown), needed in Eq. 3.12.72, we obtain an image with high signal-to-noise ratio, suppressing the signal not generated by FLG, as in Fig.3.15.c. This procedure provides images with vibrational sensitivity and signal intensities comparable to those of NVRB, for which sub ms pixel dwell times have been demonstrated with a photomultiplier [157]. In our case the images in Fig.3.15 are obtained with a pixel dwell time $\sim$ 200 ms using a Si-CCD array, aiming at a complete spectral characterization, and scanning the sample at fixed ΔT with step motor stages. Figs.3.16 show the pixel intensity histogram. This highlights a bimodal distribution: one corresponding to the most intense pixels, associated to FLG (I_g), another related to the weaker substrate signal (I_s). As we

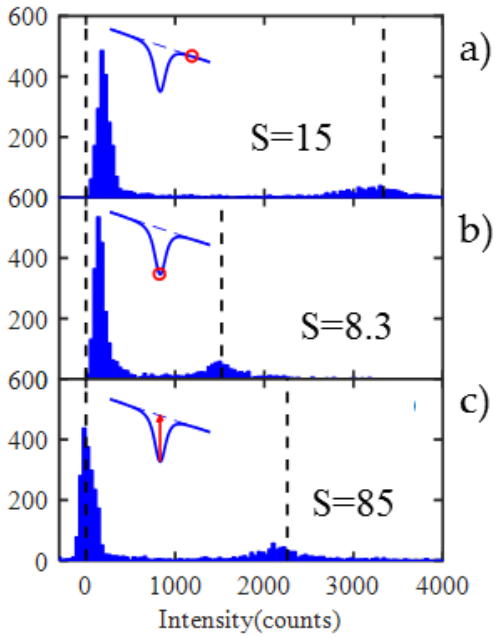

Figure 3.16: Intensity histograms of Fig.3.15. The corresponding selectivity S is also reported. The black dashed lines represent the colormap boundaries Fig.3.15.

have already hinted, the image quality can be quantified by the selectivity S in order to compare the images: $S = \frac{\overline{I}_g - \overline{I}_s}{\overline{I}_s}$, where $\overline{I}_g$ and $\overline{I}_s$ are the mean intensities of FLG and substrate, corresponding to the local maxima in the histograms. It is clear that the Fig.3.16.c reveals an higher S with respect to the other two images in Fig. 3.15: consequently we can confirm that it is a good approximation, although at the linear order, for the evaluation of residual NVRB. Moreover, the physical meaning of this value is quite different respect to FWM imaging: in the latter case, the intensity signal is referred to a physical property that is common to both substrate and sample, as they have a non-zero third order susceptibility. On the contrary, in CARS imaging the intensity signal is due to a vibrational fingerprint of the sample respect to the substrate and associated to $\Im(\chi^{(3)}_{NVRB})\Im(\chi^{(3)}_{CARS})$. Fig. 3.17 reports the corresponding intensity profiles along two scanning paths, in (dashed) and out (full line) of a FLG, shown in Fig.3.15. Notably, the image in Fig.3.15.c (green line) corresponds to the minimal signal intensity from the substrate.

In this chapter, we showed the first evidence of CARS peaks equivalent to the

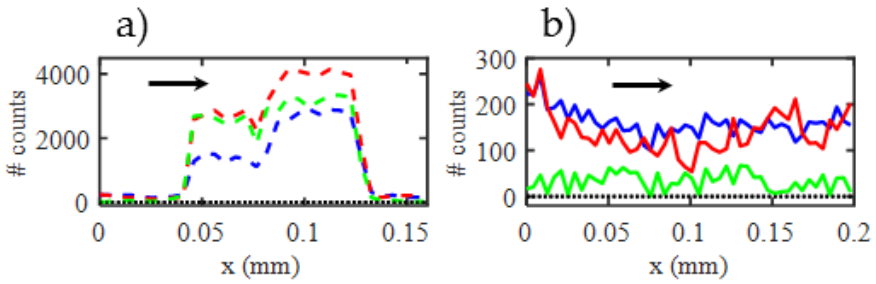

Figure 3.17: Intensity profiles along the scanning paths in and out of a FLG flake (dashed and full lines, respectively) as highlighted in Figs.3.15.

Raman spectrum in graphene. This was possible by introducing an experimental time delayed FWM scheme, which disclosed the chance to disentangle the two processes responsible for SLG FWM lineshape: NVRB and CARS. Indeed, the overall spectral response is described in terms of a third order diagrammatic description of the light-matter interaction. This quantum treatment unambiguously reveals that the presence of the gapless Dirac cones determines the resonant nature of the FWM in graphene. Then the interference between CARS and NVRB results in Lorentzian profiles which are either peaks or dips depending on their relative strength, without facing the dispersive lineshape, typical of the (non-resonant) biological systems.

Chapter 4

Pulsed Spontaneous Raman spectroscopy in graphene

Raman spectroscopy is widely recognized as a fundamental characterization tool for graphene [12]. Indeed, peak position and full-width-at-half-maximum (FWHM) of the different modes reveal information about both electronic and vibrational properties of the system, due to the breakdown of the Born-Oppenheimer approximation [9]. Generally, Raman spectroscopy is performed by using a continuous-wave laser excitation, able to study the equilibrium phonon spectrum with the best spectral resolution. Indeed, as we have already discussed in part I of this work, the fast e-e and e-ph non radiative recombination channels determine the thermodynamic equilibrium between the lattice and the electronic distribution.

In this section, we are interested in understanding the role of e-ph coupling as relaxation channel for an hot Fermi-Dirac distribution in out-of-equilibrium graphene. In particular, we wonder if it is possible to exploit the great advantages of Raman spectroscopy in studying the phononic counterpart of the mechanism also to analyse the out-of-equilibrium phonon behaviour. As the process of interest takes place within ps timescale, graphene has to be excited impulsively. Then, it is necessary to substitute the CW laser beam with a pulsed excitation. Here we use a 3 ps pulse to achieve a trade-off between the narrow excitation bandwidth required for spectral resolution ($\delta\nu \leq 10$ cm^{-1}, being ν the laser frequency, a condition met under CW excitation) and the pulse duration, δt, sufficiently short ($\delta t \leq 10$ ps, achieved using

ultrafast laser sources) to generate an highly excited carrier distribution over the equilibrium ph population, being those two quantities Fourier conjugates: $\frac{\delta\nu}{\delta t} \leq 14.7$ $\mathrm{cm}^{-1}ps$. *Then we study the dependence of both ph frequency and dephasing time on the electronic temperature* T_e.

4.1 T-dependent Raman spectroscopy in graphene: a review

Temperature has a key role in this work. In particular, in the out-of-equilibrium regime impulsively photoexcited in this work, it is fundamental to distinguish between the electrons and the lattice temperature. Actually, they are fingerprints of the relaxation mechanisms that we are interested in. First of all, we are going to discuss about the T-dependence of SLG Spontaneous Raman at the thermodynamic equilibrium in order to highlight the main mechanisms responsible for it.

The effect of temperature on the Raman spectra of graphene has been extensively discussed in the literature both from a theoretical [44, 192, 193] and an experimental point of view [64, 193–197]. Notably, temperature-dependent Raman scattering is important for further understanding some of the physical effects induced by anharmonic phonons, such as thermal expansion, specific heat and thermal conductivity.

Different calculations methods have been applied in order to theoretically predict the phonon behaviour in terms of energy and lifetime as a function of temperature. Lin et al. [193] have adopted a simplified Klemens model in order to studying the dominating anharmonic phonon scattering mechanism. Bonini et al. [44] have determined the finite-temperature properties of the G mode in graphite and graphene from first-principles. Apostolov et al. [192] have calculated both energy and lifetime of G and 2D phonons by using a microscopic model and a Green's function technique.

Most experimental data show a decrease of the G and 2D mode frequencies with increasing temperature [194, 195]. On the contrary, there are some differences in the results of the T-dependence of FWHM(G). Refs. [64, 192–194] observed an increasing FWHM(G) while Ref. [44] a decrease with T. A brief review of the data is reported

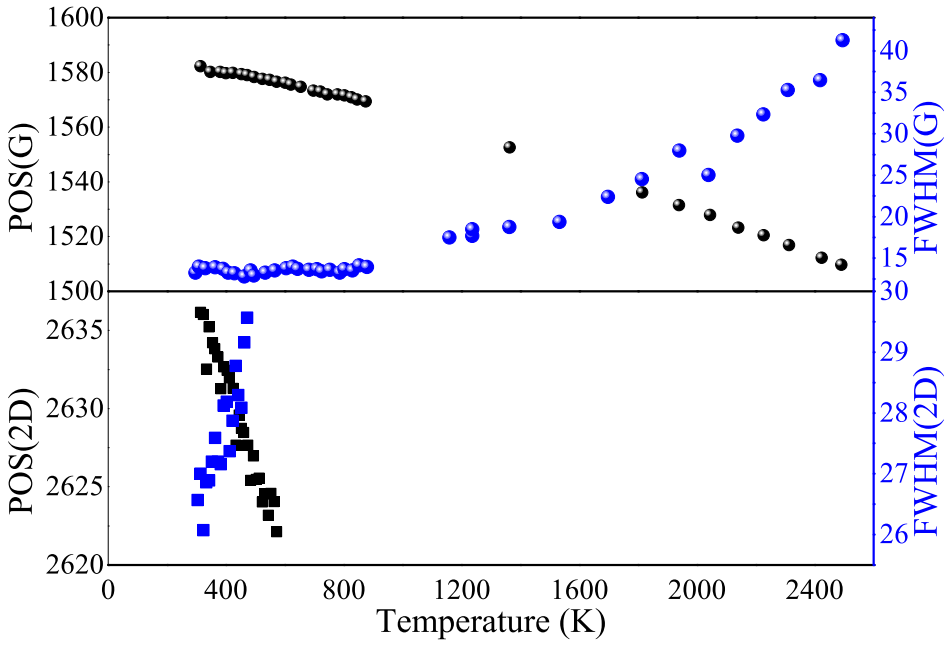

Figure 4.1: Behaviour of POS(G), POS(2D), FWHM(G), FWHM(2D) as a function of temperature at thermodynamic equilibrium, performed by Spontaneous Raman spectroscopy. Blue and black filled circles are from Ref. [196], black filled squares from Ref. [197] and blue filled squares from Ref. [194].

in Fig.4.1.

Both data and simulations show that the SLG Raman response is characterized by the competitive mechanism of two processes: anharmonicity, also called phonon-phonon interactions, and electron-phonon coupling (EPC). Indeed, EPC leads to the hardening of the phonon modes with increasing T, while the anharmonic terms to their softening. In addition, electron-phonon interaction decreases the FWHM of the phonon peak with increasing temperature whereas the anharmonic phononphonon interaction increases it. Experimental data in Fig. 4.1, also confirmed by theoretical predictions [44], reveal the dominant role of anharmonicity in T-dependent SLG Raman spectrum. Actually, EPC is, in most of the cases, a minor correction.

In the following, we introduce the theoretical formalism able to describe EPC.

4.1.1 Theoretical description of the e-ph coupling

The optical phonons modify the distance between neighboring carbon atoms and therefore the electronic band structure. Then the electron-phonon coupling (EPC) can be considered as a perturbation of the SLG Hamiltonian (Eq. 2.2.1). In order to study how they modify SLG response, Feynman diagrams, in their most elementary form, appear a natural choice in perturbation theory [198].

As long as we are interested in the phononic counterpart of the process, whose effects are measurable by means of Raman spectroscopy, we want to develop the perturbation method to evaluate the phonon propagator in the case wherein the phonon Hamiltonian, say $\mathcal{H}_{ph}$ and EPC Hamiltonian, $\mathcal{H}_{EPC}$, cannot be diagonalized in the same basis [199, 200].

In many-body theory, the propagator (or Green Function) describes how a wave propagates through a medium and its expression is deeply associated to the Hamiltonian describing the particle. In the phonon case, the Hamiltonian $\mathcal{H}_{ph}$ is represented by a quantum oscillator of frequency ω_0 [199, 200]:

$$\mathcal{H}_{ph} = \sum_{\mathbf{q},\mu} \hbar\omega_0 \left(b^{\dagger}_{\mathbf{q},\mu} b_{\mathbf{q},\mu} + \frac{1}{2} \right) \tag{4.1.1}$$

where $\mathbf{q} = (q_x, q_y)$ is the wavevector, μ denotes the modes (t for transverse and l for longitudinal), $b^{\dagger}_{\mathbf{q},\mu}$ and $b_{\mathbf{q},\mu}$ are the creation and annihilation operators, respectively. The corrisponding free (non-interacting) Green's function $D^0_{\mu}(\mathbf{q},\omega)$ is given by [198]:

$$D^0_{\mu}(\mathbf{q},\omega) = \frac{2\hbar\omega_0}{(\hbar\omega + i\delta)^2 - (\hbar\omega_0)^2} \tag{4.1.2}$$

where the term $i\delta$ represents the analytical continuation. In order to understand, the physical meaning of $D^0_{\mu}(\mathbf{q},\omega)$, we write the propagator definition as a function of the spectral weight $A^0(\mathbf{q},\omega)$:

$$D^0_{\mu}(\mathbf{q},\omega) = \int \frac{\hbar d\,\omega'}{2\pi} \frac{A^0_{\mu}(\mathbf{q},\omega')}{\hbar\omega + i0 - \hbar\omega'} \tag{4.1.3}$$

$$A^0_{\mu}(\mathbf{q},\omega) = -2\Im m D^0_{\mu}(\mathbf{q},\omega) \tag{4.1.4}$$

It follows that for $D^0_{\mu}(\mathbf{q},\omega)$ in Eq. 4.1.2 we have: $A^0_{\mu}(\mathbf{q},\omega) = 2\pi\delta(\omega - \omega_0)$. In order to catch the physical meaning, we should think of the frequency as energy. Non-interacting particles are the only case wherein specifying the energy implies to

have specified the wavevector, since $\omega = \omega_0$ is the only existing case. Intuitively, for weak perturbations, this condition is no more guaranteed and we simply expect that $A^0_\mu(\mathbf{q},\omega)$ will broaden in frequency around $\hbar\omega_0$. This is what happened in the case of a damped harmonic oscillator where the resonance is broadened and shifted by the damping. If we take a Lorentzian as a phenomenological form for the interacting spectral weight $A_\mu(\mathbf{q},\omega)$, we obtain:

$$A_\mu(\mathbf{q},\omega) = \frac{2\Gamma}{(\hbar\omega - \hbar\tilde{\omega})^2 + \Gamma^2} \tag{4.1.5}$$

$$D_\mu(\mathbf{q},\omega) = \frac{1}{\hbar\omega - \hbar\tilde{\omega} + \Gamma} \tag{4.1.6}$$

where $\tilde{\omega}$ represents the shifted energy, while Γ is the damping.

More in general, as we will explain in a moment, we define the one-particle irreducible self-energy $\Pi_\mu(\mathbf{q},\omega)$ as:

$$D_\mu(\mathbf{q},\omega) = \frac{2\hbar\omega_0}{\hbar\omega + i\delta)^2 - (\hbar\omega_0)^2 - 2\hbar\omega_0\Pi_\mu(\mathbf{q},\omega)} = \frac{1}{D^0_\mu(\mathbf{q},\omega) - \Pi_\mu(\mathbf{q},\omega)} \tag{4.1.7}$$

Its physical meaning is clear. The imaginary part $\Im m\Pi_\mu(\mathbf{q},\omega)$ corresponds to the scattering rate, or inverse lifetime, whereas the real part, $\Re e\Pi_\mu(\mathbf{q},\omega)$ leads to the energy shift of the resonance in the spectral weight, i.e. the shift of the phonon frequency. In other words, $\Pi_\mu(\mathbf{q},\omega)$ contains all the information about the interactions and it is deeply correlated to the physical quantities (phonon frequency and lifetime), that we measure by means of Raman spectroscopy [199, 200].

In the case of G phonon in graphene, we have [198]:

$$\begin{aligned} D(\omega) &= \frac{2\hbar\omega^0_{\mathrm{G}}}{(\hbar\omega + i\delta)^2 - (\hbar\omega^0_{\mathrm{G}})^2 - 2\hbar\omega^0_{\mathrm{G}}\Pi(\omega)} \\ \Delta\mathrm{POS(G)} &= \frac{1}{hc}\mathrm{Re}\left[\Pi(0,\omega^0_{\mathrm{G}},T_{\mathrm{e}}) - \Pi(0,\omega^0_{\mathrm{G}},T_{\mathrm{e}}=0)\right] \\ \mathrm{FWHM(G)} &= -\frac{2}{hc}\mathrm{Im}\Pi(0,\omega^0_{\mathrm{G}},T_{\mathrm{e}}) \end{aligned} \tag{4.1.8}$$

wherein we write explicitly the T_e dependence.

In many-body theory, Eq. 4.1.7, which describes the interacting propagator, is well-known as Dyson's equation. It can be derived by developing $D_\mu(\mathbf{q},\omega)$ in perturbation series of the interacting Hamiltoninan. This would correspond to an infinite set of terms; stopping the iteration at an arbitrary power may lead to misleading

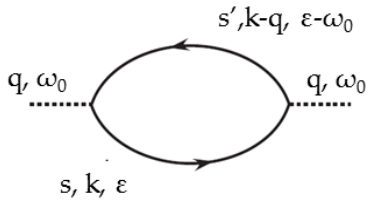

Figure 4.2: Feynman diagram for the self-energy for an optical phonon with a wavevector $\mathbf{q}$ and a frequency ω_0.

results. Hence, the self-energy $\Pi_\mu(\mathbf{q},\omega)$ contains all the possible terms in the series characterized by the phonon state $(\mathbf{q},\omega)$. At the end, the effect of the interacting Hamiltonian, in our case $\mathcal{H}_{EPC}$, leads back to the calculation of the corresponding the self-energy.

Calculation of the self-energy $\Pi_\mu(\mathbf{q},\omega)$

The EPC Hamiltonian for the K point in graphene is given by [201]:

$$\mathcal{H}_{EPC} = -\frac{g}{2}\sum_{\mathbf{q},\mu} V_\mu(\mathbf{q}) e^{i\mathbf{q}\cdot\mathbf{r}}(b_{\mathbf{q},\mu} + b^\dagger_{\mathbf{q},\mu}) \tag{4.1.9}$$

where

$$V_l^K(\mathbf{q}) = \begin{pmatrix} 0 & -e^{-i\phi(\mathbf{q})} \\ e^{i\phi(\mathbf{q})} & 0 \end{pmatrix}, V_t^K(\mathbf{q}) = \begin{pmatrix} 0 & ie^{i\phi(\mathbf{q})} \\ ie^{i\phi(\mathbf{q})} & 0 \end{pmatrix}, \tag{4.1.10}$$

where g is a constant that gives the EPC strength and $\phi(\mathbf{q})$ is the phase associated to $\mathbf{q}$: $\mathbf{q} = [(q\cos(\phi(\mathbf{q}), q\sin(\phi(\mathbf{q}))]$. For the K' point, the corresponding quantities are obtained by the relation $V_\mu^{K'}(\mathbf{q}) = V_\mu^K(-\mathbf{q})^\star$. The EPC self-energy can be depicted in terms of the corresponding Feynman diagram shown in Fig.4.3: it describes the absorption of an optical phonon (dashed line) with a wavevector $\mathbf{q}$ and a frequency ω_0 to create an h-e pair (solid line). Then, the pair is reabsorbed by emitting an optical phonon $(\mathbf{q},\omega_0)$.

We can compute the G-phonon $(q = 0)$ self-energy $\Pi(q = 0, \omega_{\mathrm{G}}^0)$, as for Refs.

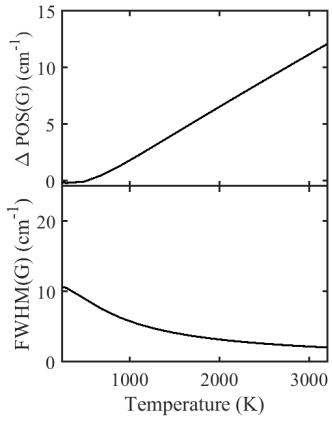

Figure 4.3: The frequency shift Δ POS(G) (upper panel) and broadening FWHM(G) (lower panel) of optical phonon as a function of the temperature.

[9, 45, 202]:

$$\Pi(q=0,\omega_G^0,T_{\rm e}) = \xi \int_0^{\tilde{\epsilon}} d\epsilon\, \epsilon \int_{-\infty}^{+\infty} dz\, dz' \sum_{s,s'} M_s(z,\epsilon) M_{s'}(z',\epsilon) \left[\frac{f_{\rm F}(z-E_{\rm F}) - f_{\rm F}(z'-E_{\rm F})}{z-z'-\hbar\omega_{\rm G}^0 + {\rm i}\delta} \right] \quad (4.1.11)$$

Here, in graphene case, $\xi = g^2/(2\hbar m_{\rm a}\omega_{\rm G}^0 v_{\rm F}^2) = 4.43 \times 10^{-3}$ is a dimensionless constant, $v_{\rm F}$ is the Fermi velocity, $\tilde{\epsilon}$ is the upper cutoff of the linear dispersion $\epsilon = v_{\rm F}|\mathbf{q}|$, $m_{\rm a}$ is the carbon atom mass, $\hbar\omega_{\rm G}^0 = 0.196$ eV the bare phonon energy, δ is a positive arbitrary small number (< 4eV), $g \sim 12.3$eV is proportional to the EPC [45, 202–204], z, z' are the energy integration variables and $f_{\rm F}(z-E_{\rm F})$ is the Fermi-Dirac distribution with Fermi energy $E_{\rm F}$. The two indexes $s, s' = \mp 1$ denote the electron and hole branches and $M_s(z,\epsilon)$ is the corresponding spectral function, which describes the electronic dispersion. FWHM(G) can be further simplified since the evaluation of ${\rm Im}\Pi(0,\omega_{\rm G}^0,T_{\rm e})$ leads to $\delta(z-z'-\hbar\omega_{\rm G}^0)$ in Eq.4.1.11, so that we get:

$$\text{FWHM(G)} = \frac{\pi\xi}{hc} \int_0^{\tilde{\epsilon}} d\epsilon\, \epsilon \int_{-\infty}^{+\infty} dz \sum_{s,s'} M_s(z,\epsilon) M_{s'}(z-\hbar\omega_{\rm G}^0 - E_F,\epsilon) \Big[f_{\rm F}(z-E_F) - f_{\rm F}(z-\hbar\omega_{\rm G}^0 - E_F) \Big] \quad (4.1.12)$$

In the limit of vanishing broadening of the quasiparticle state, the SLG gapless linear

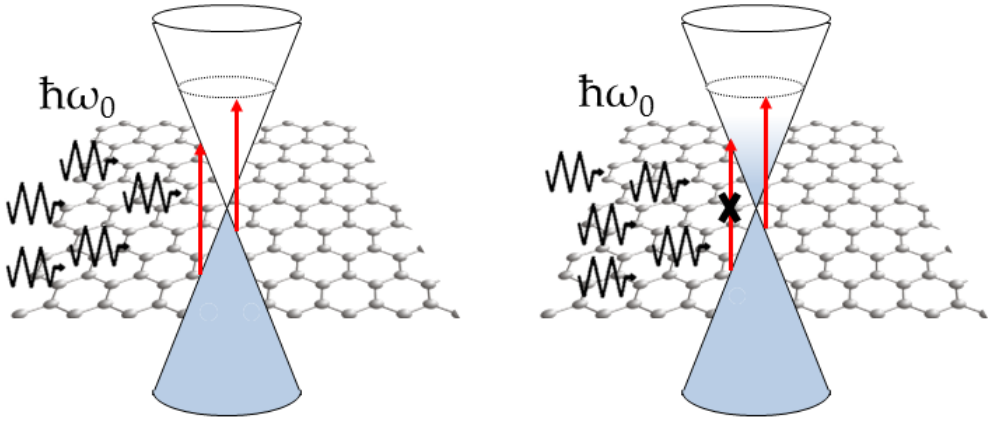

Figure 4.4: Qualitative sketch of the EPC. The zigzag lines represent the G-phonons, whose absorption determines the creation of e-h pair (red arrows). Increasing T_e, the conduction band becomes increasingly populated (right panel) and some transitions become forbidden due to the fact that some electronic final state are already filled. This causes an increase of the G-phonon lifetime.

dispersion is represented by the following spectral function [198]:

$$M_s(z,\epsilon) = \delta(z + s\epsilon), \quad s = \pm 1, \tag{4.1.13}$$

This rules the energy conservation in Eq.4.1.12 and allows only transitions between h and e states with energy difference $2\epsilon = \hbar\omega_{\rm G}^0$. Thus, we get [9, 45, 202]:

$$\mathrm{FWHM(G)} = \mathrm{FWHM(G)}^0 \left[f_{\rm F}(-\hbar\omega_{\rm G}^0/2) - f_{\rm F}(\hbar\omega_{\rm G}^0/2) \right] \tag{4.1.14}$$

where $\mathrm{FWHM(G)}^0 = \frac{\pi\xi\hbar\omega_{\rm G}^0}{2hc} \sim 11\mathrm{cm}^{-1}$ [44], assuming $E_F = 0$. Fig. 4.3 shows the predicted behaviour of Δ POS(G) (upper panel) and FWHM(G) (lower panel) due to EPC. The electron-phonon interaction leads to the hardening of the phonon mode; i.e., with increasing temperature it tries to increase the frequency and to shift the peak to higher energies. This dependence can be understood as a change in the effective force constant due to the reduction of the electronic screening. As $T_{\rm e}$ increases, the conduction band becomes increasingly populated; consequently, the filled states can no longer contribute to the screening process and, as result, the phonon frequency increases with T_e. Eq.4.1.14 also shows that an increasing $T_{\rm e}$ makes progressively less efficient the phonon decay channel related to e-h formation

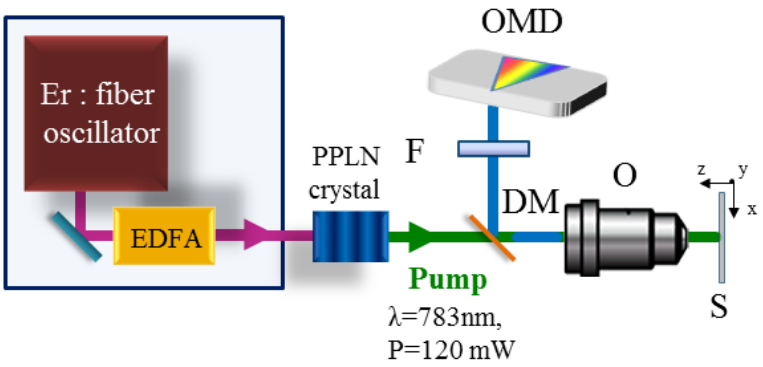

Figure 4.5: CARS setup. EDFA, Erbium-Doped fiber amplified; DM, dichroic mirror; O, objective; S, sample; F, filter; OMD, optical multichannel analyzer. Purple and green lines represent the beam pathway of 1550nm and 784 nm pulses. Blue lines are referred to the emitted Raman signal

leading to an increase of the phonon decay time (see Fig. 4.4). This determines a decrease of FWHM(G) with T_e [44, 192].

4.2 Experimental methods

4.2.1 Pulsed Raman setup

The ps-Raman apparatus, shown in Fig. 4.5, is based on a mode-locked Er:fiber amplified laser, widely described in the Chapter 3; it generates 90fs pulses with $\lambda \sim$ 1550nm at a repetition rate RR=40MHz.

In our setup (Fig.4.5), using SHG in a 1cm PPLN crystal [205], we obtain 3 ps pulses at 783 nm with a$\sim$ 9.5 cm^{-1} bandwidth, shown in Fig. 4.6. The intensity of the laser beam can be adjusted with optical densities. The beam is focused on SLG through a slightly underfilled 20X objective (NA= 0.4), resulting in a focal diameter $D = 5.7\mu$m. To localize the region of interest in the sample and to detect possible demaging effects, a removable white-light can be focused on the sample and the optical image is then detected by a camera. Back-scattered light is collected by the same objective, separated with a dichroic filter from the incident beam and sent

to a spectrometer (with a resolution of 0.028 nm/pixel corresponding to 1.2 cm^{-1}). The overall IRF, therefore, is dominated by the additional contribution induced by the finite excitation pulse bandwidth. Hence, in order to extract the FWHM of the Raman peaks, our data has to be fitted convolving a Lorentzian with the spectral profile of the laser excitation.

When using ultrafast pulses, a nonlinear PL is observed in SLG [61]. Such an effect is particularly intense for the S spectral range [63,91], preventing the clear observation of the Raman peaks in our accessible spectral window. The S signals, measured in this works, are obtained as the difference spectrum of two measurements with excitation frequencies slightly offset by$\sim$130 cm^{-1}, resulting in PL suppression. The background subtraction requires in this case a wider spectral range, at the expenses of spectrometer resolution which is reduced to 0.13 nm/pixel corresponding to$\sim$6 cm^{-1}, as additional contribution to the IRF. Although this procedure allows to isolate the S Raman peaks, the resulting noise level is worse than for AS. For this reason we mostly focus on the AS features.

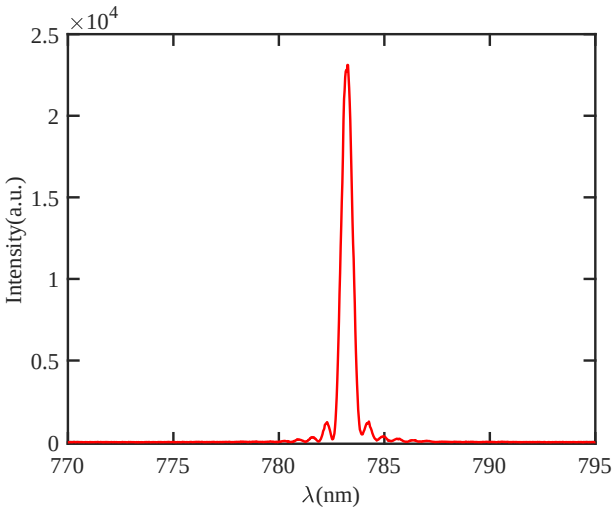

Figure 4.6: Pump pulse spectrum.

4.2.2 CW Raman setup

Continuous-wave Raman measurements are performed in the High Pressure Spectroscopy (HPS) laboratory in the Physics Department, "La Sapienza" University of

Rome (Dr. Claudia Fasolato and Prof. Paolo Postorino). Tha data are collected by means of a commercial Raman micro-spectrometer by Horiba-Jobin Yvon, the LABRAM HR Evolution. The setup includes a 15mW He-Ne laser (∼632.8 nm) as excitation source, a back-scattering geometry, an optical notch filter with additional Bragg filters, an optical microscope with confocal geometry, a xy motorized sample stage and a Peltier cooled multichannel charge coupled device (CCD) detector (1024 X 256 pixel). The 800 mm focal length of the LABRAM HR Evolution ensures a spectral resolution below 1 cm^{-1} (3 cm^{-1}) with the 1800 (600) lines/mm grating.

4.3 Continuous-wave Raman spectroscopy in SLG

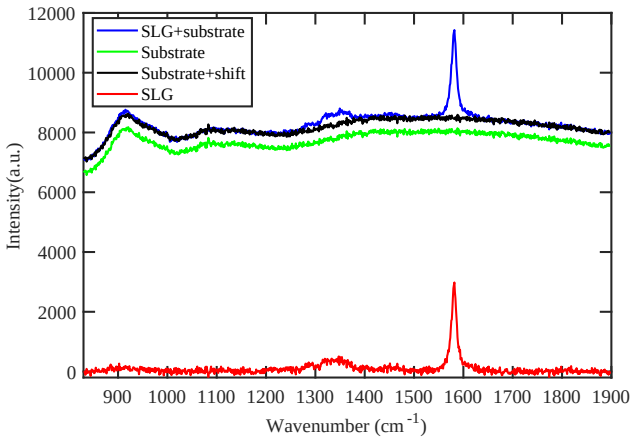

Figure 4.7: CW Raman spectrum of graphene. Blue and green lines correspond to the Stokes emission spectrum by SLG sample and the substrate, respectively. Black line indicates the substrate spectrum shifted upon the SLG one. The difference between blue and red lines is reported in red.

Continuous-wave Raman scattering is performed in SLG sample by means of the microRaman setup, described in section 3.2.1. Fig.4.7 shows the SLG Stokes emission spectrum. We can clearly distinguish the G peak (∼ 1590 cm^{-1}) upon a very intense broad background, mainly due to the substrate (green line). Indeed, by comparing the signal emitted by the sample (blue line) and that carried out on the substrate (green line), it results that the substrate emission, conveniently shifted

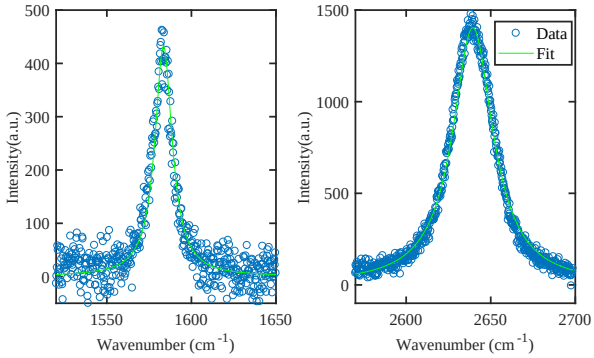

Figure 4.8: G (left) and 2D (right) modes measured by means of CW Raman spectroscopy are reported (blu circles), with their best Lorentzian fit (green lines).

(black line), corresponds to SLG background. The difference between blue and black line can be quantitatively interpreted as the SLG Raman spectrum (red line). It also shows a peak around 1350 cm^{-1}, consistent with the D peak. Its low intensity indicates a low level of disorder and damage in the sample.

Fig. 4.8 shows 2D and G modes (blue circles). Data are fitted with a Lorentzian lineshape and the estimated POS and FWHM are reported below:

$$\begin{aligned} &\mathrm{POS(G)} = (1584.1 \pm 0.7)\mathrm{cm}^{-1} \\ &\mathrm{FWHM(G)} = (1.8 \pm 1.1)\mathrm{cm}^{-1} \\ &\mathrm{POS(2D)} = (2639.4 \pm 29.2)\mathrm{cm}^{-1} \\ &\mathrm{FWHM(2D)} = (29.2 \pm 0.5)\mathrm{cm}^{-1} \end{aligned} \tag{4.3.15}$$

As affirmed in the experimental methods section, most of the pulsed Raman data shown in this chapter are related to the blue side of the spectrum (AS). For this reason, in order to compare CW measurements to the pulsed Raman spectra, we should consider two important aspects related to the 2D mode dispersion with photon energy. First of all, for a given excitation wavelength, a different energy and momentum of the D phonon is involved in the S or AS processes, due to the phonon dispersion in the double-resonant mechanism [206,207] (see Fig.4.9). Hence, in order to measure the same D phonon in S and AS processes, different laser excitations (ν_{laser}) must be used according to [12, 208, 209]:

$$\nu^{S}_{laser} = \nu^{AS}_{laser} + c\mathrm{Pos(2D)}$$

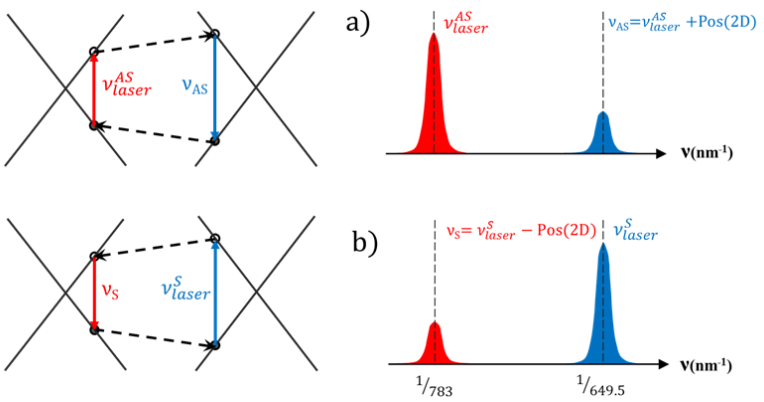

Figure 4.9: AS (a) and S (b) 2D Raman process. The cone representation of the two processes is depicted on the left, while a sketch of the corresponding Raman spectra is shown on the right.

Given our pulsed laser wavelength (784nm), the CW excitation, that corresponds to the same D phonon involved in our pulsed experiment, would be ∼649.5nm. Since we use a 632.8nm He-Ne source, we have to account for the small residual wavelength mismatch by scaling the measured 2D phonon frequency as [12]:

$$\Delta POS(2D) = \frac{d\text{Pos(2D)}}{d\nu_{laser}} = 0.0132/c \tag{4.3.16}$$

Consequently, POS(2D), corrected for D phonon dispersion, is ~ 2634 cm^{-1}.

Fig. 4.10 shows the effect of increasing laser power on the G peak in the Stokes side. Table 4.1 reports POS(G) and FWHM(G) for different laser power. POS(G) and FWHM(G) are nearly constant within the instrumental resolution (~ 1 cm^{-1}) and they are in agreement with values typical for SLG.

P_L	POS(G)(cm^{-1})	FWHM(G)(cm^{-1})
100%	1584.7	12.6
25%	1584.9	12.8
10%	1584.6	10.8

Table 4.1: POS(G) and FWHM(G) for different P_L estimated by fitting spectra in Fig. 4.10 with a Lorentzian lineshape.

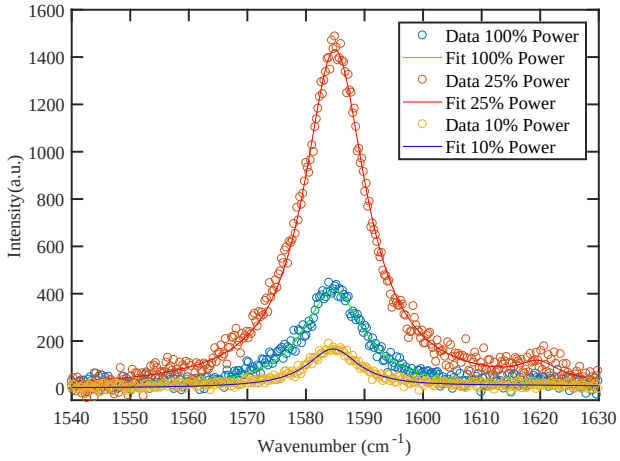

Figure 4.10: SLG Stokes Raman spectra (circles) at different P_L. Lorentzian fit is also reported (solid lines).

4.4 Pulsed Raman spectroscopy in SLG

Fig.4.11 plots the AS and S G peaks, together with fits by Lorentzians (blue lines) convoluted with the laser bandwidth ($\sim$ 9.5 cm^{-1}) and spectrometer resolution ($\sim$ 6 cm^{-1}), which determine the instrumental response function, IRF. We obtain a full width at half maximum of the G peak, FWHM(G)$\sim$ 21 cm^{-1}, larger than the CW one ($\sim$ 12.7cm^{-1}). Similarly, we get FWHM(2D)$\sim$50-60 cm^{-1} over our $P_{\rm L}$ range, instead of FWHM(2D)$\sim$ 29 cm^{-1} as measured on the same sample under CW excitation. The S data have a larger noise due to a more critical background subtraction, which also requires a wider accessible spectral range, as explained in the experimental method section. For this reason, we are going to focus on the AS spectral region

Fig.4.12a plots a sequence of AntiStokes (AS) Raman spectra of SLG excited at 1.58eV, as a function of excitation power $P_{\rm L}$. Notably, it is possible to clearly distinguish SLG vibrational fingerprints (G and 2D modes) upon a broad background. This background stems from hot photoluminescence (PL) due to the inhibition of a full non-radiative recombination under high excitation densities [61–64]. This process, absent under CW excitation in pristine SLG [210], is due to the ultrafast photogeneration of charge carriers in the conduction band, congesting the e-ph de-

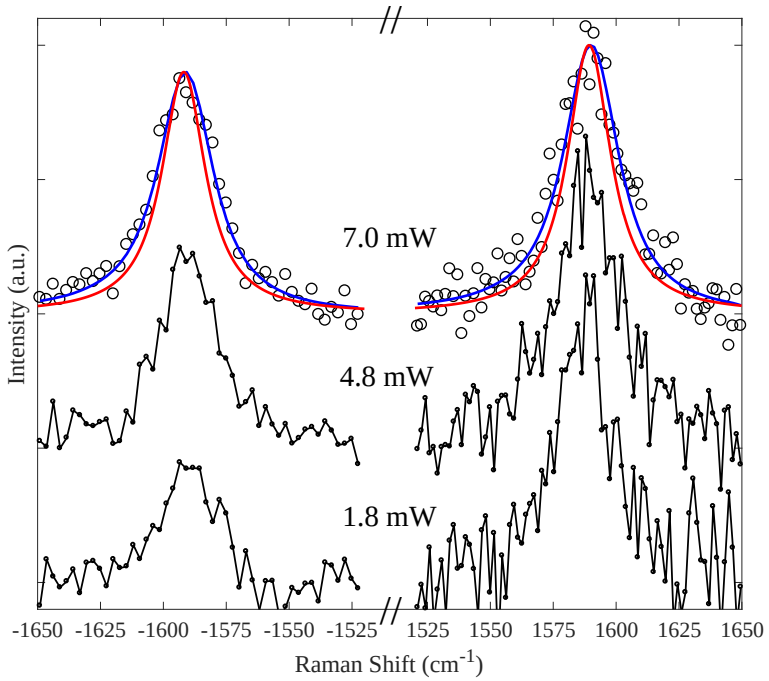

Figure 4.11: Background subtracted, AS and S G peak (in black, normalized to the corresponding Stokes maximum) measured as function of P_{L} in the range $\sim 1.8 \div 7.0$mW (corresponding to $T_{\mathrm{e}} \sim 2000 \div 2700$K). Three representative P_{L} values are shown. Best fits of the G peak (blue line), obtained as a convolution of a Lorentzian (red line) with the IRF are also reported for the largest P_{L} value.

cay pathway, which becomes progressively less efficient with increasing fluence. This non equilibrium PL recalls the grey body emission and can be in first approximation described by Planck's law [61, 62, 64, 67]:

$$I(\hbar\omega, T_e) = \mathcal{R}(\hbar\omega)\tau_{\mathrm{em}}\eta\frac{\hbar\omega^3}{2\pi^2c^2}\left(e^{\frac{\hbar\omega}{kT_e}} - 1\right)^{-1} \tag{4.4.17}$$

where η is the emissivity, defined as the dimensionless ratio of the thermal radiation of the material to the radiation from an ideal black surface at the same temperature as given by the Stefan-Boltzmann law [92]. τ_{em} is the emission time and $\mathcal{R}(\hbar\omega)$ is the frequency-dependent, dimensionless responsivity of our detection chain. Refs. [61,62,67] reported that, although Eq.4.4.17 does not perfectly reproduce the entire grey body emission, the good agreement on a ~ 0.5eV energy window is sufficient to extract T_{e}. By fitting the backgrounds of the Raman spectra with Eq.4.4.17 (solid

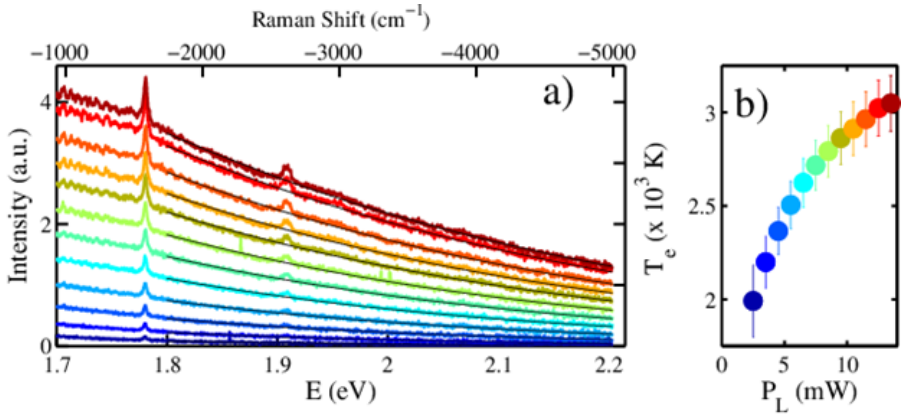

Figure 4.12: a) AS Raman spectra under ultrafast excitation for laser powers increasing along the arrow direction. The P_{L}-dependent background is fitted by thermal emission (Eq.4.4.17, black lines) resulting in T_{e} in the 1700-3100K range. b) T_{e} as a function of P_L. Error bars represent the 95% confidence bounds of the best fit.

lines in Fig.4.12a) we obtain T_{e} as a function of P_{L}. Fig.4.12b shows that T_{e} can reach up to 3100K under our pulsed excitation conditions.

An upper estimate for the lattice temperature, T_{l}, can be derived assuming a full thermalization of the optical energy between vibrational and electronic degrees of freedom, i.e. evaluating the local equilibrium temperature, T_{eq}, by a specific heat argument. Photoexcitation of SLG induces an excess of energy in the form of heat Q per unit area, that can be expressed as:

$$Q \sim \frac{P_{\mathrm{L}}}{RR}\frac{A}{\pi W^2} \tag{4.4.18}$$

where $A = 2.3\%$ is the SLG absorption, approximated to the undoped case [7], $W \sim 2.8\mu$m is the waist of focused beam and $RR = 40$ MHz is the repetition rate of the excitation laser. The induced T_{eq} can be derived based on two assumptions: (i) in our ps time scale the energy absorbed in the focal region does not diffuse laterally, (ii) the energy is equally distributed on each degree of freedom (electrons, optical and acoustic ph). Then, Q can be described as:

$$Q = \int_{RT}^{T_{\mathrm{eq}}} C(T)\, dT \tag{4.4.19}$$

where $C(T)$ is the SLG T-dependent specific heat. In the $300 - 700$K range, $C(T)$ can be described as [211]: $C(T) = aT + b$, where $a = 1.35 \cdot 10^{-6}$ J/(K^2·m^2)

and $b = 1.35 \cdot 10^{-4}$ J/(K·m^2). Therefore, considering Eqs.4.4.18 and 4.4.19, for $P_{\mathrm{L}} = P^{max} = 13.5$mW, we get $T_{\mathrm{eq}} \sim 680$K, well below the corresponding T_{e}, indicating an out-of-equilibrium condition ($T_{\mathrm{l}} < T_{\mathrm{eq}} < T_e$). Any contributions from the substrate and taking into account for the heat profile would contribute in reducing even further T_{l} estimation.

To understand the origin of such large FWHM(G) and FWHM(2D) in pulsed excitation, we first consider the excitation power dependence of the SLG AS Raman response in the $1.53 - 13.5$mW range (the lower bound is defined by the detection capability of our setup) with an higher spectrometer resolution (1.2 cm^{-1}), Fig.4.13.. This shows that the position of the G peak, Pos(G), is significantly blueshifted (as reported for graphite in Ref. [212]), while the position of the 2D peak, Pos(2D), is close to that measured under CW excitation, while both FWHM(G) and FWHM(2D) increase with P_{L}.

Notably, even the low resolution S data of the G band, collected in the range 1.8-7.0mW (a selection is shown in Fig.4.11), display a broadening ($(8 \pm 4)10^{-3}$ cm^{-1}K^{-1}) and upshift ($(2.8 \pm 1.4)10^{-3}$ cm^{-1}K^{-1}), which is compatible with that of the high resolution AS measurements (Fig. 4.11), $(7.4 \pm 0.5)10^{-3}$ cm^{-1}K^{-1} and $(3.2 \pm 0.2)10^{-3}$ cm^{-1}K^{-1}, respectively.

To verify that the observed peaks broadening is not limited by our IRF, we perform the same experiment on the Si substrate (4.15a), measuring its Raman spectrum as a function of P_L. The Raman spectrum of Silicon is characterized by an intense peak at ~ 520 cm^{-1} and a linewidth of ~ 3 cm^{-1}. Previous works [213] show that at increasing temperature the energy mode decreases and a significant variation of the relative intensity of S and AS components is observed; nevertheless, its dephasing time is expected to be constant with temperature.

Picosecond Raman measurements are carried out by varying P_L. Fig. 4.14.a shows the normalized Raman spectra after background subtraction. No changes of the peak frequency and linewidth are observed. These trends are confirmed by Fig. 4.14.b and 4.14.c , wherein FWHM and POS of the Si peak are obtained after deconvolution of the IRF (Fig.4.15a) and shown as a function of P_L. They both appear to be constant within the errorbars and we obtain the following weighted

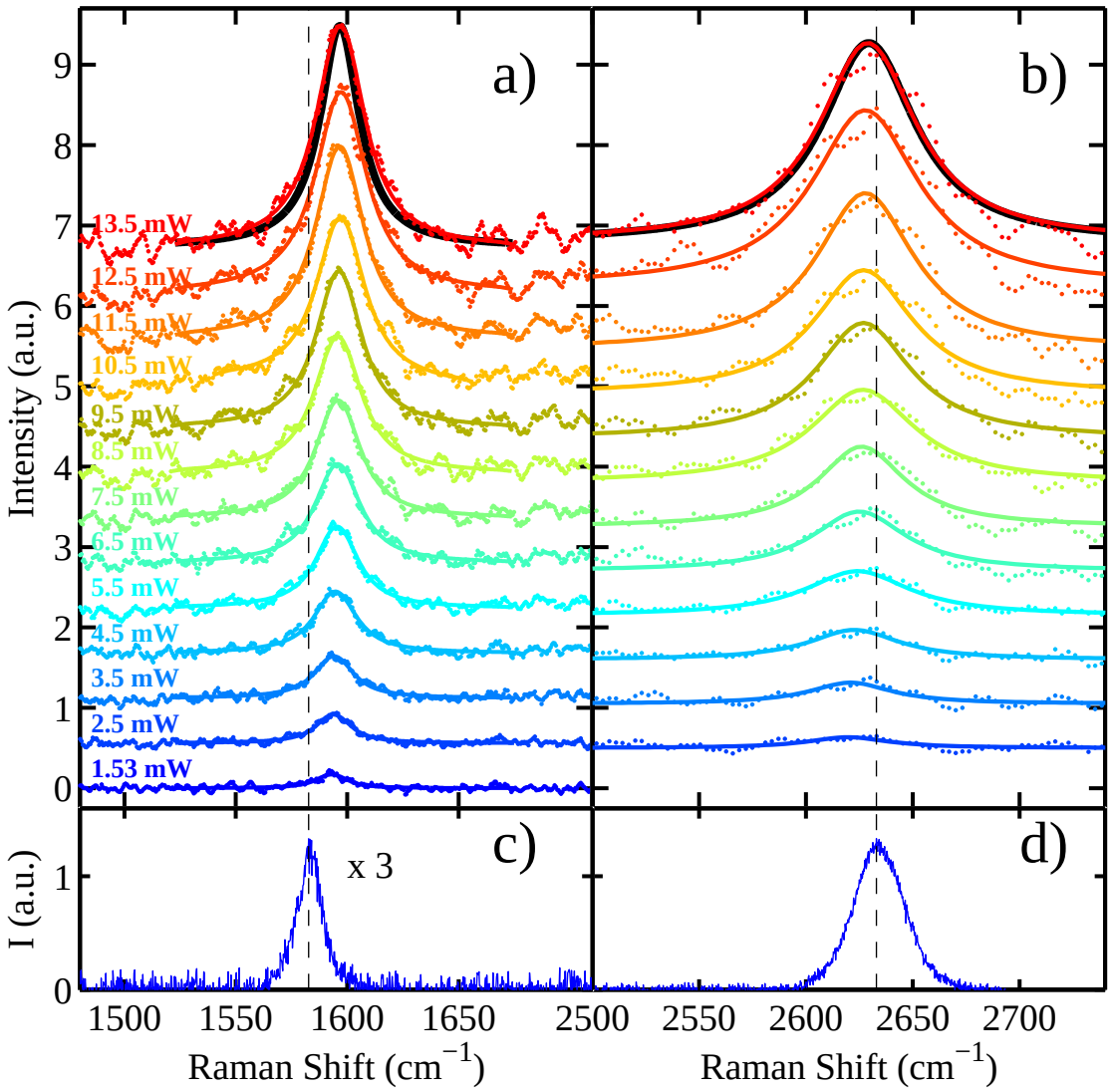

Figure 4.13: fRaman spectra at different laser power. (a) AS G and (b) 2D peak as function of P_L. (dots) Experimental data. (Lines) fitted Lorentzians convoluted with the spectral profile of the excitation pulse. The vertical dashed lines are the equilibrium, RT, Pos(G) and Pos(2D). (c) RT CW S G and (d) 2D peaks. The CW 2D is shifted by 5.4 cm^{-1} for comparison with the AS ps-Raman, see Methods. The relative calibration accuracy is $\sim$ 2cm^{-1}.

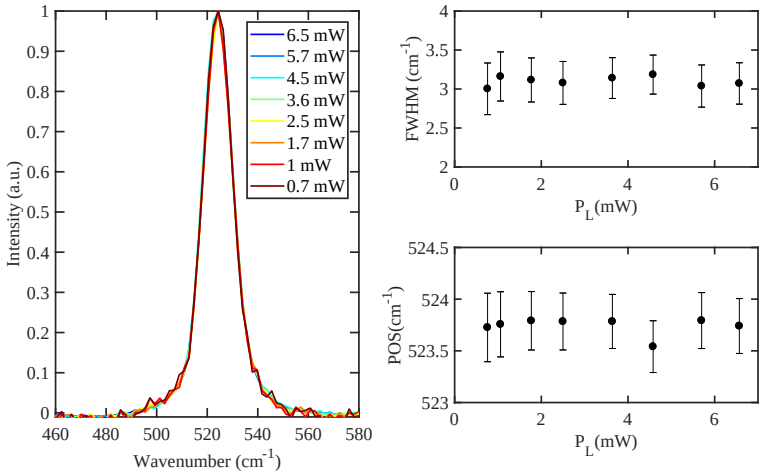

Figure 4.14: a) Normalized Si Raman spectra at different P_L. Both FWHM (b) and POS (c) are shown and they are constant in the P_L range.

values:

$$\text{POS} = (523.7 \pm 0.1)\text{cm}^{-1}$$

$$\text{FWHM} = (3.1 \pm 0.1)\text{cm}^{-1}$$

In particular, the FWHM of the Si optical phonon is independent of P_{L}, in contrast with the well-defined dependence on P_{L} observed in SLG, Fig.4.15b. We conclude that the observed broadening is only due to SLG.

In the case of CW excitation, the anti-Stokes/Stokes intensity ratio $A(G)_{AS}/A(G)_S$ is commonly used as a thermometer for the phonon bath, according to the following expression [214]:

$$T = \frac{\text{POS(G)}}{k_B ln\left[\frac{A(G)_{AS}}{A(G)_S}\right]} \tag{4.4.20}$$

This approximation is however grounded on key assumptions not valid in SLG case. Indeed, we note that phonons temperature estimates based on the AS/S intensity ratio [101,215] (corrected for the wavelength dependent grating reflectivity and CCD efficiency) are hampered in graphene by two concurring effects. First, SLG resonant response to any optical wavelength gives a non trivial wavelength dependent Raman excitation profile which modifies the Raman intensities with respect to the non-resonant case. Consequently, the AS/S ratio is no longer straightforwardly related to the thermal occupation [103]. Second, in graphene one S created phonon may be

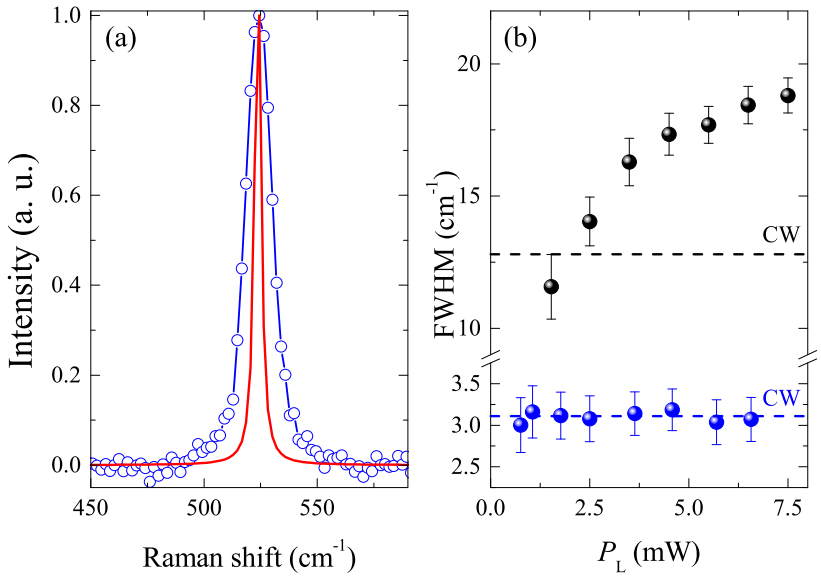

Figure 4.15: Raman response of Si for pulsed laser excitation.(a)Raman spectrum of Si measured for ultrafast laser excitation and 6.6mW average power. (blue line) Lorentzian fit. (red line) laser-bandwidth deconvoluted spectrum. (b) FWHM(Si) as a function of P_L (blue symbols) does not show any deviation from the CW FWHM(Si) (dashed blue line). FWHM(G) under the same excitation conditions (black symbols) deviates from the CW regime (dashed black line). Error bars represent the 95% confidence level of the best fit of the Si (panel a) and SLG (G band) peaks.

subsequently annihilated by a correlated AS event. Although a complete theoretical description for this phenomenon is still laking in graphene case, it has been proved in other carbon-based systems [216–219]. In practice, it results into an extra pumping in the AS side which does not allow to relate in the standard way AS/S ratio and phonon temperature via the thermal occupation factor [102]. Accordingly, the AS/S ratio approaching one at the largest excitation power in Fig.4.11 (black circles) does not necessary imply a large increase of the G phonon temperature.

Raman spectra, shown in Fig. 4.13, are fitted and Fig.4.16 plots Pos(2D), FWHM(2D), Pos(G), FWHM(G) as a function of T_e, estimated from the hot-PL. A comparison with CW measurements (633nm) at room temperature (RT) is also shown (blue diamonds).

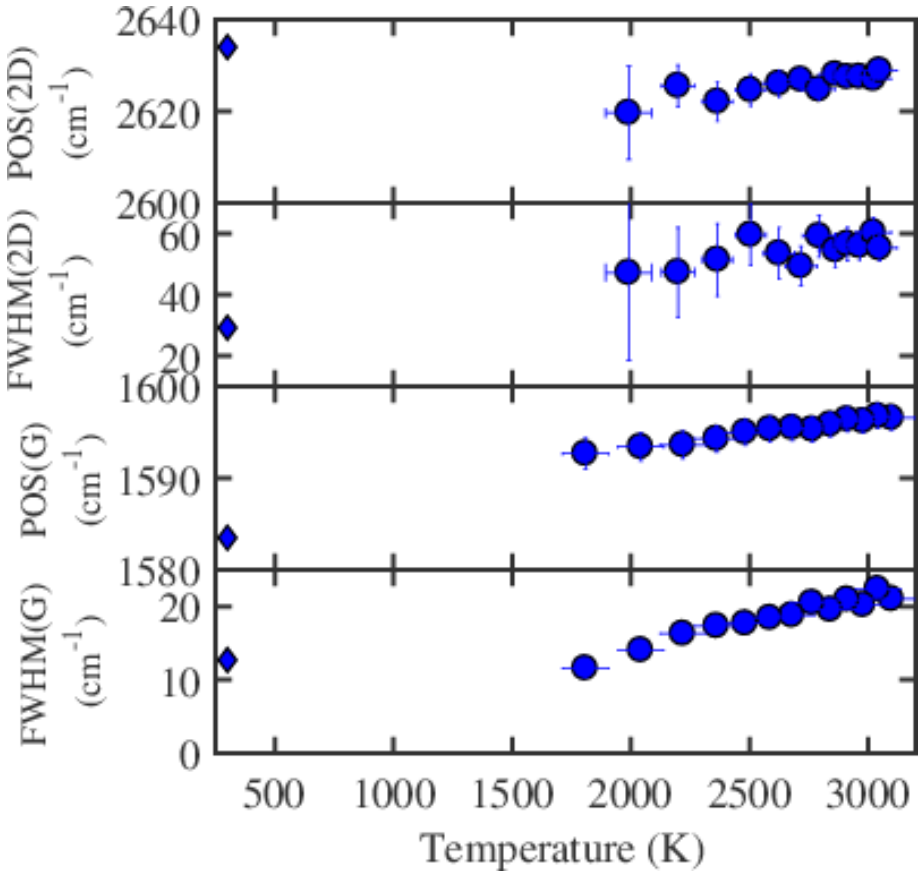

Figure 4.16: a) Pos(2D), b) FWHM(2D), c) Pos(G), d) FWHM(G) as a function of T_e for ps-excited Raman spectra. Error bars represent the 95% confidence level in the best fitting procedure. Solid diamonds represent the corresponding CW measurements.

4.5 Model

As pointed out by the hot-photoluminescence background, the ps-pulsed laser induces an high T_e in the system. Nevertheless, the lattice bath remains still cold. Indeed, it is confirmed by the estimation of T_{eq} and by the mismatch between our Raman data with the CW Raman spectroscopy obtained by heating SLG. Indeed at equilibrium the dominant anharmonicity determines an hardening of the phonon energy, that is in contrast with what we observe in Fig.4.16.

Therefore, in contrast with the previous scenario, the e-ph coupling becomes the dominant mechanism, while anharmonicity has to be considered as an additional effect. Nevertheless, EPC theory, as depicted in paragraph 3.1.1, is not able to

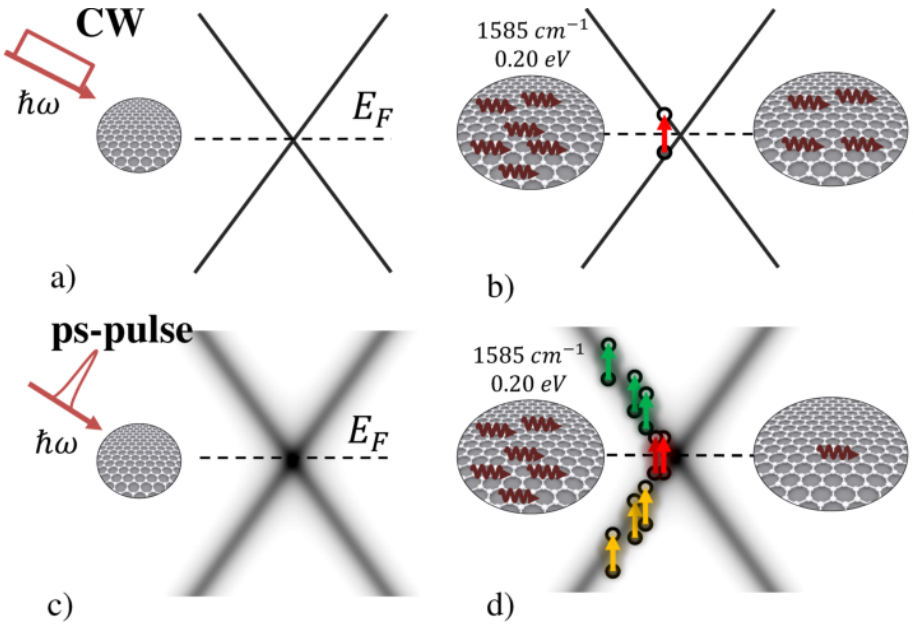

Figure 4.17: Effect of Dirac cone broadening on Raman process. (a) CW photo-excitation with mW power does not affect the Dirac cone. (b) Accordingly, e-h formation induced by e-ph scattering only occurs in presence of resonant phonon excitation. (c) Under ps excitation, with average P_{L} comparable to (a), the linear dispersion is smeared by the large $k_B T_{\mathrm{e}} \approx \hbar\omega_{\mathrm{G}} = 0.2$eV. (d) Consequently, e-h formation is enhanced by the increased phonon absorption cross section, due to new intraband processes.

completely describe our data yet. Actually, as shown in Fig. 4.3, it correctly describes an increase of POS(G) with T_e, but it would also predict a decrease of the FWHM(G), in striking contrast with our data (see Fig. 4.16).

Notably, we should consider the effect of the ps-pulsed laser on the electronic screening properties. Actually, referring to Eq. 4.1.11, the high photo-induced T_e could affect the electronic spectral function $M_s(z,\epsilon)$ and the Fermi energy E_F. Actually, our data suggest to have to firstly account for the effect of T_{e} on the energy broadening (γ_{e}) of the linear dispersion $M_s(z,\epsilon)$, introduced in Eq.4.1.13, along with the smearing of the Fermi function (see Fig. 4.17). $\gamma_{\mathrm{e}}(z,T_{\mathrm{e}})$ can be expressed, to a first approximation, as the sum of three terms [48]:

$$\gamma_{\mathrm{e}}(z,T_{\mathrm{e}}) = \gamma_{\mathrm{ee}}(T_{\mathrm{e}}) + \gamma_{\mathrm{ep}}(z) + \gamma_{def}(z) \tag{4.5.21}$$

where γ_{ee}, γ_{ep} and γ_{def} are the e-e, e-ph and defect contributions to γ_{e}. The only

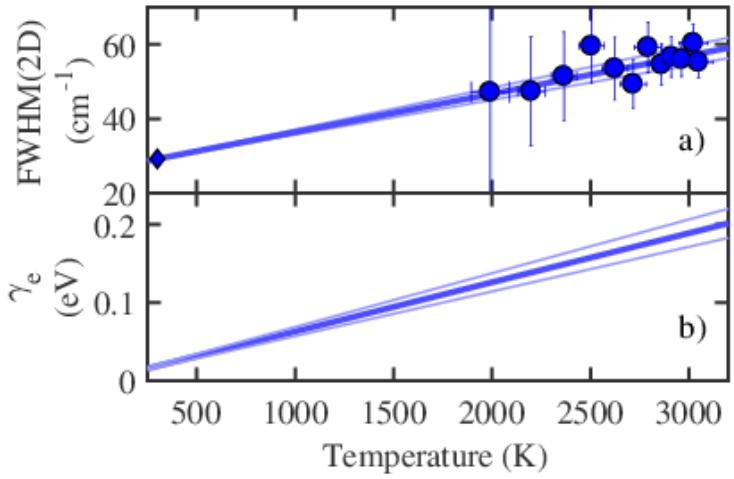

Figure 4.18: a) Pos(2D) as a function of T_e for ps-excited Raman spectra. Error bars represent the 95% confidence level in the best fitting procedure. Solid diamond represents the corresponding CW measurements. FWHM(2D) are used to determine the e-e contribution (γ_{ee}) to the Dirac cones broadening, shown in (b) (blue lines). From the fit of γ_{ee} in (b), we get $\frac{\alpha_e k_B}{hc} = 0.51\text{cm}^{-1}\text{K}^{-1}$ (thickest blue line). Values of $\frac{\alpha_e k_B}{hc} = 0.46, 0.55$ cm^{-1}K^{-1}, corresponding to 99% confidence boundaries, are also shown (thin light blue lines).

term that significantly depends on T_e is γ_{ee}, while the others depend on the energy z [9, 44, 46, 48, 181, 220].

The linear dependence of γ_{ee} on T_e [221] can be estimated from its impact on FWHM(2D). The variation of FWHM(2D) with respect to RT can be written as [116]:

$$\Delta\text{FWHM(2D)} = 4\sqrt{2^{2/3}-1}\frac{1}{2}\frac{\partial\text{POS(2D)}}{\partial(h\nu_{\text{laser}})}\gamma_{ee} \tag{4.5.22}$$

where $[\partial\text{POS(2D)}/\partial(h\nu_{\text{laser}})]/2 = \frac{1}{ch}v_{ph}/v_F \sim 100\text{cm}^{-1}$ eV^{-1} [12, 119], i.e. the ratio between the phonon and Fermi velocity, defined as the slope of the phononic (electronic) dispersion at the ph (e) momentum corresponding to a given excitation laser energy $h\nu_{\text{laser}}$ [12]. Since the double-resonant process responsible for the 2D peak involves the creation of e-h pairs at energy $\mp h\nu_{\text{laser}}/2$, the variation of FWHM(2D) allows us to estimate the variation of γ_e at $z = h\nu_{\text{laser}}/2 \simeq 0.8$eV. Then, γ_{ep} and γ_{def}, both proportional to z ($\gamma_{ep}, \gamma_{\text{def}} \propto z$), will give an additional constant contribution to FWHM(2D), but not to its variation with T_e. Our data support the

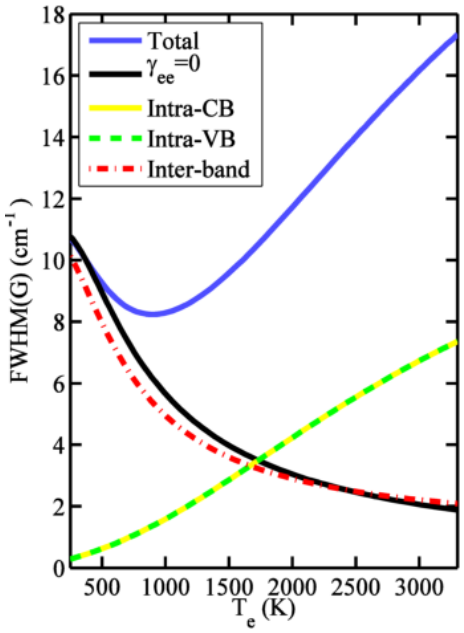

Figure 4.19: Corresponding contributions to FWHM(G) for the broadened inter-bands and intra-band processes for $\alpha_e k_B = 0.51$ cm^{-1}K^{-1}.

predicted [221] linear increase of $\gamma_{\rm ee}$ with $T_{\rm e}$, with a dimensionless experimental slope $\alpha_e \simeq 0.73$, Fig.4.18.b.

In order to compute FWHM(G) from Eq.4.1.11, we note that the terms $\gamma_{\rm ep}$ and $\gamma_{\rm def}$ are negligible at the relevant low energy $z = \hbar\omega_{\rm G}/2 \sim 0.1{\rm eV} \ll h\nu_{\rm laser}/2$. Hence $\gamma_{\rm e}(z, T_{\rm e}) \simeq \gamma_{\rm ee}(T_{\rm e})$.

The Dirac cone broadening can now be introduced by accounting for γ_e in the spectral function of Eq.4.1.13:

$$M_s(z) = \frac{1}{\pi}\frac{\gamma_{\rm e}/2}{(z + s\epsilon)^2 + (\gamma_{\rm e}/2)^2}, \quad s = \pm 1, \tag{4.5.23}$$

accordingly, all the processes where the energy difference $|s\epsilon(k) - s'\epsilon(k') + \hbar\omega_0|$ is less than $2\gamma_{\rm e}$ (which guarantees the overlap between the spectral functions of the quasiparticles) will now contribute in Eq.4.1.11. Amongst them, those transitions within the same (valence or conduction) band, as shown in Fig.4.17.d.

The broadened interband contributions still follow, approximately, Eq.4.1.14 (see Fig.4.19). However, the Dirac cone broadening gives additional channels for G phonon annihilation by carrier excitation. In particular, intra-band transitions within the Dirac cone are now progressively enabled for increasing $T_{\rm e}$, as sketched

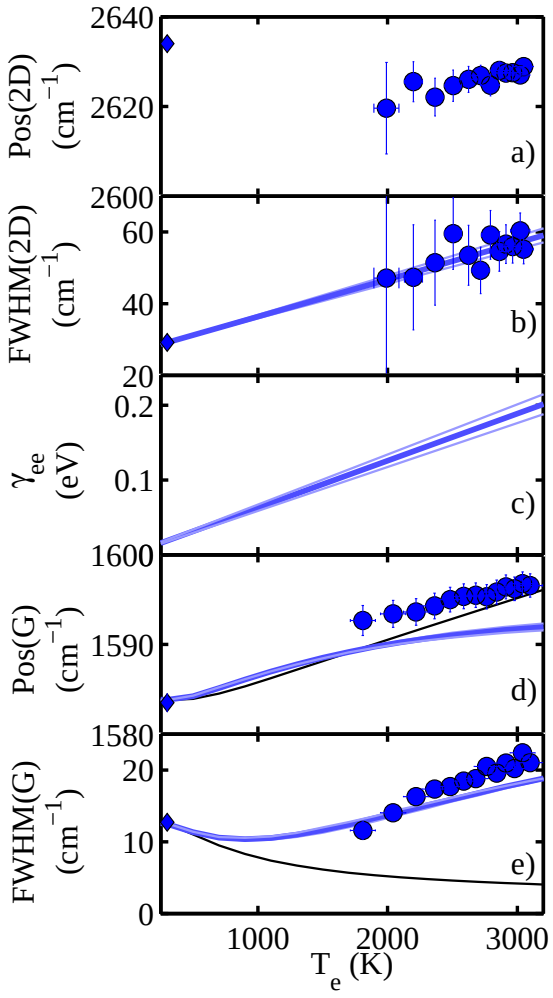

Figure 4.20: Comparison between theory and experiments. a) Pos(2D), b) FWHM(2D), d) Pos(G), e) FWHM(G) as a function of T_e for ps-excited Raman spectra. Error bars represent the 95% confidence level in the best fitting procedure. Solid diamonds in a,b,d,e represent the corresponding CW measurements. FWHM(2D) are used to determine the e-e contribution (γ_{ee}) to the Dirac cones broadening, shown in (c) (blue lines). Pos(G) and FWHM(G) are compared with theoretical predictions accounting for e-ph interaction in presence of electronic broadening (an additional RT anharmonic damping$\sim$2cm^{-1} [44] is included in the calculated FWHM(G)). Black lines are the theoretical predictions for $\gamma_{ee} = 0$eV, while blue lines take into account an electronic band broadening linearly proportional to T_e ($\gamma_{ee} = \alpha_e k_B T_e$). From the fit of γ_{ee} in (c), we get $\frac{\alpha_e k_B}{hc} = 0.51\text{cm}^{-1}\text{K}^{-1}$ (thickest blue line). Values of $\frac{\alpha_e k_B}{hc} = 0.46, 0.55$ cm^{-1}K^{-1}, corresponding to 99% confidence boundaries, are also shown (thin light blue lines).

in Fig.4.17.d. In Fig.4.19 the corresponding contributions to FWHM(G) are shown. Calculations in the weak-coupling limit [221] suggest that $\gamma_e(T_e)$ should be suppressed as $z \to 0$, due to phase-space restriction of the Dirac-cone dispersion. Our results, however, indicate that this effect should appear at an energy scale smaller than $\hbar\omega_G/2$, as the theory captures the main experimental trends, just based on a z-independent $\gamma_e(T_e)$.

Moreover, the good agreement between our model and data in Fig.4.20 reveal the minor role of the second possible effect to be considered, i.e. the Fermi level E_F. Indeed, the doping significantly decreases at high T_e, as shown in Fig.4.21. So, even if our samples are p doped at 250meV, E_F decreases down to 50 meV at the largest electronic temperatures explored in our study. This justifies the assumption of undoped graphene in our calculations, which simplify our numerical algorithms. Furthermore, a decrease of E_F with T_e would predict a POS(G) trend in striking contrast with our experimental results, as reported in Ref. [198].

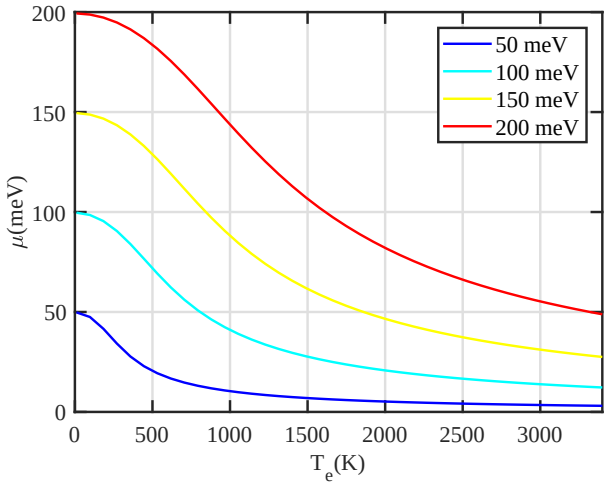

Figure 4.21: Temperature dependance of E_F. Adapted from Ref. [222].

Critically, the G peak broadening has a different origin from the previous models applied in the equilibrium case. This effect is observable only due to the possibility to isolate the EPC effects by impulsive photoexcitation. Indeed the absence of anharmonicity would imply a FWHM(G) decrease with temperature due to the e-ph mechanism [**?**, 9]. However, the Dirac cone broadening reverses this trend into a linewidth broadening above $T_e = 1000$K producing, in turn, a dephasing time

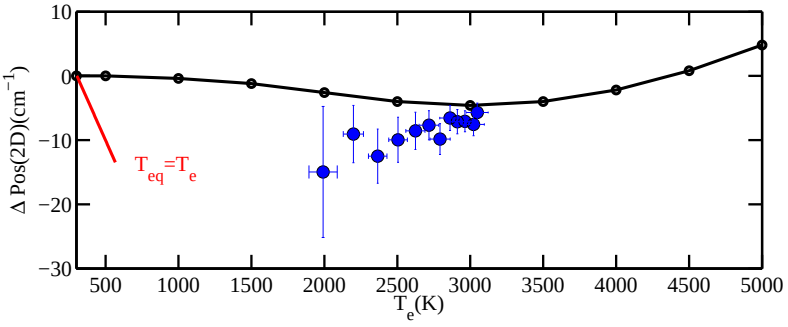

Figure 4.22: Temperature dependence of Pos(2D). Pos(2D), relative to the RT CW measurement, as a function of T_{e}. Black line: DFPT; Blue circles: experimental data with pulsed excitation. Red line: T-dependent CW measurement in thermal equilibrium ($T_{\mathrm{e}} = T_{\mathrm{l}} = T_{\mathrm{eq}}$) from Ref. [197]. The error bars represent the 95% of confidence level, as in Fig.4.20.

reduction, corresponding to the experimentally observed FWHM(G) increase. The blueshift of the G peak with temperature is captured by the standard e-ph interaction, beyond possible calibration accuracy. Importantly, the Dirac cone broadening does not significantly affect Pos(G).

An additional validation of the out-of-equilibrium model introduced to describe our experiment is given by the POS(2D) behaviour as a function T_e shown in Fig. 4.22 (blue circles). Notably, in order to describe this trend Prof. Mauri and Dr. Benfatto perform calculations within the Local Density Approximation in DFPT [223, 224]. We use the experimental lattice parameter 2.46Å [225] and plane waves (45Ry cutoff), within a norm-conserving pseudopotential approach [224]. The electronic levels are occupied with a finite fictitious T_{e} with a Fermi Dirac distribution, and we sample a Brillouin Zone with a 160x160x1 mesh. This does not take into account anharmonic effects, assuming $T_{\mathrm{l}} = 300$K. Fig.4.22 shows a weak $\Delta Pos(2D)(\sim 5\mathrm{cm}^{-1})$ in the range $T_{\mathrm{e}} = 300 - 3000$K. In equilibrium, $T_{\mathrm{l}} = T_{\mathrm{e}}$ would induce a non-negligible anharmonicity [197], which would lead to a Pos(2D) softening: $\Delta Pos(2D)/\Delta T_{\mathrm{eq}} = -0.05\mathrm{cm}^{-1}\ \mathrm{K}^{-1}$. The weak dependence $\Delta Pos(2D)(P_{\mathrm{L}})$ (blue circles in Fig.4.22) rules out a dominant anharmonicity contribution and, consequently, $T_{\mathrm{l}} = T_{\mathrm{e}}$. The minor disagreement with DFPT suggests a T_{l} slightly larger than RT, but definitely smaller than T_{eq}.

In this chapter [226] we show how to investigate the out-of equilibrium phonon behaviour in SLG by measuring the Raman spectrum with impulsive excitation. The choice of ps-pulses represents the best compromise between frequency resolution, required to observe the Raman spectra, and short pulse duration, necessary to create a significant population of hot carriers. It results that in order to understand SLG Raman spectrum under these strongly non-equilibrium conditions, it requires to revisit the standard low fluence picture. Our results shed light on a peculiar regime of non-equilibrium Raman response, whereby the e-ph interaction is enhanced due to the establishment of new relaxation channels. Moreover, we provide the experimental demonstration of a broadening of the electronic linear dispersion induced by the highly excited carriers.

Chapter 5

Conclusions

In this thesis, we present a novel approach for studying vibrational properties of low-dimensional materials as graphene. For this purpose, we use an erbium-doped fiber femtosecond oscillator combined with spectral compression achieved by group-velocity mismatched second-harmonic generation in periodically-poled nonlinear crystals. It allows an efficient generation of narrow-bandwidth picosecond pulses involved in Raman effect-based spectroscopic and imaging techniques.

By using two synchronized picosecond pulses and varying the time delay between them, we demonstrate how to suppress the intense NVRB and we measure the first evidence of CARS peak equivalent to the Raman spectrum in graphene. Indeed, lorentzian profiles, either peaks or dips, can be observed due to the interference between CARS and NVRB, although without facing the dispersive lineshape, typical of the (non-resonant) biological systems. Then, the overall spectral response is described in terms of a third-order diagrammatic description of the light-matter interaction. We demonstrate the resonant nature of the FWM in graphene due to the gapless Dirac cones is responsible for the anomalous dip lineshape. Accordingly, we show how to achieve high contrast and vibrational sensitivity for graphene imaging, introducing a promising characterization tool.

The same pulsed radiation has been used for investigating the out-of-equilibrium phonon behaviour in SLG by measuring the Raman spectrum with impulsive excitation. In this case, the choice of ps pulses represents the best trade-off between the frequency resolution, necessary to measure the Raman vibrational fingerprint, and

the short pulse duration to photoinduce an out-of-equilibrium condition. We observe a peculiar behaviour of the frequency and lifetime of both G and 2D phonons as function of the carriers temperature in the range 1700-3100 K, which is strongly suggestive of a smearing out of the Dirac cones. We rationalize such behaviour by accordingly revisiting the traditional theoretical modeling of the electron-phonon coupling in this highly excited transient scenario. Actually, the e-ph interaction is enhanced due to the establishment of new relaxation channels. Moreover, we are able to experimentally demonstrate the broadening of the electronic linear dispersion induced by the highly excited carriers.

Was this effect due to the coherent feature of the photoexcited phonons? Could it be due to the use of pulsed excitation in the experiment instead of the continuous-wave lasers involved in Spontaneous Raman spectroscopy? Could it be related to thermic effects? Can ultrashort light excitation photoinduce peculiar effects on graphene electronic and vibrational properties?

We are now able to answer the questions raised in the Motivation, about the decrease of SLG G phonon lifetime observed in coherent Raman measurements.

- Is this effect due to the coherent feature of the photoexcited phonons? No, the effect is observed also in Spontaneous Raman measurements, wherein the phonons are photoexcited incoherently. Indeed, as described in Chapter *Four*, the spectra show a broadening of FWHM(G), indicating a reduction of the phonon lifetime.

- Could it be related to thermic effects? Yes, actually the effect can be addressed to the out-of-equilibrium condition photoinduced in graphene, i.e. the establishment of an high electronic temperature largely exceeding the lattice one. This transient scenario enhances the effect of EPC in the SLG Raman spectra, without affecting the anharmonicity, determining a change in the Raman response.

- Could it be due to the use of pulsed excitation in the experiment instead of the continuous-wave lasers involved in Spontaneous Raman spectroscopy? Yes, the use of picosecond pulses allows us to establish the out-of-equilibrium

condition in SLG, while CW Spontaneous Raman is able to probe only phonon properties in thermodynamic equilibrium and it is not suitable for accessing such an effect. In particular, as explained in Chapter *Four*, ultrashort pulses can generate a smearing out of the Dirac cone, determining the opening of additional relaxation channels in the EPC response, responsible for the reduction of the G phonon lifetime.

In this work we analyse the details of the evolution in the graphene electronic distribution looking at a different point of view: the phonons counterpart. Moreover, we introduce a CARS vibrational imaging protocol with contrast equivalent to spontaneous Raman microscopy and signal level as large as those of the third-order non-linear response. Such a tool paves the way to ultrafast imaging, that can be obtained by substituting in the experiment our Si-CCD array with a faster point detector, e.g. a photomultiplier.

We believe that this thesis has witnessed how exploit picosecond pulses to explore out-of-equilibrium phonon behaviour will find interest in the scientific community, offering a new promising way to study other nanostructured systems for optoelectronic and photonic applications.

Bibliography

[1] K. S. Novoselov, D. Jiang, F. Schedin, T. J. Booth, V. V. Khotkevich, S. V. Morozov, and A. K. Geim. Two-dimensional atomic crystals. *Proceedings of the National Academy of Sciences*, 102(30):10451–10453, 2005.

[2] Andrea C. Ferrari, Francesco Bonaccorso, Vladimir Fal'ko, Konstantin S. Novoselov, Stephan Roche, Peter Bggild, Stefano Borini, Frank H. L. Koppens, Vincenzo Palermo, Nicola Pugno, Jos A. Garrido, Roman Sordan, Alberto Bianco, Laura Ballerini, Maurizio Prato, Elefterios Lidorikis, Jani Kivioja, Claudio Marinelli, Tapani Ryhnen, Alberto Morpurgo, Jonathan N. Coleman, Valeria Nicolosi, Luigi Colombo, Albert Fert, Mar Garcia-Hernandez, Adrian Bachtold, Grgory F. Schneider, Francisco Guinea, Cees Dekker, Matteo Barbone, Zhipei Sun, Costas Galiotis, Alexander N. Grigorenko, Gerasimos Konstantatos, Andras Kis, Mikhail Katsnelson, Lieven Vandersypen, Annick Loiseau, Vittorio Morandi, Daniel Neumaier, Emanuele Treossi, Vittorio Pellegrini, Marco Polini, Alessandro Tredicucci, Gareth M. Williams, Byung Hee Hong, Jong-Hyun Ahn, Jong Min Kim, Herbert Zirath, Bart J. van Wees, Herre van der Zant, Luigi Occhipinti, Andrea Di Matteo, Ian A. Kinloch, Thomas Seyller, Etienne Quesnel, Xinliang Feng, Ken Teo, Nalin Rupesinghe, Pertti Hakonen, Simon R. T. Neil, Quentin Tannock, Tomas Lfwander, and Jari Kinaret. Science and technology roadmap for graphene, related two-dimensional crystals, and hybrid systems. *Nanoscale*, 7:4598–4810, 2015.

[3] F. Bonaccorso, Z. Sun, T. Hasan, and A. C. Ferrari. Graphene photonics and optoelectronics. *Nat. Phot.*, 4:611–622, 2010.

[4] All-graphene-battery: bridging the gap between supercapacitors and lithium ion batteries. *Sci. Rep.*, 4, Jun 2014.

[5] Francesco Bonaccorso, Luigi Colombo, Guihua Yu, Meryl Stoller, Valentina Tozzini, Andrea C. Ferrari, Rodney S. Ruoff, and Vittorio Pellegrini. Graphene, related two-dimensional crystals, and hybrid systems for energy conversion and storage. *Science*, 347(6217), 2015.

[6] Jason Horng, Chi-Fan Chen, Baisong Geng, Caglar Girit, Yuanbo Zhang, Zhao Hao, Hans A. Bechtel, Michael Martin, Alex Zettl, Michael F. Crommie, Y. Ron Shen, and Feng Wang. Drude conductivity of dirac fermions in graphene. *Phys. Rev. B*, 83:165113, Apr 2011.

[7] R. R. Nair, P. Blake, A. N. Grigorenko, K. S. Novoselov, T. J. Booth, T. Stauber, N. M. R. Peres, and A. K. Geim. Fine structure constant defines visual transparency of graphene. *Science*, 320(5881):1308, 2008.

[8] A. H. Castro Neto, F. Guinea, N. M. R. Peres, K. S. Novoselov, and A. K. Geim. The electronic properties of graphene. *Rev. Mod. Phys.*, 81:109–162, Jan 2009.

[9] Simone Pisana, Michele Lazzeri, Cinzia Casiraghi, Kostya S. Novoselov, A. K. Geim, Andrea C. Ferrari, and Francesco Mauri. Breakdown of the adiabatic born-oppenheimer approximation in graphene. *Nat. Mater.*, 6:198–201, Mar 2007.

[10] Claude Weisbuch and Henri Benisty. Progress in the control of the lightmatter interaction in semiconductors. *Solid State Communications*, 135(9):627 – 637, 2005. Fundamental Optical and Quantum Effects in Condensed Matter.

[11] Christian Schneider, Mikhail M. Glazov, Tobias Korn, Sven Höfling, and Bernhard Urbaszek. Two-dimensional semiconductors in the regime of strong lightmatter coupling. *Nat. Commun.*, 9:2695, 2018.

[12] Andrea C. Ferrari and Denis M. Basko. Raman spectroscopy as a versatile tool for studying the properties of graphene. *Nat. Nanotech.*, 8:235–246, 2013.

[13] Andreas Volkmer, Lewis D. Book, and X. Sunney Xie. Time-resolved coherent anti-stokes raman scattering microscopy: Imaging based on raman free induction decay. *Applied Physics Letters*, 80(9):1505–1507, 2002.

[14] P. R. Wallace. The band theory of graphite. *Phys. Rev.*, 71:622–634, May 1947.

[15] H. W. Kroto, J. R. Heath, S. C. O'Brien, R. F. Curl, and R. E. Smalley. C60: Buckminsterfullerene. *Nature*, 318:162, Nov 1985.

[16] Sumio Iijima. Helical microtubules of graphitic carbon. *Nature*, 354:56, Nov 1991.

[17] K. S. Novoselov, A. K. Geim, S. V. Morozov, D. Jiang, Y. Zhang, S. V. Dubonos, I. V. Grigorieva, and A. A. Firsov. Electric field effect in atomically thin carbon films. *Science*, 306(5696):666–669, 2004.

[18] Wei Han, Roland K. Kawakami, Martin Gmitra, and Jaroslav Fabian. Graphene spintronics. *Nat. Nanotech.*, 9:794, 2014.

[19] Francesco Bonaccorso, Antonio Lombardo, Tawfique Hasan, Zhipei Sun, Luigi Colombo, and Andrea C. Ferrari. Production and processing of graphene and 2d crystals. *Mater. Today*, 15(12):564 – 589, 2012.

[20] Alexander E. Karu and Michael Beer. Pyrolytic formation of highly crystalline graphite films. *Journal of Applied Physics*, 37(5):2179–2181, 1966.

[21] Keun Soo Kim, Yue Zhao, Houk Jang, Sang Yoon Lee, Jong Min Kim, Kwang S. Kim, Jong-Hyun Ahn, Philip Kim, Jae-Young Choi, and Byung Hee Hong. Large-scale pattern growth of graphene films for stretchable transparent electrodes. *Nature*, 457:706, 2009.

[22] Alfonso Reina, Xiaoting Jia, John Ho, Daniel Nezich, Hyungbin Son, Vladimir Bulovic, Mildred S. Dresselhaus, and Jing Kong. Large area, few-layer graphene films on arbitrary substrates by chemical vapor deposition. *Nano Letters*, 9(1):30–35, 2009.

[23] Sukang Bae, Hyeongkeun Kim, Youngbin Lee, Xiangfan Xu, Jae-Sung Park, Yi Zheng, Jayakumar Balakrishnan, Tian Lei, Hye Ri Kim, Young Il Song, Young-Jin Kim, Kwang S. Kim, Barbaros Ozyilmaz, Jong-Hyun Ahn, Byung Hee Hong, and Sumio Iijima. Roll-to-roll production of 30-inch graphene films for transparent electrodes. *Nat. Nanotech.*, 5:574–578, Aug 2010.

[24] Dan Li, Marc B. Mller, Scott Gilje, Richard B. Kaner, and Gordon G. Wallace. Processable aqueous dispersions of graphene nanosheets. *Nat. Nanotech.*, 3:101, Jan 2008.

[25] Mustafa Lotya, Yenny Hernandez, Paul J. King, Ronan J. Smith, Valeria Nicolosi, Lisa S. Karlsson, Fiona M. Blighe, Sukanta De, Zhiming Wang, I. T. McGovern, Georg S. Duesberg, and Jonathan N. Coleman. Liquid phase production of graphene by exfoliation of graphite in surfactant/water solutions. *Journal of the American Chemical Society*, 131(10):3611–3620, 2009. PMID: 19227978.

[26] Mohammad Choucair, Pall Thordarson, and John A. Stride. Gram-scale production of graphene based on solvothermal synthesis and sonication. *Nat. Nanotech.*, 4:30, Dec 2008.

[27] Claire Berger, Zhimin Song, Tianbo Li, Xuebin Li, Asmerom Y. Ogbazghi, Rui Feng, Zhenting Dai, Alexei N. Marchenkov, Edward H. Conrad, Phillip N. First, and Walt A. de Heer. Ultrathin epitaxial graphite: 2d electron gas properties and a route toward graphene-based nanoelectronics. *J. Phys. Chem. B*, 108(52):19912–19916, 2004.

[28] S. Marchini, S. Gunther, and J. Wintterlin. Scanning tunneling microscopy of graphene on ru(0001). *Phys. Rev. B*, 76:075429, Aug 2007.

[29] B. Partoens and F. M. Peeters. From graphene to graphite: Electronic structure around the k point. *Phys. Rev. B*, 74:075404, Aug 2006.

[30] S. Reich, J. Maultzsch, C. Thomsen, and P. Ordejón. Tight-binding description of graphene. *Phys. Rev. B*, 66:035412, Jul 2002.

[31] R Saito, G Dresselhaus, and M S Dresselhaus. *Physical Properties of Carbon Nanotubes*. Published by Imperial Collage Press and distributed by World Scientific Publishing Co., 1998.

[32] D. C. Elias, R. V. Gorbachev, A. S. Mayorov, S. V. Morozov, A. A. Zhukov, P. Blake, I. V. Ponomarenko, L. A.and Grigorieva, K. S. Novoselov, F. Guinea, and A. K. Geim. Dirac cones reshaped by interaction effects in suspended graphene. *Nature Physics*, 7:701, 2011.

[33] C. Faugeras, S. Berciaud, P. Leszczynski, Y. Henni, K. Nogajewski, M. Orlita, T. Taniguchi, K. Watanabe, C. Forsythe, P. Kim, R. Jalil, A. K. Geim, D. M. Basko, and M. Potemski. Landau level spectroscopy of electron-electron interactions in graphene. *Phys. Rev. Lett.*, 114:126804, Mar 2015.

[34] Johannes Hofmann, Edwin Barnes, and S. Das Sarma. Why does graphene behave as a weakly interacting system? *Phys. Rev. Lett.*, 113:105502, Sep 2014.

[35] J. P. Hobson and W. A. Nierenberg. The statistics of a two-dimensional, hexagonal net. *Phys. Rev.*, 89:662–662, Feb 1953.

[36] Aaron Bostwick, Taisuke Ohta, Thomas Seyller, Karsten Horn, and Eli Rotenberg. Quasiparticle dynamics in graphene. *Nature Physics*, 3:36, 2006.

[37] L.M. Malard, M.A. Pimenta, G. Dresselhaus, and M.S. Dresselhaus. Raman spectroscopy in graphene. *Physics Reports*, 473(56):51 – 87, 2009.

[38] R. Nicklow, N. Wakabayashi, and H. G. Smith. Lattice dynamics of pyrolytic graphite. *Phys. Rev. B*, 5:4951–4962, Jun 1972.

[39] J. Maultzsch, S. Reich, C. Thomsen, H. Requardt, and P. Ordejón. Phonon dispersion in graphite. *Phys. Rev. Lett.*, 92:075501, Feb 2004.

[40] A. Grüneis, J. Serrano, A. Bosak, M. Lazzeri, S. L. Molodtsov, L. Wirtz, C. Attaccalite, M. Krisch, A. Rubio, F. Mauri, and T. Pichler. Phonon surface mapping of graphite: Disentangling quasi-degenerate phonon dispersions. *Phys. Rev. B*, 80:085423, Aug 2009.

[41] M. Mohr, J. Maultzsch, E. Dobardžić, S. Reich, I. Milošević, M. Damnjanović, A. Bosak, M. Krisch, and C. Thomsen. Phonon dispersion of graphite by inelastic x-ray scattering. *Phys. Rev. B*, 76:035439, Jul 2007.

[42] C. Oshima, T. Aizawa, R. Souda, Y. Ishizawa, and Y. Sumiyoshi. Surface phonon dispersion curves of graphite (0001) over the entire energy region. *Solid State Communications*, 65(12):1601 – 1604, 1988.

[43] H. Yanagisawa, T. Tanaka, Y. Ishida, M. Matsue, E. Rokuta, S. Otani, and C. Oshima. Analysis of phonons in graphene sheets by means of hreels measurement and ab initio calculation. *Surface and Interface Analysis*, 37(2):133–136.

[44] Nicola Bonini, Michele Lazzeri, Nicola Marzari, and Francesco Mauri. Phonon anharmonicities in graphite and graphene. *Phys. Rev. Lett.*, 99:176802, Oct 2007.

[45] S. Piscanec, M. Lazzeri, Francesco Mauri, A. C. Ferrari, and J. Robertson. Kohn anomalies and electron-phonon interactions in graphite. *Phys. Rev. Lett.*, 93:185503, Oct 2004.

[46] Jun Yan, Yuanbo Zhang, Philip Kim, and Aron Pinczuk. Electric field effect tuning of electron-phonon coupling in graphene. *Phys. Rev. Lett.*, 98:166802, Apr 2007.

[47] Michele Lazzeri, Claudio Attaccalite, Ludger Wirtz, and Francesco Mauri. Impact of the electron-electron correlation on phonon dispersion: Failure of lda and gga dft functionals in graphene and graphite. *Phys. Rev. B*, 78:081406, Aug 2008.

[48] Pedro Venezuela, Michele Lazzeri, and Francesco Mauri. Theory of double-resonant raman spectra in graphene: Intensity and line shape of defect-induced and two-phonon bands. *Phys. Rev. B*, 84:035433, Jul 2011.

[49] Aaron Bostwick, Taisuke Ohta, Jessica L. McChesney, Thomas Seyller, Karsten Horn, and Eli Rotenberg. Renormalization of graphene bands by

many-body interactions. *Solid State Communications*, 143(1):63 – 71, 2007. Exploring graphene.

[50] S. Piscanec, M. Lazzeri, Francesco Mauri, A. C. Ferrari, and J. Robertson. Kohn anomalies and electron-phonon interactions in graphite. *Phys. Rev. Lett.*, 93:185503, Oct 2004.

[51] Stephanie Reich and Christian Thomsen. Raman spectroscopy of graphite. *Philosophical Transactions of the Royal Society of London A: Mathematical, Physical and Engineering Sciences*, 362(1824):2271–2288, 2004.

[52] Eric Pop, Vikas Varshney, and Ajit K. Roy. Thermal properties of graphene: Fundamentals and applications. *MRS Bulletin*, 37(12):12731281, 2012.

[53] K V Zakharchenko, Annalisa Fasolino, J H Los, and M I Katsnelson. Melting of graphene: from two to one dimension. *Journal of Physics: Condensed Matter*, 23(20):202202, 2011.

[54] Kin Fai Mak, Long Ju, Feng Wang, and Tony F. Heinz. Optical spectroscopy of graphene: From the far infrared to the ultraviolet. *Solid State Communications*, 152(15):1341 – 1349, 2012. Exploring Graphene, Recent Research Advances.

[55] N. M. R. Peres. Colloquium: The transport properties of graphene: An introduction. *Rev. Mod. Phys.*, 82:2673–2700, Sep 2010.

[56] Z. Q. Li, E. A. Henriksen, Z. Jiang, Z. Hao, M. C. Martin, P. Kim, H. L. Stormer, and D. N. Basov. Dirac charge dynamics in graphene by infrared spectroscopy. *Nature Physics*, 4(1824):532–535, 2008.

[57] Feng Wang, Yuanbo Zhang, Chuanshan Tian, Caglar Girit, Alex Zettl, Michael Crommie, and Y. Ron Shen. Gate-variable optical transitions in graphene. *Science*, 320(5873):206–209, 2008.

[58] Kin Fai Mak, Jie Shan, and Tony F. Heinz. Seeing many-body effects in single- and few-layer graphene: Observation of two-dimensional saddle-point excitons. *Phys. Rev. Lett.*, 106:046401, Jan 2011.

[59] V. G. Kravets, A. N. Grigorenko, R. R. Nair, P. Blake, S. Anissimova, K. S. Novoselov, and A. K. Geim. Spectroscopic ellipsometry of graphene and an exciton-shifted van hove peak in absorption. *Phys. Rev. B*, 81:155413, Apr 2010.

[60] T. Stauber, N. M. R. Peres, and A. K. Geim. Optical conductivity of graphene in the visible region of the spectrum. *Phys. Rev. B*, 78:085432, Aug 2008.

[61] Chun Hung Lui, Kin Fai Mak, Jie Shan, and Tony F. Heinz. Ultrafast photoluminescence from graphene. *Phys. Rev. Lett.*, 105:127404, Sep 2010.

[62] Marcus Freitag, Hsin-Ying Chiu, Mathias Steiner, and Phaedon Avouris. Thermal infrared emission from biased graphene. *Nat. Nanotech.*, 5:497, 2010.

[63] Rainer J. Stöhr, Roman Kolesov, Jens Pflaum, and Jörg Wrachtrup. Fluorescence of laser-created electron-hole plasma in graphene. *Phys. Rev. B*, 82:121408, Sep 2010.

[64] Stéphane Berciaud, Melinda Y. Han, Kin Fai Mak, Louis E. Brus, Philip Kim, and Tony F. Heinz. Electron and optical phonon temperatures in electrically biased graphene. *Phys. Rev. Lett.*, 104:227401, Jun 2010.

[65] Tobias Kampfrath, Luca Perfetti, Florian Schapper, Christian Frischkorn, and Martin Wolf. Strongly coupled optical phonons in the ultrafast dynamics of the electronic energy and current relaxation in graphite. *Phys. Rev. Lett.*, 95:187403, Oct 2005.

[66] K. J. Tielrooij, J. C. W. Song, S. A. Jensen, A. Centeno, A. Pesquera, A. Zurutuza Elorza, M. Bonn, L. S. Levitov, and F. H. L. Koppens. Photoexcitation cascade and multiple hot-carrier generation in graphene. *Nature Physics*, 9:248, 2013.

[67] Young Duck Kim, Hakseong Kim, Yujin Cho, P. Kim, Ji Hoon Ryoo, Cheol-Hwan Park, Pilkwang Kim, Yong Seung Kim, Sunwoo Lee, Yilei Li, Seung-Nam Park, Yong Shim Yoo, Duhee Yoon, Duhee Yoon, Vincent E. Dorgan, Eric Pop, Tony F. Heinz, James Hone, Seung-Hyun Chun, Hyeonsik Cheong,

Sang Wook Lee, and Myung-Ho and Bae. Bright visible light emission from graphene. *Nat. Nanotech.*, 10:676, Jun 2015.

[68] F. H. L. Koppens, T. Mueller, Ph. Avouris, A. C. Ferrari, M. S. Vitiello, and M. Polini. Photodetectors based on graphene, other two-dimensional materials and hybrid systems. *Nat. Nanotech.*, 9:780, Oct 2014.

[69] Zhang H. Wang Y. Ni Z. Yan Y. Shen Z. X. Loh K. P. Bao, Q. and D. Y. Tang. Atomiclayer graphene as a saturable absorber for ultrafast pulsed lasers. *Advanced Functional Materials*, 19(19):3077–3083.

[70] G. Q. Xie, J. Ma, P. Lv, W. L. Gao, P. Yuan, L. J. Qian, H. H. Yu, H. J. Zhang, J. Y. Wang, and D. Y. Tang. Graphene saturable absorber for q-switching and mode locking at 2 μm wavelength. *Opt. Mater. Express*, 2(6):878–883, Jun 2012.

[71] Xiaomu Wang, He Tian, Mohammad Ali Mohammad, Cheng Li, Can Wu, Yi Yang, and Tian-Ling Ren. A spectrally tunable all-graphene-based flexible field-effect light-emitting device. *Nat. Commun.*, 36:7767, Jul 2015.

[72] Marc Currie, Joshua D. Caldwell, Francisco J. Bezares, Jeremy Robinson, Travis Anderson, Hayden Chun, and Marko Tadjer. Quantifying pulsed laser induced damage to graphene. *Applied Physics Letters*, 99(21):–, 2011.

[73] Harald O. Jeschke, Martin E. Garcia, and K. H. Bennemann. Theory for the ultrafast ablation of graphite films. *Phys. Rev. Lett.*, 87:015003, Jun 2001.

[74] A Beltaos, A Kovaevi, A Matkovi, U Ralevi, Dj Jovanovi, and B Jelenkovi. Damage effects on multi-layer graphene from femtosecond laser interaction. *Physica Scripta*, 2014(T162):014015, 2014.

[75] Adam Roberts, Daniel Cormode, Collin Reynolds, Ty Newhouse-Illige, Brian J. LeRoy, and Arvinder S. Sandhu. Response of graphene to femtosecond high-intensity laser irradiation. *Applied Physics Letters*, 99(5):–, 2011.

[76] S. Butscher, F. Milde, M. Hirtschulz, E. Mali, and A. Knorr. Hot electron relaxation and phonon dynamics in graphene. *Applied Physics Letters*, 91(20):203103, 2007.

[77] Wang-Kong Tse, E. H. Hwang, and S. Das Sarma. Ballistic hot electron transport in graphene. *Applied Physics Letters*, 93(2):023128, 2008.

[78] Kwangu Kang, Daner Abdula, David G. Cahill, and Moonsub Shim. Lifetimes of optical phonons in graphene and graphite by time-resolved incoherent anti-stokes raman scattering. *Phys. Rev. B*, 81:165405, Apr 2010.

[79] Raseong Kim, Vasili Perebeinos, and Phaedon Avouris. Relaxation of optically excited carriers in graphene. *Phys. Rev. B*, 84:075449, Aug 2011.

[80] M. Schütt, P. M. Ostrovsky, I. V. Gornyi, and A. D. Mirlin. Coulomb interaction in graphene: Relaxation rates and transport. *Phys. Rev. B*, 83:155441, Apr 2011.

[81] P. J. Hale, S. M. Hornett, J. Moger, D. W. Horsell, and E. Hendry. Hot phonon decay in supported and suspended exfoliated graphene. *Phys. Rev. B*, 83:121404, Mar 2011.

[82] Ermin Malic, Torben Winzer, Evgeny Bobkin, and Andreas Knorr. Microscopic theory of absorption and ultrafast many-particle kinetics in graphene. *Phys. Rev. B*, 84:205406, Nov 2011.

[83] B. Y. Sun, Y. Zhou, and M. W. Wu. Dynamics of photoexcited carriers in graphene. *Phys. Rev. B*, 85:125413, Mar 2012.

[84] T Winzer and E Malic. The impact of pump fluence on carrier relaxation dynamics in optically excited graphene. *Journal of Physics: Condensed Matter*, 25(5):054201, 2013.

[85] Andrea Tomadin, Daniele Brida, Giulio Cerullo, Andrea C. Ferrari, and Marco Polini. Nonequilibrium dynamics of photoexcited electrons in graphene: Collinear scattering, auger processes, and the impact of screening. *Phys. Rev. B*, 88:035430, Jul 2013.

[86] D. Brida, A. Tomadin, C. Manzoni, Y. J. Kim, A. Lombardo, S. Milana, R. R. Nair, K. S. Novoselov, A. C. Ferrari, G. Cerullo, and M. Polini. Ultrafast collinear scattering and carrier multiplication in graphene. *Nat. Commun.*, 4:1987, June 2013.

[87] Torben Winzer, Andreas Knorr, and Ermin Malic. Carrier multiplication in graphene. *Nano Letters*, 10(12):4839–4843, 2010. PMID: 21053963.

[88] Klaas-Jan Tielrooij, Niels C.H. Hesp, Alessandro Principi, Mark B. Lundeberg, Eva A.A. Pogna, Luca Banszerus, Zoltn Mics, Mathieu Massicotte, Peter Schmidt, Diana Davydovskaya, David G. Purdie, Ilya Goykhman, Giancarlo Soavi, Antonio Lombardo, Kenji Watanabe, Takashi Taniguchi, Mischa Bonn, Dmitry Turchinovich, Christoph Stampfer, Andrea C. Ferrari, Giulio Cerullo, Marco Polini, and Frank H.L. Koppens. Out-of-plane heat transfer in van der waals stacks through electronhyperbolic phonon coupling. *Nat. Nanotech.*, 13:41, Jan 2018.

[89] Takeshi Koyama, Yoshito Ito, Kazuma Yoshida, Masaharu Tsuji, Hiroki Ago, Hideo Kishida, and Arao Nakamura. Near-infrared photoluminescence in the femtosecond time region in monolayer graphene on sio2. *ACS Nano*, 7(3):2335–2343, 2013. PMID: 23461396.

[90] Zhengtang Luo, Patrick M. Vora, Eugene J. Mele, A. T. Charlie Johnson, and James M. Kikkawa. Photoluminescence and band gap modulation in graphene oxide. *Applied Physics Letters*, 94(11):111909, 2009.

[91] Wei-Tao Liu, S. W. Wu, P. J. Schuck, M. Salmeron, Y. R. Shen, and F. Wang. Nonlinear broadband photoluminescence of graphene induced by femtosecond laser irradiation. *Phys. Rev. B*, 82:081408, Aug 2010.

[92] Herbert B. Callen. *Thermodynamics and an Introduction to Thermostatistics*. John Wiley & Sons Inc, New York, 1985.

[93] C. V. Raman and K. S. Krishnan. A New Type of Secondary Radiation. *Nature*, 121:501–502, 1928.

[94] Norman B. Colthup, Lawrence H. Daly, and Stephen E. Wiberley. *Introduction to Infrared and Raman Spectroscopy*. Academic Press, 1990.

[95] A. Weber. *Raman Spectroscopy of Gases and Liquids*. Springer, Berlin, Heidelberg, 1979.

[96] Vitor H. Paschoal, Luiz F. O. Faria, and Mauro C. C. Ribeiro. Vibrational spectroscopy of ionic liquids. *Chemical Reviews*, 117(10):7053–7112, 2017. PMID: 28051847.

[97] John R. Ferraro. *Introductory Raman Spectroscopy*. Academic Press, 2002.

[98] P. Yu and M. Cardona. *Fundamentals of Semiconductors: Physics and Materials Properties*. Springer, 2010.

[99] S. Mukamel. *Principles of Nonlinear Optical Spectroscopy*. 1999.

[100] Kerson Huang. *Statistical Mechanics*. Wiley, 1987.

[101] A. G. Souza Filho, A. Jorio, J. H. Hafner, C. M. Lieber, R. Saito, M. A. Pimenta, G. Dresselhaus, and M. S. Dresselhaus. Electronic transition energy E_{ii} for an isolated (n, m) single-wall carbon nanotube obtained by anti-stokes/stokes resonant raman intensity ratio. *Phys. Rev. B*, 63:241404, Jun 2001.

[102] Carlos A. Parra-Murillo, Marcelo F. Santos, Carlos H. Monken, and Ado Jorio. Stokes–anti-stokes correlation in the inelastic scattering of light by matter and generalization of the bose-einstein population function. *Phys. Rev. B*, 93:125141, Mar 2016.

[103] Thomas Goldstein, Shao-Yu Chen, Jiayue Tong, Di Xiao, Ashwin Ramasubramaniam, and Jun Yan. Raman scattering and anomalous stokes–anti-stokes ratio in mote$_2$ atomic layers. *Scie. Rep.*, 6:28024, Jun 2016.

[104] Jan Smit. Theory of raman scattering in solids. *Phys. Rev. B*, 3:4330–4337, Jun 1971.

[105] S. Nakashima and H. Harima. *Raman Spectroscopy of Semiconductors*. American Cancer Society, 2006.

[106] F. Tuinstra and J. L. Koenig. Raman spectrum of graphite. *The Journal of Chemical Physics*, 53(3):1126–1130, 1970.

[107] A. C. Ferrari, J. C. Meyer, V. Scardaci, C. Casiraghi, M. Lazzeri, F. Mauri, S. Piscanec, D. Jiang, K. S. Novoselov, S. Roth, and A. K. Geim. Raman spectrum of graphene and graphene layers. *Phys. Rev. Lett.*, 97:187401, Oct 2006.

[108] D. Graf, F. Molitor, K. Ensslin, C. Stampfer, A. Jungen, C. Hierold, and L. Wirtz. Spatially resolved raman spectroscopy of single- and few-layer graphene. *Nano Letters*, 7(2):238–242, 2007. PMID: 17297984.

[109] Guillaume Froehlicher and Stéphane Berciaud. Raman spectroscopy of electrochemically gated graphene transistors: Geometrical capacitance, electron-phonon, electron-electron, and electron-defect scattering. *Phys. Rev. B*, 91:205413, May 2015.

[110] P. H. Tan, W. P. Han, W. J. Zhao, Z. H. Wu, K. Chang, H. Wang, Y. F. Wang, N. Bonini, N. Marzari, N. Pugno, G. Savini, and A. C. Lombardo, A. Ferrari. The shear mode of multilayer graphene. *Nat. Mater.*, 11:294–300, Apr 2012.

[111] Hui Wang, Yufang Wang, Xuewei Cao, Min Feng, and Guoxiang Lan. Vibrational properties of graphene and graphene layers. *Journal of Raman Spectroscopy*, 40(12):1791–1796, 2009.

[112] A. Gupta, G. Chen, P. Joshi, S. Tadigadapa, and Eklund. Raman scattering from high-frequency phonons in supported n-graphene layer films. *Nano Letters*, 6(12):2667–2673, 2006. PMID: 17163685.

[113] S. Das, A.and Pisana, B. Chakraborty, S. K. Piscanec, S.and Saha, U. V. Waghmare, K. S. Novoselov, H. R. Krishnamurthy, A. K. Geim, A. C. Ferrari, and A. K. Sood. Monitoring dopants by raman scattering in an electrochemically top-gated graphene transistor. *Nat. Nanotech.*, 3:210–215, 2008.

[114] C. Casiraghi, A. Hartschuh, H. Qian, S. Piscanec, C. Georgi, A. Fasoli, K. S. Novoselov, D. M. Basko, and A. C. Ferrari. Raman spectroscopy of graphene edges. *Nano Letters*, 9(4):1433–1441, 2009. PMID: 19290608.

[115] A. C. Ferrari and J. Robertson. Interpretation of raman spectra of disordered and amorphous carbon. *Phys. Rev. B*, 61:14095–14107, May 2000.

[116] D. M. Basko. Theory of resonant multiphonon raman scattering in graphene. *Phys. Rev. B*, 78:125418, Sep 2008.

[117] Stphane Berciaud, Xianglong Li, Han Htoon, Louis E. Brus, Stephen K. Doorn, and Tony F. Heinz. Intrinsic lineshape of the raman 2d-mode in free-standing graphene monolayers. *Nano Letters*, 13:35173523, 2013.

[118] L. G. Cançado, A. Reina, J. Kong, and M. S. Dresselhaus. Geometrical approach for the study of $G^{'}$ band in the raman spectrum of monolayer graphene, bilayer graphene, and bulk graphite. *Phys. Rev. B*, 77:245408, Jun 2008.

[119] R.P. Vidano, D.B. Fischbach, L.J. Willis, and T.M. Loehr. Observation of raman band shifting with excitation wavelength for carbons and graphites. *Solid State Commun.*, 39(2):341 – 344, 1981.

[120] J.A. Wilson and A.D. Yoffe. The transition metal dichalcogenides discussion and interpretation of the observed optical, electrical and structural properties. *Advances in Physics*, 18(73):193–335, 1969.

[121] Kin Fai Mak and Jie Shan. Photonics and optoelectronics of 2d semiconductor transition metal dichalcogenides. *Nature Photonics*, 10:216, 2016.

[122] Kin Fai Mak, Changgu Lee, James Hone, Jie Shan, and Tony F. Heinz. Atomically thin mos_2: A new direct-gap semiconductor. *Phys. Rev. Lett.*, 105:136805, Sep 2010.

[123] Xiaodong Xu, Wang Yao, Di Xiao, and Tony F. Heinz. Spin and pseudospins in layered transition metal dichalcogenides. *Nature Physics*, 10:216, 2014.

[124] Guillaume Froehlicher. *Optical spectroscopy of two-dimensional materials: graphene, transition metal dichalcogenides and van derWaals heterostructures*. PhD Thesis, Universit de Strasbourg, 2016.

[125] Wenjing Zhang, Chih-Piao Chuu, Jing-Kai Huang, Chang-Hsiao Chen, Meng-Lin Tsai, Yung-Huang Chang, Chi-Tea Liang, Yu-Ze Chen, Yu-Lun Chueh, Jr-Hau He, Mei-Yin Chou, and Lain-Jong Li. Ultrahigh-gain photodetectors based on atomically thin graphene-mos_2 heterostructures. *Scie. Rep.*, 4:3826, Jan 2014.

[126] A. K. Geim and I. V. Grigorieva. Van der waals heterostructures. *Nature*, 499:419, 2013.

[127] K. S. Novoselov, A. Mishchenko, A. Carvalho, and A. H. Castro Neto. 2d materials and van der waals heterostructures. *Science*, 353(6298), 2016.

[128] Xiaoping Hong, Jonghwan Kim, Su-Fei Shi, Yu Zhang, Yinghui Tongay Sefaattin Jin, Chenhao Sun, Junqiao Wu, Yanfeng Zhang, and Feng Wang. Ultrafast charge transfer in atomically thin mos_2/ws_2 heterostructures. *Nat. Nanotech.*, 9:682, Aug 2014.

[129] M. Massicotte, P. Schmidt, F. Vialla, K. G. Schädler, A. Reserbat-Plantey, K. Watanabe, T. Taniguchi, K. J. Tielrooij, and F. H. L. Koppens. Picosecond photoresponse in van der waals heterostructures. *Nat. Nano.*, 11:42, 2015.

[130] Guillaume Froehlicher, Etienne Lorchat, and Stéphane Berciaud. Charge versus energy transfer in atomically thin graphene-transition metal dichalcogenide van der waals heterostructures. *Phys. Rev. X*, 8:011007, Jan 2018.

[131] Dario Polli, Vikas Kumar, Carlo M. Valensise, Marco Marangoni, and Giulio Cerullo. Broadband coherent raman scattering microscopy. *Laser & Photonics Reviews*, 12(9):1800020, 2018.

[132] Francesco Saltarelli, Vikas Kumar, Daniele Viola, Francesco Crisafi, Fabrizio Preda, Giulio Cerullo, and Dario Polli. Broadband stimulated raman scatter-

ing spectroscopy by a photonic time stretcher. *Opt. Express*, 24(19):21264–21275, Sep 2016.

[133] Francesco Crisafi, Vikas Kumar, Tullio Scopigno, Marco Marangoni, Giulio Cerullo, and Dario Polli. In-line balanced detection stimulated raman scattering microscopy. *Scientific Reports*, 7:10745, 2017.

[134] Aurelio Oriana, Julien Réhault, Fabrizio Preda, Dario Polli, and Giulio Cerullo. Scanning fourier transform spectrometer in the visible range based on birefringent wedges. *J. Opt. Soc. Am. A*, 33(7):1415–1420, Jul 2016.

[135] Charles H. Camp Jr and Marcus T. Cicerone. Chemically sensitive bioimaging with coherent raman scattering. *Nat. Photon.*, 9:295–305, 2015.

[136] Luis G. Rodriguez, Stephen J. Lockett, and Gary R. Holtom. Coherent anti-stokes raman scattering microscopy: A biological review. *Cytometry Part A*, 69A(8):779–791.

[137] Francesco Crisafi, Vikas Kumar, Antonio Perri, Marco Marangoni, Giulio Cerullo, and Dario Polli. Multimodal nonlinear microscope based on a compact fiber-format laser source. *Spectrochimica Acta Part A: Molecular and Biomolecular Spectroscopy*, 188:135 – 140, 2018.

[138] Jordan Brocious and Eric O. Potma. Lighting up micro-structured materials with four-wave mixing microscopy. *Materials Today*, 16(9):344 – 350, 2013.

[139] D. Popa, D. Viola, G. Soavi, B. Fu, L. Lombardi, S. Hodge, D. Polli, T. Scopigno, G. Cerullo, and A. C. Ferrari. Graphene synchronised all-fiber laser for coherent raman spectroscopy. In *2017 European Conference on Lasers and Electro-Optics and European Quantum Electronics Conference*, page EI_{P3}. Optical Society of America, 2017.

[140] Lucas Lafet, Alisson R. Cadore, Thiago G. Mendes-de Sa, Kenji Watanabe, Takashi Taniguchi, Leonardo C. Campos, Ado Jorio, and Leandro M. Malard. Anomalous nonlinear optical response of graphene near phonon resonances. *Nano Letters*, 17(6):3447–3451, 2017. PMID: 28541053.

[141] U. Fano. Effects of configuration interaction on intensities and phase shifts. *Phys. Rev.*, 124:1866–1878, Dec 1961.

[142] R. Yuste. Fluorescence microscopy today. *Nature Methods*, 2:902–904, 2005.

[143] T. Wilson. Resolution and optical sectioning in the confocal microscope. *Journal of Microscopy*, 244(2):113–121, 2011.

[144] Michiel Mller and Andreas Zumbusch. Coherent anti-stokes raman scattering microscopy. *ChemPhysChem*, 8(15):2156–2170, 2007.

[145] R. W. Boyd. *Nonlinear Optics*. Academic Press, 2008.

[146] E. O. Potma and S. Mukamel. *Theory of Coherent Raman Scattering*. in Coherent Raman Scattering Microscopy, J. X. Cheng and X. S. Xie (Eds.), CRC Press, 2013.

[147] G.L. Eesley. *Coherent Raman Spectroscopy*. Pergamon Press, 1981.

[148] Vikas Kumar, Nicola Coluccelli, Marco Cassinerio, Michele Celebrano, Abigail Nunn, Massimo Levrero, Tullio Scopigno, Giulio Cerullo, and Marco Marangoni. Low-noise, vibrational phase-sensitive chemical imaging by balanced detection rike. *Journal of Raman Spectroscopy*, 46(1):109–116.

[149] Meng Cui, Brandon R. Bachler, and Jennifer P. Ogilvie. Comparing coherent and spontaneous raman scattering under biological imaging conditions. *Opt. Lett.*, 34(6):773–775, Mar 2009.

[150] Y. R. Shen. *Nonlinear Optics*. Wiley-Interscience, 2002.

[151] C. Thomson, R. Leburn and D. Reid (Eds.). *Ultrafast Nonlinear Optics*. Springer, 2013.

[152] G. Agrawal. *Nonlinear Fiber Optics*. Academic Press, 2012.

[153] R. F. Begley, A. B. Harvey, and R. L. Byer. Coherent anti-stokes raman spectroscopy. *Applied Physics Letters*, 25(7), 1974.

[154] Andreas Zumbusch, Gary R. Holtom, and X. Sunney Xie. Three-dimensional vibrational imaging by coherent anti-stokes raman scattering. *Phys. Rev. Lett.*, 82:4142–4145, May 1999.

[155] Christoph A. Marx, Upendra Harbola, and Shaul Mukamel. Nonlinear optical spectroscopy of single, few, and many molecules: Nonequilibrium green's function qed approach. *Phys. Rev. A*, 77:022110, Feb 2008.

[156] J. B. Khurgin. Graphenea rather ordinary nonlinear optical material. *Applied Physics Letters*, 104(16):–, 2014.

[157] E. Hendry, P. J. Hale, J. Moger, A. K. Savchenko, and S. A. Mikhailov. Coherent nonlinear optical response of graphene. *Phys. Rev. Lett.*, 105:097401, Aug 2010.

[158] Giancarlo Soavi, Gang Wang, Habib Rostami, David G. Purdie, Domenico De Fazio, Teng Ma, Birong Luo, Junjia Wang, Anna K. Ott, Duhee Yoon, Sean A. Bourelle, Jakob E Muench, Ilya Goykhman, Stefano Dal Conte, Michele Celebrano, Andrea Tomadin, Marco Polini, Giulio Cerullo, and Andrea C Ferrari. Broadband, electrically tunable third-harmonic generation in graphene. *Nat. Nanotech.*, (15), 2018.

[159] Han Zhang, Stéphane Virally, Qiaoliang Bao, Loh Kian Ping, Serge Massar, Nicolas Godbout, and Pascal Kockaert. Z-scan measurement of the nonlinear refractive index of graphene. *Opt. Lett.*, 37(11):1856–1858, Jun 2012.

[160] Sung-Young Hong, Jerry I. Dadap, Nicholas Petrone, Po-Chun Yeh, James Hone, and Richard M. Osgood. Optical third-harmonic generation in graphene. *Phys. Rev. X*, 3:021014, Jun 2013.

[161] Tao Jiang, Di Huang, Jinluo Cheng, Xiaodong Fan, Zhihong Zhang, Yuwei Shan, Yangfan Yi, Yunyun Dai, Lei Shi, Kaihui Liu, Changgan Zeng, Jian Zi, J. E. Sipe, Yuen-Ron Shen, Wei-Tao Liu, and Shiwei Wu. Gate-tunable third-order nonlinear optical response of massless dirac fermions in graphene. *Nat. Phot.*, 12:430–436, 2018.

[162] M. D. Duncan, J. Reintjes, and T. J. Manuccia. Scanning coherent anti-stokes raman microscope. *Opt. Lett.*, 7(8):350–352, Aug 1982.

[163] Ji-Xin Cheng, Andreas Volkmer, and X. Sunney Xie. Theoretical and experimental characterization of coherent anti-stokes raman scattering microscopy. *J. Opt. Soc. Am. B*, 19(6):1363–1375, Jun 2002.

[164] X. Sunney Xie, Ji-Xin Cheng, and Eric O. Potma. *Coherent Anti-Stokes Raman Scattering Microscopy.* in Handbook of Biological Confocal Microscopy, James Pawley (Ed), p 595-606, Springer Science, New York, 2006.

[165] Conor L. Evans and X. Sunney Xie. Coherent anti-stokes raman scattering microscopy: Chemical imaging for biology and medicine. *Annual Review of Analytical Chemistry*, 1(1):883–909, 2008. PMID: 20636101.

[166] Ji-Xin Cheng and X. Sunney Xie. Coherent anti-stokes raman scattering microscopy: instrumentation, theory, and applications. *The Journal of Physical Chemistry B*, 108:827–840, 2004.

[167] Giulio Cerullo and Sandro De Silvestri. Ultrafast optical parametric amplifiers. *Review of Scientific Instruments*, 74(1):1–18, 2003.

[168] M. A. Marangoni, D. Brida, M Quintavalle, G. Cirmi, F. M. Pigozzo, C. Manzoni, F Baronio, A. D. Capobianco, and G. Cerullo. Narrow-bandwidth picosecond pulses by spectral compression of femtosecond pulses in second-order nonlinear crystals. *Opt. Express*, 15(14):8884–8891, Jul 2007.

[169] M.M. Fejer, G.A. Magel, Dieter H. Jundt, and R.L. Byer. Quasi-phase-matched second harmonic generation: tuning and tolerances. *Quantum Electronics, IEEE Journal of*, 28(11):2631–2654, Nov 1992.

[170] Grant R. Fowles. *Introduction to Modern Optics.* Dover Publications, 1989.

[171] Michael W. Davidson and Mortimer Abramowitz. *Optical Microscopy.* Oxford University Press, 2008.

[172] Nathan S. Claxton, Thomas J. Fellers, and Michael W. Davidson. *Laser Scanning Confocal Microscopy*. 2008.

[173] C. Casiraghi, A. Hartschuh, E. Lidorikis, H. Qian, H. Harutyunyan, T. Gokus, K. S. Novoselov, and A. C. Ferrari. Rayleigh imaging of graphene and graphene layers. *Nano Letters*, 7(9):2711–2717, 2007.

[174] P. E. Gaskell, H. S. Skulason, C. Rodenchuk, and T. Szkopek. Counting graphene layers on glass via optical reflection microscopy. *Applied Physics Letters*, 94(14):–, 2009.

[175] Z. H. Ni, H. M. Wang, J. Kasim, H. M. Fan, T. Yu, Y. H. Wu, Y. P. Feng, and Z. X. Shen. Graphene thickness determination using reflection and contrast spectroscopy. *Nano Letters*, 7(9):2758–2763, 2007. PMID: 17655269.

[176] Arnaud (Ed.) Zoubir. *Raman Imaging, Techniques and Applications*. Springer-Verlag Berlin Heidelberg, 2012.

[177] Xuesong Li, Weiwei Cai, Jinho An, Seyoung Kim, Junghyo Nah, Dongxing Yang, Richard Piner, Aruna Velamakanni, Inhwa Jung, Emanuel Tutuc, Sanjay K. Banerjee, Luigi Colombo, and Rodney S. Ruoff. Large-area synthesis of high-quality and uniform graphene films on copper foils. *Science*, 324(5932):1312–1314, 2009.

[178] A. A. Lagatsky, Z. Sun, T. S. Kulmala, R. S. Sundaram, S. Milana, F. Torrisi, O. L. Antipov, Y. Lee, J. H. Ahn, C. T. A. Brown, W. Sibbett, and A. C. Ferrari. 2m solid-state laser mode-locked by single-layer graphene. *Appl. Phys. Lett.*, 102(1):013113, 2013.

[179] L. G. Cançado, A. Jorio, E. H. Martins Ferreira, F. Stavale, C. A. Achete, R. B. Capaz, M. V. O. Moutinho, A. Lombardo, T. S. Kulmala, and A. C. Ferrari. Quantifying defects in graphene via raman spectroscopy at different excitation energies. *Nano Lett.*, 11(8):3190–3196, 2011.

[180] A. C. Ferrari and J. Robertson. Interpretation of raman spectra of disordered and amorphous carbon. *Phys. Rev. B*, 61:14095–14107, May 2000.

[181] D. M. Basko, S. Piscanec, and A. C. Ferrari. Electron-electron interactions and doping dependence of the two-phonon raman intensity in graphene. *Phys. Rev. B*, 80:165413, Oct 2009.

[182] A. Das, S. Pisana, B. Chakraborty, S. Piscanec, S. K. Saha, U. V. Waghmare, K. S. Novoselov, H. R. Krishnamurthy, A. K. Geim, A. C. Ferrari, and A. K. Sood. Monitoring dopants by raman scattering in an electrochemically top-gated graphene transistor. *Nat. Nanotech.*, 3:210–215, Apr 2008.

[183] Andreas Volkmer, Lewis D. Book, and X. Sunney Xie. Time-resolved coherent anti-stokes raman scattering microscopy: Imaging based on raman free induction decay. *Appl. Phys. Lett.*, 80(9):1505–1507, 2002.

[184] Francois M. Kamga and Mark G. Sceats. Pulse-sequenced coherent anti-stokes raman scattering spectroscopy: a method for suppression of the nonresonant background. *Opt. Lett.*, 5(3):126–128, Mar 1980.

[185] Dmitrii A. Sidorov-Biryukov, Evgenii E. Serebryannikov, and Aleksei M. Zheltikov. Time-resolved coherent anti-stokes raman scattering with a femtosecond soliton output of a photonic-crystal fiber. *Opt. Lett.*, 31(15):2323–2325, Aug 2006.

[186] Dmitry Pestov, Robert K. Murawski, Gombojav O. Ariunbold, Xi Wang, Miaochan Zhi, Alexei V. Sokolov, Vladimir A. Sautenkov, Yuri V. Rostovtsev, Arthur Dogariu, Yu Huang, and Marlan O. Scully. Optimizing the laser-pulse configuration for coherent raman spectroscopy. *Science*, 316(5822):265–268, 2007.

[187] Romedi Selm, Martin Winterhalder, Andreas Zumbusch, Günther Krauss, Tobias Hanke, Alexander Sell, and Alfred Leitenstorfer. Ultrabroadband background-free coherent anti-stokes raman scattering microscopy based on a compact er:fiber laser system. *Opt. Lett.*, 35(19):3282–3284, Oct 2010.

[188] Vikas Kumar, R. Osellame, R. Ramponi, G. Cerullo, and M. Marangoni. Background-free broadband cars spectroscopy from a 1-mhz ytterbium laser. *Opt. Express*, 19(16):15143–15148, Aug 2011.

[189] Conor L. Evans and X. Sunney Xie. Coherent anti-stokes raman scattering microscopy: Chemical imaging for biology and medicine. *Annu. Rev. Anal. Chem.*, 1(1):883–909, jul 2008.

[190] Peijie Wang, Duan Zhang, Lisheng Zhang, and Yan Fang. The {SERS} study of graphene deposited by gold nanoparticles with 785 nm excitation. *Chem. Phys. Lett.*, 556:146 – 150, 2013.

[191] L. G. Cançado, A. Jorio, and M. A Pimenta. Measuring the absolute raman cross section of nanographites as a function of laser energy and crystallite size. *Phys. Rev. B*, 76:064304, Aug 2007.

[192] A T Apostolov, I N Apostolova, and J M Wesselinowa. Temperature and layer number dependence of the g and 2d phonon energy and damping in graphene. *Journal of Physics: Condensed Matter*, 24(23):235401, 2012.

[193] Jingjing Lin, Liwei Guo, Qingsong Huang, Yuping Jia, Kang Li, Xiaofang Lai, and Xiaolong Chen. Anharmonic phonon effects in raman spectra of unsupported vertical graphene sheets. *Phys. Rev. B*, 83:125430, Mar 2011.

[194] Haiqing Zhou, Caiyu Qiu, Fang Yu, Huaichao Yang, Minjiang Chen, Lijun Hu, Yanjun Guo, and Lianfeng Sun. Raman scattering of monolayer graphene: the temperature and oxygen doping effects. *Journal of Physics D: Applied Physics*, 44(18):185404, 2011.

[195] I. Calizo, A. A. Balandin, W. Bao, F. Miao, and C. N. Lau. Temperature dependence of the raman spectra of graphene and graphene multilayers. *Nano Letters*, 7(9):2645–2649, 2007. PMID: 17718584.

[196] G. Montagnac, R. Caracas, E. Bobocioiu, F. Vittoz, and B. Reynard. Anharmonicity of graphite from uv raman spectroscopy to 2700k. *Carbon*, 54:68 – 75, 2013.

[197] Cornelia Nef, Laszlo Posa, Peter Makk, Wangyang Fu, Andras Halbritter, Christian Schonenberger, and Michel Calame. High-yield fabrication of nm-size gaps in monolayer cvd graphene. *Nanoscale*, 6:7249–7254, 2014.

[198] Tsuneya Ando. Anomaly of optical phonon in monolayer graphene. *J. Phys. Soc. Jpn.*, 75(12):124701, 2006.

[199] Gerald D. Mahan. *Many-particle Physics*. Springer US, 2008.

[200] Alexander L. Fetter and John Dirk Walecka. *Quantum Theory of Many-Particle Systems*. Dover publications, 2003.

[201] Hidekatsu Suzuura and Tsuneya Ando. Phonons and electron-phonon scattering in carbon nanotubes. *Phys. Rev. B*, 65:235412, May 2002.

[202] Michele Lazzeri and Francesco Mauri. Nonadiabatic kohn anomaly in a doped graphene monolayer. *Phys. Rev. Lett.*, 97:266407, Dec 2006.

[203] Michele Lazzeri, S. Piscanec, Francesco Mauri, A. C. Ferrari, and J. Robertson. Electron transport and hot phonons in carbon nanotubes. *Phys. Rev. Lett.*, 95:236802, Nov 2005.

[204] Raman spectroscopy of graphene and graphite: Disorder, electronphonon coupling, doping and nonadiabatic effects. *Solid State Communications*, 143(12):47 – 57, 2007. Exploring graphene Recent research advances.

[205] M. A. Marangoni, D. Brida, M Quintavalle, G. Cirmi, F. M. Pigozzo, C. Manzoni, F Baronio, A. D. Capobianco, and G. Cerullo. Narrow-bandwidth picosecond pulses by spectral compression of femtosecond pulses in second-order nonlinear crystals. *Opt. Express*, 15(14):8884–8891, Jul 2007.

[206] A. V. Baranov, A. N. Bekhterev, Ya. S. Bobovich, and V. I. Petrov. Interpretation of certain characteristics in raman spectra of graphite and glassy carbon. *Opt. Spectroscopy*, 62, 1987.

[207] C. Thomsen and S. Reich. Double Resonant Raman Scattering in Graphite. *Phys. Rev. Lett.*, 85(24):5214–5217, December 2000.

[208] PingHeng Tan, Long An, LuQi Liu, ZhiXin Guo, Richard Czerw, David L. Carroll, Pulickel M. Ajayan, Nai Zhang, and HongLi Guo. Probing the phonon dispersion relations of graphite from the double-resonance process of stokes

and anti-stokes raman scatterings in multiwalled carbon nanotubes. *Phys. Rev. B*, 66:245410, Dec 2002.

[209] L. G. Cançado, M. A. Pimenta, R. Saito, A. Jorio, L. O. Ladeira, A. Grueneis, A. G. Souza-Filho, G. Dresselhaus, and M. S. Dresselhaus. Stokes and anti-stokes double resonance raman scattering in two-dimensional graphite. *Phys. Rev. B*, 66:035415, Jul 2002.

[210] T. Gokus, R. R. Nair, A. Bonetti, M. Bhmler, A. Lombardo, K. S. Novoselov, A. K. Geim, A. C. Ferrari, and A. Hartschuh. Making graphene luminescent by oxygen plasma treatment. *ACS Nano*, 3(12):3963–3968, 2009.

[211] Eric Pop, Vikas Varshney, and Ajit K. Roy. Thermal properties of graphene: Fundamentals and applications. *MRS Bull.*, 37(12):1273–1281, 12 2012.

[212] Hugen Yan, Daohua Song, Kin Fai Mak, Ioannis Chatzakis, Janina Maultzsch, and Tony F. Heinz. Time-resolved raman spectroscopy of optical phonons in graphite: Phonon anharmonic coupling and anomalous stiffening. *Phys. Rev. B*, 80:121403, Sep 2009.

[213] Raphael Tsu and Jesus Gonzalez Hernandez. Temperature dependence of silicon raman lines. *Applied Physics Letters*, 41(11):1016–1018, 1982.

[214] Derek A. Long. *The Raman Effect: A Unified Treatment of the Theory of Raman Scattering by Molecules*. John Wiley Sons, Ltd, 2002.

[215] K. T. Schomacker and P. M. Champion. Investigations of spectral broadening mechanisms in biomolecules: Cytochrome-c. *The Journal of Chemical Physics*, 84, 1986.

[216] Mark Kasperczyk, Ado Jorio, Elke Neu, Patrick Maletinsky, and Lukas Novotny. Stokes–anti-stokes correlations in diamond. *Opt. Lett.*, 40(10):2393–2396, May 2015.

[217] Carlos A. Parra-Murillo, Marcelo F. Santos, Carlos H. Monken, and Ado Jorio. Stokes–anti-stokes correlation in the inelastic scattering of light by matter

and generalization of the bose-einstein population function. *Phys. Rev. B*, 93:125141, Mar 2016.

[218] Ado Jorio, Mark Kasperczyk, Nick Clark, Elke Neu, Patrick Maletinsky, Aravind Vijayaraghavan, and Lukas Novotny. Optical-phonon resonances with saddle-point excitons in twisted-bilayer graphene. *Nano Letters*, 14(10):5687–5692, 2014. PMID: 25198466.

[219] Ado Jorio, Mark Kasperczyk, Nick Clark, Elke Neu, Patrick Maletinsky, Aravind Vijayaraghavan, and Lukas Novotny. Stokes and anti-stokes raman spectra of the high-energy cc stretching modes in graphene and diamond. *physica status solidi (b)*, 252(11):2380–2384.

[220] C. Neumann, S Reichardt, P. Venezuela, M. Drögeler, L. Banszerus, M. Schmitz, K. Watanabe, T. Taniguchi, F. Mauri, B. Beschoten, S. V. Rotkin, and C. Stampfer. Raman spectroscopy as probe of nanometre-scale strain variations in graphene. *Nat. Commun.*, 6:8429, 2015.

[221] M. Schütt, P. M. Ostrovsky, I. V. Gornyi, and A. D. Mirlin. Coulomb interaction in graphene: Relaxation rates and transport. *Phys. Rev. B*, 83:155441, Apr 2011.

[222] Dong-Hun Chae, Benjamin Krauss, Klaus von Klitzing, and Jurgen H. Smet. Hot phonons in an electrically biased graphene constriction. *Nano Letters*, 10(2):466–471, 2010. PMID: 20041665.

[223] Stefano de Gironcoli. Lattice dynamics of metals from density-functional perturbation theory. *Phys. Rev. B*, 51:6773–6776, Mar 1995.

[224] Paolo Giannozzi, Stefano Baroni, Nicola Bonini, Matteo Calandra, Roberto Car, Carlo Cavazzoni, Davide Ceresoli, Guido L Chiarotti, Matteo Cococcioni, Ismaila Dabo, Andrea Dal Corso, Stefano de Gironcoli, Stefano Fabris, Guido Fratesi, Ralph Gebauer, Uwe Gerstmann, Christos Gougoussis, Anton Kokalj, Michele Lazzeri, Layla Martin-Samos, Nicola Marzari, Francesco Mauri, Riccardo Mazzarello, Stefano Paolini, Alfredo Pasquarello, Lorenzo

Paulatto, Carlo Sbraccia, Sandro Scandolo, Gabriele Sclauzero, Ari P Seitsonen, Alexander Smogunov, Paolo Umari, and Renata M Wentzcovitch. Quantum espresso: a modular and open-source software project for quantum simulations of materials. *J. Phys. Condens. Matter*, 21(39):395502, 2009.

[225] Yuejian Wang, Joseph E. Panzik, Boris Kiefer, and Kanani K. M. Lee. Crystal structure of graphite under room-temperature compression and decompression. *Sci. Rep.*, 2, July 2012.

[226] C. Ferrante, A. Virga, L. Benfatto, M. Martinati, D. De Fazio, U. Sassi, C. Fasolato, A. K. Ott, P. Postorino, D. Yoon, G. Cerullo, F. Mauri, A. C. Ferrari, and T. Scopigno. Raman spectroscopy of graphene under ultrafast laser excitation. *Nat. Commun.*, 9:308, 2018.

[227] Ji-xin Cheng, Andreas Volkmer, Lewis D. Book, and X. Sunney Xie. An epi-detected coherent anti-stokes raman scattering (e-cars) microscope with high spectral resolution and high sensitivity. *The Journal of Physical Chemistry B*, 105(7):1277–1280, 2001.

[228] Eric O. Potma, Conor L. Evans, and X. Sunney Xie. Heterodyne coherent anti-stokes raman scattering (cars) imaging. *Opt. Lett.*, 31(2):241–243, Jan 2006.

[229] Feruz Ganikhanov, Conor L. Evans, Brian G. Saar, and X. Sunney Xie. High-sensitivity vibrational imaging with frequency modulation coherent anti-stokes raman scattering (fm cars) microscopy. *Opt. Lett.*, 31(12):1872–1874, Jun 2006.

[230] Andreas Volkmer, Lewis D. Book, and X. Sunney Xie. Time-resolved coherent anti-stokes raman scattering microscopy: Imaging based on raman free induction decay. *Applied Physics Letters*, 80(9), 2002.

[231] Ji-Xin Cheng, Lewis D. Book, and X. Sunney Xie. Polarization coherent anti-stokes raman scattering microscopy. *Opt. Lett.*, 26(17):1341–1343, Sep 2001.

List of Figures

List of Tables

Appendix A

Suppression of NVRB

As NVRB derives not only from the sample but also may be from the cuvette or cover-slip, on which it is mounted, it often overwhelms the resonant signal, reducing chemical sensitivity in CARS experiments. Therefore, several methods have been developed to reduce or suppress the nonresonant contribution to the signal [144].

- Epi-detection CARS [227]: Microscopy under tight focusing condition provides wavevectors of pump and Stokes pulses in a cone with a large angle and hence relaxes the phase-matching condition ($\Delta kL \ll \pi$), which is fulfilled in both forward and backward directions. Referring to FWM equation, the phase-matching condition for both resonant and nonresonant contributions is the same, although in epi-detection it can be considered that the resonant signal satisfies the condition $L \sim 0$, while $|\Delta k| = 2k_{as}$: this causes the enhancement of resonant-nonresonant ratio, due to elimination of NRB from bulk materials, but not from smaller scatterers.

- Interferometric CARS [228]: the CARS field $E_{as} \propto E_p^2 E_s^* [\chi_R^{(3)} + \chi_{NR}^{(3)}]$ is mixed with a well-controlled external field at the same frequency, E_{LO}, known as local oscillator. This means that the total intensity at frequency ω_{as} is given by:

$$\begin{aligned} I = |E_{as} + E_{LO}|^2 = |E_{as}|^2 + |E_{LO}|^2 + \\ + 2|E_{LO}|E_p^2 E_s^* [\Re e(\chi_R^{(3)}) + \chi_{NR}^{(3)}] cos\phi + 2|E_{LO}|E_p^2 E_s^* \Im m(\chi_R^{(3)}) sin\phi \end{aligned} \tag{A.0.1}$$

where ϕ is the phase difference between CARS field and local oscillator. It is clear that in the two interferometric terms the real and imaginary parts of $\chi_R^{(3)}$ show different dependences on phase. Setting $\phi = 90^o$ the resonant imaginary contribution is being maximized while the mixing term containing the nonresonant contribution is minimized, thus allowing heterodyne probing of $\Im m(\chi_R^{(3)})$ with suppression of NRB. Furthermore, the detected signal is linear in the concentration of vibrational modes and can be linearly amplified by increasing the amplitude of the local oscillator. Nevertheless, the requirement for three synchronized, phase-locked, independently tunable beams makes this setup complicated and difficult to utilize.

- Frequency modulation CARS [229]: as already described, the resonant contribution is attributed to the molecular vibrations and is enhanced when the pump-Stokes difference frequency matches the characteristic vibrational frequency of the molecule. On the other hand, the non resonant background remains constant under a wide frequency range. If Stokes (pump) source is rapidly switched between two frequencies, this frequency modulation results in an amplitude modulation of the CARS signal $\Delta_I = I(\omega_1) - I(\omega_2)$, that can be extracted by using lock-in detection. Since non-resonant contribution to the CARS signal is spectrally constant, it does not contribute to the detected modulation signal and hence is supressed. A critical point is the choice of ω_1 and ω_2: in fact the value of the nonresonant contribution can vary throughout a heterogeneous sample producing intensity artefacts. By selecting the modulation frequencies to be $\Omega \pm \Gamma/2$, where Γ is the FWHM linewidth of the resonant response, the linear term $2\Re e[\chi_R^{(3)}]\chi_{NR}^{(3)}$ can be efficiently suppressed.

  It is worth noting that frequency modulation needs to be done at high repetition rate in order to separate the modulated signal from lower frequency laser-noise and it requires three synchronized pulses.

- Time-resolved CARS [230]: temporally overlapped pump and Stokes pulses, tuned to the frequency of a Raman active vibrational mode, are able to excite vibrational coherence in the sample, that decays exponentially in time. As the

non-resonant background is related to electronic transitions, it could be considered instantaneous; thus, delaying the two pulses in time allows the detection of only the resonant signal, although significantly reduced in intensity.

- Polarization CARS [231]: until now, we have referred to CARS as a scalar interaction, neglecting vector properties of the field. Nevertheless, a possible way to suppress NVRB is to take advantage of the polarization difference between resonant and non-resonant contribution. Let us suppose that both pump and Stokes pulses propagate along z axis: the pump beam is linearly polarized along x, while the Stokes linear polarization forms an angle ϕ with x-axis. By considering Kleinmann symmetries for the third-order susceptibility tensor, the x and y components of $P^{(N)R}$ can be written as:

$$\begin{aligned} P_x^{(N)R} &= 3\chi_{1111}^{(3)} E_p^2 E_s^* cos\phi \\ P_y^{(N)R} &= 3\chi_{1221}^{(3)} E_p^2 E_s^* sen\phi \end{aligned} \tag{A.0.2}$$

In the absence of any electronic resonances, P^{NR} is linearly polarized with angle θ with respect to x-axis:

$$P^{(N)R} = 3\chi_{1111}^{(3)} E_p^2 E_s^* cos\phi / cos\theta \tag{A.0.3}$$

where the angle θ is related to ϕ by $tan\theta = tan\phi \left(\chi_{1221}^{(3)NR} / \chi_{1111}^{(3)NR}\right) = tan\phi \cdot \rho_{NR}$. ρ_{NR} is the depolarization ratio of the non-resonant term and according to the rule of Kleinmann symmetry assumes a value of 1.3. P^R is linearly polarized in a different direction from that of the non-resonant counterpart, that can be suppressed by using a polarization sensitive detection. If an analyzer is placed before the detector perpendicularly to P^{NR}, the total projection can be written as:

$$P_\perp = 3E_p^2 E_s^* \chi_{1111}^{(3)R} (cos\phi\, sin\theta - \frac{\chi_{1221}^{(3)R}}{\chi_{1111}^{(3)R}} sin\phi\, cos\theta) \tag{A.0.4}$$

Pratically it is impossible to achieve a perfect NRB suppression due to the presence of birifrengent optical elements. Moreover, different vibrational modes may have different depolarization ratios, requiring different settings of the polarizers: this explains a quite limited use of this method in CARS microscopy.